Copyright
by
Yicong Wang
2017

The Dissertation Committee for Yicong Wang
certifies that this is the approved version of the following dissertation:

Impact of Blockage and Mobility on Collaborative Sensing and Millimeter Wave Based Communication

Committee:

Gustavo de Veciana, Supervisor

François Baccelli

Robert Heath Jr.

Lili Qiu

John Hasenbein

Impact of Blockage and Mobility on Collaborative Sensing and Millimeter Wave Based Communication

by

Yicong Wang

DISSERTATION

Presented to the Faculty of the Graduate School of

The University of Texas at Austin

in Partial Fulfillment

of the Requirements

for the Degree of

DOCTOR OF PHILOSOPHY

THE UNIVERSITY OF TEXAS AT AUSTIN

December 2017

Dedicated to my family.

Acknowledgments

First I would like to express my sincerest gratitude to my PhD supervisor Dr. Gustavo de Veciana, for his continuous support and guidance. It is my great fortune to have Dr. de Veciana as my supervisor, who has set an exceptional example of excellence as a instructor, researcher, mentor and friend. The time spent with him will always be an invaluable asset to me.

I want to thank my dissertation committee members: Dr. François Baccelli, Dr. Robert W. Heath Jr., Dr. Lili Qiu, and Dr. John Hasenbein. I really appreciate their time and valuable comments on this dissertation. Moreover the exceptional works of Dr. Baccelli and Dr. Heath are of great help to my research. I also want to thank Dr. Jeff Andrews, Dr. Constantine Caramanis, Dr. Sujay Sanghavi, Dr. Sanjay Shakkottai, Dr. Lorenzo Alvisi, Dr. Adnan Aziz, Dr. Craig Chase, and several other professors, whose courses provide enormous help on both my graduate research and future career.

I would like to thank Intel, National Science Foundation, and Toyota Infotechnology Center, for financially supporting my research. I would like to thank Dr. Kerstin Johnsson at Intel for her suggestions and helpful discussions on the 5G project. I thank Dr. Takayuki Shimizu and Dr. Hongsheng Lu for their help on our vehicular sensing project. I also want to thank Dr. Ping Wang, Dr. Shu-ping Yeh, and Dr. Yangseok Choi, for their help and guidance

during my intern at Intel Labs.

I want to thank friends for their accompany during my wonderful five years at UT: Xinyang Yi, Yingzhe Li, Tong Zhao, Zheng Lu, Yuhuan Du, Jiaxiao Zheng, Zhuoran Zhao, Shuang Song, Chenguang Liu, Hongbo Si, Tianyang Bai, Jianhua Mo, Yitao Chen, Qi Wang, Yuyang Wang, Chao Chen, Qiaoyang Ye, Xingqin Lin and many others. I would like to give special thanks to my roommates, Lingyuan Gao, Xiyuan Tang and Yibo Lin, who are wonderful in every way.

Finally I want to thank my mom and dad for their unconditional love and support throughout my life. I would not have been here without you.

Impact of Blockage and Mobility on Collaborative Sensing and Millimeter Wave Based Communication

Publication No. _____

Yicong Wang, Ph.D.
The University of Texas at Austin, 2017

Supervisor: Gustavo de Veciana

This dissertation considers the impact of blockage and mobility on collaborative sensing and millimeter wave (mmWave) based communication networks. We first study the character of interference and MAC performance in dense indoor mmWave wearable networks. Using simple stochastic geometric models for propagation in mmWave bands, we quantify the number of strong interferers as seen by a typical receiver and show that it is limited due to blockage. We propose a model to evaluate the performance of current MAC designs using clustering and hierarchical scheduling. Our results show that the MAC overheads are scalable, i.e., the performance optimal cluster size does not grow with user density in dense scenarios. Furthermore, we show that at high densities the per user throughput is eventually constant.

Next we consider the impact of blockage mobility on MAC overheads and performance in such networks. We propose a stochastic geometric model

to capture the temporal dynamics of strong interfering channels resulting from blocking in networks comprising both fixed and mobile blockages. Based on our analysis, we derive the rate of change in channels' states, i.e., Line-of-Sight (LOS) and Non-LOS (NLOS), and estimate the signaling overheads resulting from blockage mobility. We argue that while the overheads to track the interference environment may in fact be limited, MAC protocols will most likely be better off not coordinating with distant and/or mobile nodes.

We then move on to another area where obstructions have a major impact, i.e., collaborative sensing for automated driving applications. Both the sensing and communication for collaborative sensing may be subject to obstructions (blockages) in such a collaborative setting. We introduce new models for vehicular collaborative sensing and networking under obstructions and evaluate how "performance" scales. In particular, we quantify the coverage and reliability gains obtained by collaborative sensing as a function of the penetration of collaborative vehicles. We further evaluate the associated communication loads in terms of vehicle-to-vehicle (V2V) and/or vehicle-to-infrastructure (V2I) capacity requirements and how these depend on penetration. Sensing by a single vehicle can be highly limited by obstructing neighboring vehicles and objects, while collaborative sensing is shown to greatly improve sensing performance, e.g., improves coverage from 20% to 80% with a 20% penetration. Furthermore, the volume of sensor data a vehicle generates and needs to share for collaborative sensing does not necessarily increase with the density of objects. In scenarios with limited penetration and enhanced

reliability requirements, infrastructure can be used to sense the environment and relay data. Once penetration is high enough, vehicular collaborative sensing provides good sensing coverage and V2V connectivity. Data traffic can be effectively 'offloaded' to V2V network, making V2I resources available to support other services.

Finally we present a more detailed evaluation of the performance of collaborative sensing assisted by sensing capable infrastructure, including Road Side Units (RSUs) and sensors on cellular infrastructure. We compare the performance of different infrastructure and deployment schemes in terms of collaborative sensing coverage. Unless deployed along roads, cellular based sensors off the roads are more obstructed and RSUs deployed at intersections and at even spacings appear more desirable. Simulation results show that RSUs see fewer environmental obstructions when placed higher than vehicles and can benefit from temporal diversity in sensing. Although RSUs have good sensing coverage, in order to communicate with the relevant vehicle, they will require relatively high communication range, rate and reliability. Even if RSUs provide complete coverage of the roads, to increase reliability of sensing, e.g., redundancy in sensing, collaboration amongst sensing capable vehicles may still be desirable.

Table of Contents

Acknowledgments **v**

Abstract **vii**

List of Tables **xiv**

List of Figures **xv**

Chapter 1. Introduction **1**

1.1 Motivation 1

1.2 Related Work 5

1.2.1 Related Work on mmWave Based Wearable Networks . 5

1.2.2 Related Work on Sensing for Automated Driving 8

1.3 Contributions and Organization 10

Part I Impact of Blockage and Mobility on mmWave Based Wearable Networks **13**

Chapter 2. MAC Scheduling for Dense Wearable Networks **14**

2.1 Model Formulation 14

2.2 MAC Perspective on Interference in Dense Millimeter Wave Wearable Networks 20

2.2.1 Number of Strong Interferers 21

2.2.2 Stability of Strong Interferers 25

2.2.3 Numerical Results on Interference 28

2.3 Hierarchical Wearable MAC 33

2.3.1 Hierarchical MAC for Wearable Networks 34

2.3.2 Modeling the Achievable Reuse for Hierarchical MAC Scheduling 36

2.3.3 Numerical Results and Discussion 42
2.4 Conclusion 49

Chapter 3. Temporal Dynamics of Mobile Blocking in Millimeter Wave Based Wearable Networks 51
3.1 System Model and Background Results 51
3.1.1 Background Notation and Key Results 52
3.1.2 System Model 53
3.2 Time-varying Blocking for a Fixed Channel 60
3.2.1 Probability of Having LOS Link 60
3.2.2 Temporal Variation of Fixed Channels 61
3.3 Rate of Change for Strong LOS Neighbors Seen by a Typical Receiver 66
3.4 Impact on MAC in mmWave Networks 69
3.5 Numerical Results 71
3.6 Conclusion 76
3.7 Appendix 78
3.7.1 Proof of Theorem 3.3.1 78

Part II Impact of Blockage and Mobility on Collaborative Sensing for Automated Driving Applications 81

Chapter 4. Performance and Scaling of Collaborative Sensing and Networking for Automated Driving Applications 82
4.1 Modeling Sensing in Obstructed Environments 82
4.1.1 Obstructed Environments and Sensing Capabilities . . . 82
4.1.2 Vehicle's Region of Interest 86
4.1.3 Collaborative Sensing in an Obstructed Environment . . 86
4.1.4 Sensor Coverage Area: Numerical and Simulation Results 88
4.2 Performance Benefits of Collaborative Sensing 91
4.2.1 Sensing Redundancy 92
4.2.2 Collaborative Sensing Coverage and Reliability. 94
4.2.3 Benefits of Collaboration with Sensing RSUs. 102

4.3 Data Volumes to Support Collaborative Sensing 102
4.3.1 Representations and Compression of Sensor Data. . . . 103
4.3.2 Scaling Behavior of Sensor Data Volumes 105
4.4 Network Capacity Scaling for Collaborative Sensing 107
4.4.1 Capacity Scaling in V2V Network 108
4.4.2 Capacity Scaling in V2V+V2I Network 112
4.4.3 Numerical Results 115
4.5 Conclusion 118
4.6 Appendix: Proofs and Additional Results 119
4.6.1 Proof of Theorem 4.1.4 119
4.6.2 Proof of Theorem 4.2.2 121
4.6.3 Proof of Theorem 4.4.1 122
4.6.4 Proof of Theorem 4.4.2 123
4.6.5 V2I Capacity with V2V Relay by Vehicles in Neighbor Lanes 124

Chapter 5. Infrastructure Assisted Collaborative Sensing 130
5.1 Comparison of RSU and Cellular Based Sensing 130
5.1.1 System Model 130
5.1.2 RSU Based Sensing Coverage 136
5.1.3 Cellular Based Sensing Coverage 138
5.1.4 Comparisons 141
5.2 RSU Assisted Collaborative Sensing 146
5.2.1 Sensing of Objects 147
5.2.2 RSU Assisted Collaborative Sensing Scenario 149
5.2.3 Numerical Results on RSU Sensing 152
5.3 Spatio-temporal Diversity in Collaborative Sensing 158
5.3.1 Temporal Dynamic Environment and Sensing Model . . 159
5.3.2 Sensing Redundancy and Coverage Resulting from Temporal Dynamics 160
5.3.3 Performance of Collaborative Sensing Utilizing Spatio-temporal Diversity 162
5.3.4 Generalized Sensing with Mobile Sensors 166

5.4 Robustness in Collaborative Sensing 169
5.4.1 Metric for Sensing Robustness 169
5.4.2 Impact of Failures 170
5.5 Conclusion 171
5.6 Appendix: Proofs and Additional Results 172
5.6.1 Proof of Theorem 5.1.1 172
5.6.2 Proof of Theorem 5.1.2 173
5.6.3 RSU Sensing Coverage in Poisson Line Process Model . 174

Chapter 6. Conclusion and Future Work **178**

Bibliography **180**

Vita **192**

List of Tables

2.1 Parameters in wearable MAC performance analysis 43

List of Figures

2.1 Wearable network using 802.11ad distributed clustering MAC. 15
2.2 Illustration of the location of PCP and self-blockage model . . 16
2.3 Model for the wearable network as seen by a reference user located at 0. 17
2.4 Blockage model for LOS and NLOS channels 19
2.5 How expected number of strong interferers changes with user density 30
2.6 PDF of LOS strong interferers as a function of distance to reference user 30
2.7 Distribution of interferers at different user densities 31
2.8 Stability at different user densities 33
2.9 Frame structure and reuse in clustering based MAC 35
2.10 Model for clustering and channel selection 39
2.11 Successful transmission time of different types of traffic at different cluster sizes 45
2.12 Prob. of successful transmission at different cluster sizes . . . 46
2.13 Primary transmission successful transmission time at different beamwidths 47
2.14 Cluster sizes optimizing per user successful transmission time at different user densities 48
2.15 Per user successful transmission time at different user densities under different MAC protocols 49

3.1 Model for mobile users 56
3.2 Model of fixed and mobile blockages, and mobile blockage traces 58
3.3 Two-state continuous time Markov model for temporal variation of a fixed link 66
3.4 Illustration of movement of user for analysis of rate of change 68
3.5 Evaluation of distribution of T_{LOS} and T_{NLOS} 72
3.6 Rate of change in states of channels to neighbor users 74

3.7 Impact of mobility on joining cluster 75
3.8 Impact of mobility on re-clustering 77

4.1 Environment model for collaborative sensing 84
4.2 Sensing support model 85
4.3 Sensor coverage set under obstruction 87
4.4 Example of collaborative sensing in analytical model and freeway simulation 90
4.5 Normalized coverage area of a typical sensing vehicle at different vehicle densities 91
4.6 Redundancy of location at different vehicle densities 93
4.7 Decomposition of region of interest for collaborative sensing coverage approximation 95
4.8 Example of collaborative sensing coverage in analytical model and simulation 97
4.9 Coverage reliability for different redundancy requirement at different penetrations 99
4.10 Collaborative sensing coverage reliability at different vehicle densities and penetrations 100
4.11 Coverage reliability at different obstruction densities given fixed collaborative sensing vehicle density 101
4.12 Sensor data volume generated by a vehicle at different vehicle (object) densities 106
4.13 Model for collaborative sensing of vehicles in a single lane with V2V + V2I network 112
4.14 Model for collaborative sensing of vehicles in a single lane with assistance from vehicles in the two neighboring lanes 114
4.15 Scalability of V2I and V2V capacity in the penetration of collaborative sensing vehicles 117
4.16 Difference in V2I capacity when a collaborating vehicle's communication fails 118
4.17 Scalability of V2I capacity for collaborative sensing of vehicles on a single lane assisted by vehicles in neighboring lanes . . . 128

5.1 Model of infrastructure assisted sensing in Manhattan Poisson line process road system 131
5.2 Cellular based sensing obstruction model 135

5.3 Cellular based sensing in dense urban area 136
5.4 Footprint of a typical building 140
5.5 Minimum sensor density for 90% coverage at different road densities 142
5.6 Minimum sensor density for different coverage requirements at road density 6km / km^2 143
5.7 Relation between required RSU density and unobstructed BS density 145
5.8 Model for collaborative sensing with RSU 150
5.9 Coverage for RSU and vehicular sensing (base case) 152
5.10 RSU coverage for different (V2V and V2I) communication ranges 153
5.11 RSU coverage for different RSU heights 154
5.12 RSU coverage for random and even space deployment 155
5.13 RSU coverage at different RSU-to-road distances 156
5.14 RSU coverage at different RSU densities 157
5.15 RSU coverage with different RSU sensing ranges 157
5.16 Freeway simulation scenario for RSU assisted collaborative sensing with temporal dynamics 163
5.17 1-object coverage reliability of collaborative sensing with RSUs using temporal diversity 164
5.18 Infrastructure assisted sensing scenarios in Poisson line process road model 175
5.19 Required RSU densities under MPLP model and Poisson line process model when RSUs are deployed at intersections 177

Chapter 1

Introduction

1.1 Motivation

The rapid evolution of mobile technologies has introduced new devices and applications requiring high data rate, low latency and/or high reliability.

A new class of networks currently being developed is that in support of wearable technologies. In the near future each user might be equipped with multiple on-body interconnected devices [1], some of which may require high rates and/or low latency, e.g., devices supporting high quality audio/video, or enabling real-time augmented reality applications. Millimeter wave (mmWave) wireless technologies are suitable to meet these requirements and are being standardized for use in short-range wireless personal area networks (WPAN), e.g., 802.11ad [2], 802.15.3c [3] and ECMA387 [4].

In order to be viable such technologies will need to operate seamlessly in a wide range of environments, including settings with high densities of users/vehicles and dynamics. Even though in the mmWave band there is high signal attenuation, human body blockage, and typically directional transmissions, we posit that in dense indoor environments interference is still a problem. Indeed there are at least three issues that pose problems. First in order to

achieve narrow beams one would typically use a large array of antennas. Such arrays can be miniaturized and produced at low cost, however the computational and energy costs to process the signals they generate/capture may not be workable for wearable applications. Secondly, even if the above costs are acceptable for high end devices, e.g., cellular phones, augmented reality headsets, etc., they may not be for low end devices wishing to share the same band which may use wider beams. Thirdly, since mmWave channels are sensitive to user movements, it may be necessary to use wider transmit beams in order to retain connectivity in a dynamic environment and/or reduce signaling overheads associated with channel estimation and beam tracking. For these reasons we expect that in dense scenarios MAC scheduling will play a critical role in mitigating interference.

However MAC protocol design in such settings also faces several challenges. In particular in order to effectively schedule transmissions a MAC scheduler needs to be aware of the neighboring strong interferers – which may be large in numbers and vary quickly. Indeed for dense settings, e.g., a crowded train car, the set of strong interferers could be large, leading to high signaling overheads and reduced channel reuse. Moreover due to the sensitivity of mmWave channels to motion and blockage this set may change quickly and be subject to uncertainty resulting in additional signaling costs and degraded performance. In this dissertation we will develop an understanding of the characteristics of the interference environment in dense wearable settings, in particular the impact of human body blockage and its mobility. We use these

results to evaluate their impact on MAC design for such networks.

Another application which is sensitive to blockages and obstructions is collaborative sensing in support of automated driving. In future automated driving systems, vehicles will sense their surrounding environment in real time. Despite vehicles being equipped with multiple sensors, e.g., radar, LIDAR and cameras, the sensing capacity of the sensors mounted on a single vehicle is limited. Sensors can typically only detect objects in their line-of-sight (LOS) thus are subject to obstructions. We envisage that neighboring vehicles perform collaborative sensing to extend the view of a single vehicle and improve the reliability of sensed information. However, exchanging sensor data, especially raw sensor data, among vehicles can be costly. The network can be crowded and dynamic, and the requirements on communication can be stringent, e.g., high data rates and low latency.

To better design future collaborative sensing applications and communication networks, it is crucial to develop an understanding of the performance benefits and costs of collaborative sensing. For the performance benefits, we want to quantify the performance gains of collaborative sensing in terms of sensing coverage and reliability and how they depend on the environment, e.g., density of vehicles and objects, and penetration of sensing and communication capable collaborative vehicles. For the communication amongst vehicles, high rate V2V links, e.g., mmWave V2V links, seem to meet the communication requirements. However, as is the case for sensing, mmWave V2V links also depend on LOS channels and are subject to blockages of neighboring objects.

At a low penetration of collaborative sensing and communication vehicles, mmWave based V2V (relay) paths may be blocked, and V2I communication would be required to facilitate the exchange of sensor data. The traffic loads on V2V and V2I networks depends on the penetration of communication capable collaborative vehicles, and in this dissertation we study how the required traffic loads vary with the penetration of collaborative sensing vehicles.

Infrastructure can help relay sensor data amongst collaborating vehicles to overcome potential blockage in communication, yet the limited sensing coverage at low penetrations can still be a problem. One possible solution is to deploy sensing capable infrastructure to assist vehicles with collaborative sensing. The performance of infrastructure assisted sensing would depend on the deployment schemes and infrastructure's sensing / communication capabilities. Two possible options for deploying sensors include 1) placing sensing capabilities on cellular infrastructure (randomly) located in space, and 2) deploying sensing and communication capable RSUs along roads. Deploying sensors on existing cellular infrastructure, e.g., base stations (BSs), may cost less as we can reuse the back-end and communication infrastructure. However, BSs may see more obstructions than RSUs, e.g., buildings along the road, if BSs are not also placed along the road. Other factors impacting performance include, e.g., the height of sensors, the RSU distance to road, RSU and BS sensing / communication range, etc. In addition, sensors on fixed infrastructure would see dynamic objects and obstructions. Such environmental dynamics may also impact the performance benefits of infrastructure assisted sensing. In this dis-

sertation, we will evaluate the impact of these factors and propose principles for the deployment of sensors.

In summary,this dissertation explores network and sensing systems with blockage (obstruction) and mobility, and how the design of the underlying communication networks will be impacted.

1.2 Related Work

There has been substantial works on mmWave communication networks and sensing for automated driving. We first introduce works on mmWave based wearable networks, then discuss the existing works on sensing in vehicular networks.

1.2.1 Related Work on mmWave Based Wearable Networks

There has been a number of initial works on measuring and modeling propagation in the mmWave band. Large scale path loss models were studied for outdoor [5–7] and indoor [6–10] environments. The spatial and temporal statistics of paths have been measured and studied in [8, 10] and 3-D channel models are proposed in [11, 12]. In addition preliminary works in [13–16] study the impact of human body blockage on a channel between two fixed points through measurement and simulation.

In addition to these measurement campaigns and models development, stochastic geometric models and analysis have been widely used to study the capacity of mmWave networks for outdoor [17, 18] and indoor [19, 20] networks

with blocking. In these works, users and blockages are randomly located, the distribution of the signal to interference plus noise ratio (SINR) and the coverage probability of a typical user were computed. However, for tractability, these works assume a simple MAC such as random access Aloha. The authors of [21, 22] studied the capacity of a wearable network featuring more delicate frame structures akin to those used in 802.11ad, but in their work blockage is not considered.

Various standards have been developed to support WPAN in the mmWave band [2–4]. Among these standards, 802.11ad provides the highest data rate and works best in dense settings. In the 802.11ad MAC, users may form clusters. Users within the same cluster are coordinated to avoid intra-cluster interference and improve reuse. However, the throughput of 802.11ad MAC can be limited since two users in the same cluster can not transmit at the same time if they hear each other's beacon. Note that beacons are typically transmitted omni-directionally. MAC protocols have been proposed to improve the capacity of mmWave networks [23–25]. The limitation of current standards and proposed MAC designs is that the characteristics of wearable networks, i.e., the blockage by users body and large densities of devices, are not fully addressed. The work of [26] proposes a link scheduling protocol considering mobile blockage, but the blockage model does not consider the actual characteristics of dense wearable networks, i.e., the parameters of channels are set without considering the blockage model, user density and locations of users.

Channels in the mmWave bands are highly sensitive to user movements,

including small local movements like the rotation of a torso or swinging and large scale movements, e.g., people walking around. Acquiring and maintaining robust communication channels in mmWave bands is a recognized physical layer challenge. Many approaches to quickly acquiring and adapting beams are under study see e.g., [27, 28]. On the MAC design end, the authors of [26] propose and evaluate link scheduling algorithms for mmWave ad hoc networks but the characteristics of their channel blockage model are arbitrarily set without accounting for actual blockage mobility models. These works proposed methods to improve the performance of mmWave based networks in the presence of blockage, but lack an understanding of channel characteristics of user mobility. Existing work on user mobility [14–16] study the influence of human activity on the radio channel between a fixed transmitter and receiver. For example, the authors of [14, 16] present measurements of the impact of human mobility on channel variation. The work in [16] further evaluates the probability that a channel is blocked by users and proposes a two-state Markov model for the state of the channel based on experiments. The authors of [15] use simulation to study radio propagation characteristics in the presence of static and moving obstacles and show that directional LOS mmWave links experience relatively high outage. These works provide valuable measurements and insights on the influence of blockages resulting from human mobility, but do not provide models towards understanding the impact of user mobility in dense environments, or towards understanding the impact of density on the conclusions.

1.2.2 Related Work on Sensing for Automated Driving

Collaborative sensing is likely to be one of the key enabling technologies for automated driving systems. Vehicles can exchange real time sensor information with vehicles/RSUs to enhance their view of an obstructed environment [29] [30] [31] [32] [33]. An analysis of the scaling and performance of such systems is however not been done before.

Currently available protocols like Dedicated Short-Range Communication (DSRC) [34] have limited data rates, e.g., IEEE 802.11p suports 3–27 Mbps (typically 6Mbps), and face challenges for high channel loads [35]. LTE systems are evolving to support safety-related V2X applications [36], yet still provide limited capacity and face challenges associated with high density of UEs. To serve the requirements of collaborative sensing, 3GPP defined various use cases and requirements in [37] [38]. Also mmWave technology is being considered to support the sharing of HD sensor data [39] [40].

The representation of the environment and dynamic objects impact the performance of information sharing and the volume of sensor data. Sparse object-based environmental models are currently used but are not sufficient for safety applications in arbitrary environments. Different ways of representing the environment at different levels of abstraction have been proposed, ranging from most compact feature map [41], 2D grid map [42], 3D voxel grid [43], to raw sensor data. Vehicles may share data at different abstraction levels based on the scenario. However, the amount of information generated by each vehicle is in fact also related to the environment, e.g., density of objects/vehicles, due

to blockage, and this problem has not been well investigated.

The capacity of vehicular ad hoc network (VANET) has been studied in a variety of works, see e.g., [44] [45] [46] [47]. The communication requirements for collaborative sensing, i.e., each vehicle requiring local many-to-many information sharing, is different from general VANETs where the source and destination of data need not be close by. Existing capacity analysis needs to be adapted to this many-to-many setting. The authors of [48] study the communication cost of a single vehicle, but obstructions and networking are not considered.

Our work on modeling and assessing the performance of collaborative sensing can be viewed as a stochastic version of what are referred to as the gallery problems [49], which typically address questions such as the number and placement of cameras/guards in a fixed environment to meet a pre-specified coverage criterion.

Infrastructure has been considered to be an important component in ITS to support automated driving [37] [50]. Authors of [51] propose a method to perceive the environment using RSU camera and vehicle GPS. An analysis of the performance of infrastructure assisted sensing, e.g., sensing coverage, is however absent.

1.3 Contributions and Organization

In summary this dissertation addresses the impact of blockage and mobility in two settings: 1) the channel characteristics and thus MAC design in millimeter wave based communications; and 2) the performance and communication costs of collaborative sensing for automated driving applications. The dissertation is organized accordingly.

In Part I we look at the mmWave based wearable networks. In Chapter 2 we study the impact of blockages on MAC design for dense wearable networks. In Section 2.1 we present our system model for dense wearable networks. In Section 2.2 we characterize the number and distribution of the set of "strong interferers" a typical receiver would see, as well as its stability to users' local motion. In Section 2.3 we characterize the capacity of wearable networks utilizing a MAC scheduler which leverages clustering and hierarchical scheduling – not unlike current MAC design approaches. We propose a simple model to analyze the performance and validate it through simulation. Such model permits us to evaluate the impact of MAC design parameters, e.g., cluster size and transmission beamwidths, on the MAC performance.

In Chapter 3 we study the characteristics of temporal dynamics of mmWave channels. We discuss the system model for analysis and necessary background results in Section 3.1. In Section 3.2 we characterize the temporal variation of a fixed channel. We prove that the temporal variation follows an on/off renewal process, and characterize the distribution of on (LOS) and off (OFF) states. We then study the aggregate rate of change of the set of strong

LOS neighbors seen by a typical receiver in Section 3.3. In Section 3.4 we study the MAC overheads associated with simple clustering based MAC protocols as used in current standard in the presence of mobile blockages. In particular, we evaluate the signaling overheads in cluster formation and maintenance in mobile environments. Our numerical results in Section 3.5 illustrate that our analytical model for temporal variations and the rate of change of the set of strong interferers are accurate.

In Part II we study collaborative sensing for automated driving applications. In Chapter 4 we study the performance and scaling of collaborative sensing and networking in support of automated driving. In Section 4.1 we introduce a new stochastic geometric model for collaborative sensing in obstructed environments, which captures both the objects in the environment and sensing capability of sensors, and propose associated performance metrics capturing sensing coverage and reliability. We then quantify the performance of collaborative sensing for varying reliability requirements, vehicle/object densities, and penetrations of collaborative sensing vehicles in Section 4.2. Next we study the communication costs in Section 4.3 and 4.4. In Section 4.3, we study how the volume of sensor data generated by a vehicle under different representation method scales in the vehicle/object density. In Section 4.4 we explore heterogeneous architectures of sensing and communication combining vehicles and infrastructure. Our study of the performance and capacity requirements exhibits the critical role of possible infrastructure assistance in improving sensing coverage and communication reliability especially at the early

stages of collaborative sensing where there may only be a low penetration of collaborative vehicles.

In Chapter 5 we evaluate the performance of infrastructure assisted sensing. In Section 5.1 we compare the sensing coverage of cellular and RSU assisted sensing at different road densities. In Section 5.2 we study the performance of RSU assisted sensing under different deployment schemes, e.g., sensor height, distance to road, sensing and communication ranges, etc. In Section 5.3 we study how sensors can utilize sensing temporal diversity caused by environmental dynamics to improve sensing coverage. We give a brief discussion of robustness in collaborative sensing based automated driving in Section 5.4 and conclude the chapter in Section 5.5.

Chapter 6 provides a summary of the key questions and findings addressed in this dissertation.

Part I

Impact of Blockage and Mobility on mmWave Based Wearable Networks

Chapter 2

MAC Scheduling for Dense Wearable Networks[1]

2.1 Model Formulation

In this section we focus on indoor wearable networks. The devices on each user are assumed to form a Personal Basic Service Set (PBSS), coordinated by the PBSS Control Point (PCP), e.g., the user's smart phone, see Fig. 2.1. Data transmissions only happen between the PCP and non-PCP devices of the same PBSS. There is no access point (AP) or central controller to coordinate or synchronize transmissions across different users. The PBSSs may form clusters, with the PCP of one PBSS working as the synchronization PCP (S-PCP), i.e., the cluster head, to synchronize the beacon transmissions of PBSSs. In the sequel, we will use the channel between two PCPs to approximate the channels amongst the devices in two PBSSs. PCPs are located at the front of each user's body at a fixed height h_{device}, see Fig. 2.2. We define an interferer as a *strong interferer* if the received interference power, P_r, exceeds

[1]This chapter is based on paper: Yicong Wang and Gustavo de Veciana, "Dense indoor mmWave wearable networks: Managing interference and scalable MAC," in *14th International Symposium on Modeling and Optimization in Mobile, Ad Hoc, and Wireless Networks (WiOpt)*, Temple, AZ, 2016. Prof. de Veciana supervised the project.

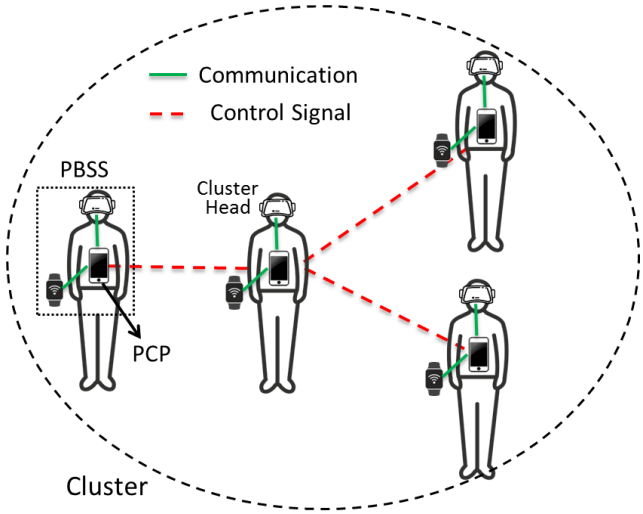

Figure 2.1: Wearable network using 802.11ad distributed clustering MAC.

a threshold γ_{SI}, i.e.,

$$P_r = P_t \cdot G_t \cdot G_r \cdot L \geq \gamma_{\text{SI}},$$

where P_t is the transmit power, G_t and G_r are the transmit and receive antenna gains, and L is the path loss.

User model. Users are assumed to be located on a 2-D plane. Walls and obstructions other than human bodies are not considered, but we shall assume there is a ceiling at a height h_{ceiling}. For simplicity, users' bodies are of the same dimensions.

Consider a reference user located at the origin 0 with a random orientation denoted by a random variable Θ_0, which is uniformly distributed on $[0, 2\pi)$. The centers of other users, denoted by $\Phi = \{X_i\}$, are assumed to follow a homogeneous Poisson Point Process (HPPP) with intensity λ on

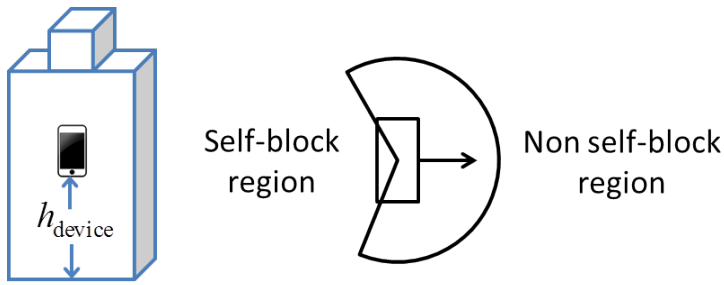

Figure 2.2: Illustration of the location of PCP and self-blockage model. The PCP is located in front of user body at a height h_{device}. In the figure on the right, the arrow indicates the orientation (facing direction) of the user, and the sector centered at the center of the user shows the region with no self-blockage.

$\mathbb{R}^2 \setminus b(0, r_{\min})$. Here $b(0, r_{\min})$ denotes a disc centered at 0 with radius $r_{\min}$, and $r_{\min}$ is the minimum distance between other users and the reference user. Let Θ_i denote the orientation of user i, which is assumed to be independent and identically distributed (IID) and uniformly distributed on $[0, 2\pi)$. $\tilde{\Phi} = \{(X_i, \Theta_i)\}$ is an independently marked point process (IMPP) and the network is uniquely defined by $\tilde{\Phi}$. We let $\tilde{\phi} = \{(x_i, \theta_i)\}$ denote a realization of $\tilde{\Phi}$, where x_i and θ_i denote the location and the orientation of user i respectively. Fig.2.3 illustrates the model of the network.

Channel model. Again for simplicity let the location of the center of a user approximate the location of the user's PCP, see Fig. 2.3. Only two types of channel are considered, the LOS channel and the reflected channel off the ceiling, which we refer to as the NLOS channel. We shall assume a LOS channel follows the free space propagation model while the path loss of the reflected channel is determined by the free space path loss and a ceiling reflection coefficient, Γ, which depends on incident angle and reflection material,

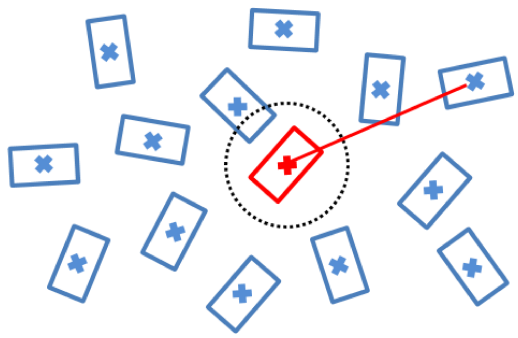

Figure 2.3: Model for the wearable network as seen by a reference user located at 0.

see e.g., [52].

Blockage model. Human body introduces more than 20 dB path loss [13], thus from the MAC perspective, we assume that the interference from a channel is weak to be neglected in MAC scheduling. We assume the channel gain is 0 if a channel is blocked by users, including self blockage. For self blockage, we assume user's body would block both the LOS and NLOS channels to/from devices behind the user as shown in Fig. 2.2. We say that two users are "facing" each other if they are in the non self-blocking regions of each other. The angle of the non self-block region is α.

Blocking by other users can be different for LOS and NLOS channels. Consider the channel between the reference user at 0 and the user at location x, and a potential blocking user (x', θ'), see Fig. 2.4(a). Denote by $l_{0,x}$ the line segment between 0 and x, n_x the unit vector perpendicular to $l_{0,x}$. We assume user at x' blocks the LOS channel, $l_{0,x}$, if the following two conditions are met,

$$s_x(x') \in [0, |x|], \tag{2.1}$$

$$0 \in D_x(x, \theta'), \tag{2.2}$$

where $s_x(x') \in \mathbb{R}$ is the projection of x' on the unit vector from 0 to x, $|x|$ is the distance between x and 0, $D_x(x', \theta') \subset \mathbb{R}$ is the projection of user's cross section at height h_{device} on n_x. For blocking of the NLOS channel, we further assume that the cross section of the user body at height higher than the device, $h \geq h_{\text{device}}$, is contained in the cross section at height h_{device}. Denote by $C_x(x', \theta') \subset \mathbb{R}^2$ the intersection of the cross section of user (x', θ') at height h_{device} and $l_{0,x}$, $h_{\text{NLOS}}(x, s_x(x'))$ is the height of the NLOS channel between 0 and x at a distance $s_x(x')$ from 0 and $h_{(x',\theta')}(y)$ is the height of user (x', θ') at location y, see Fig. 2.4. Based on the assumptions, the user at x' blocks the NLOS channel if the condition in Eq. 2.1 is met and

$$h_{\text{NLOS}}(x, s_x(x')) \leq h_{(x',\theta')}(y), \forall y \in C_x(x', \theta'). \tag{2.3}$$

Notice that if the LOS channel is not blocked, $C_x(x', \theta') = \emptyset$, thus the NLOS channel is also not blocked.

Given P_t, G_t and G_r, let $r_{\max}$ be the maximum distance of a strong interferer when the LOS channel is available, and $r_{\max}^{\text{reflection}}$ that when only the NLOS channel is not blocked. Due to reflection losses and longer path taken, $r_{\max}^{\text{reflection}} < r_{\max}$. For $|x| \in [r_{\min}, r_{\max}^{\text{reflection}}]$, a user at x is a strong interferer if the NLOS channel is not blocked; for $|x| \in (r_{\max}^{\text{reflection}}, r_{\max}]$, a user at x is a strong interferer if the LOS channel is not blocked. Notice that the path loss of the NLOS channel may not be a monotonically increasing function of $|x|$ due to the sensitivity of the reflection coefficient to the incident angle,

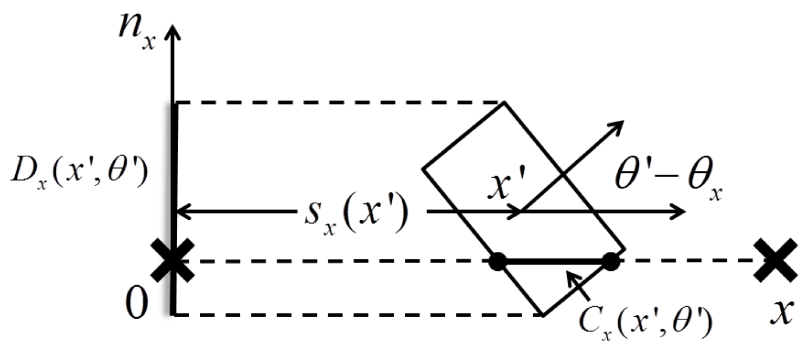

(a) Blockage model for LOS channel

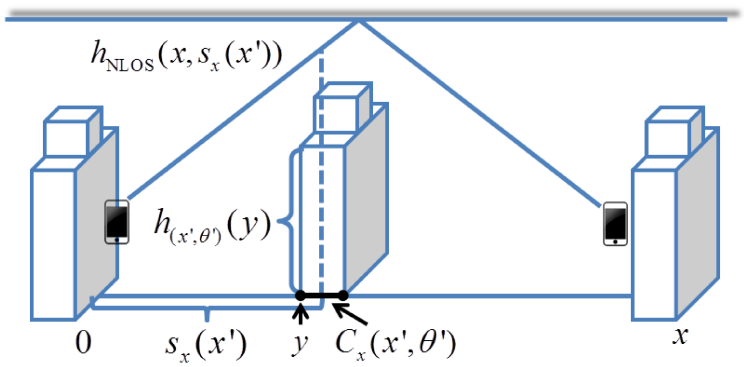

(b) Blockage model for NLOS channel

Figure 2.4: (a) the conditions that user (x', θ') blocks the LOS channel between 0 and x. (b) illustrates the condition that the NLOS channel is blocked.

thus for $|x| \leq r_{\max}^{\text{reflection}}$, having an unblocked NLOS channel may be only a necessary condition, not a sufficient condition, for being a strong interferer in some scenarios. Our model can be easily extended to account for these effects.

Antenna model. We assume that the antenna gain is invariant to the angle between antenna direction and the vertical axis, e.g., the same for the LOS and the NLOS channel between two devices. The antenna gain follows a

sectorized antenna model [17], i.e.,

$$G = \begin{cases} g_{\text{main}}, & \text{w.p. } \beta/2\pi \\ g_{\text{side}}, & \text{w.p. } 1-\beta/2\pi \end{cases},$$

where g_{main} is the antenna gain of main lobe, g_{side} is the antenna gain out of the main lobe, β is the 2-D beamwidth.

There are many complex factors involved in mmWave propagation but the above simple model captures the key features for such systems, e.g., directionality, reflection, and blockages. Notice that in the analysis of strong interferers, the directional transmission is not actually not considered. The reason is that in the current 802.11ad standard, two PBSSs are assumed to be interfering with each other and cannot transmit at the same time if the devices can hear the beacons from the other PBSS. The beacons are transmitted and received in omni-directional mode [2]. The directional antenna model is used in our analysis of wearable MAC performance. Different parameters, e.g., threshold for strong interferers, Γ, NLOS path loss model, and antenna model do impact the accuracy and numerical results of our analysis. Our qualitative analysis is used to capture the key factors and their potential impact on MAC design.

2.2 MAC Perspective on Interference in Dense Millimeter Wave Wearable Networks

In this section, we characterize the interference environment in dense mmWave wearable networks from the MAC perspective, i.e., the characteris-

tics of the set of strong interferers, including the size of the set and its stability under user motion. These characteristics determine the performance and coordination costs associated with MAC scheduling.

For simplicity we assume $G_t = G_r = 1$ and focus our analysis on the impact of channel blockages in this section. Assuming $G_t = G_r = 1$ corresponds to the setting considered in the 802.11ad MAC standard, where two users are considered to be interfering with each other if they can hear each other's beacon which are sent/received omni-directionally. This model can be extended to the case where users have different or heterogeneous beamforming capabilities. These considerations will be included when we evaluate MAC performance in Section 2.3.

2.2.1 Number of Strong Interferers

We first analyze the number of strong interferers seen by the user at 0, $(0, \Theta_0)$, denoted by N_{SI}. N_{SI} can be written as follows,

$$N_{\text{SI}} = \sum_{(X,\Theta)\in\tilde{\Phi}} f\big(X, \Theta, \tilde{\Phi}\backslash\{(X,\Theta)\}, 0, \Theta_0\big), \tag{2.4}$$

where $f(X, \Theta, \tilde{\Phi}\backslash\{(X,\Theta)\}, X_0, \Theta_0)$ is the indicator function that user (X, Θ) is a strong interferer to user (X_0, Θ_0) given the locations and orientations of other users, $\tilde{\Phi}\backslash\{(X,\Theta)\}$.

Due to the blockage effect, N_{SI} is a function of the process $\tilde{\Phi}$, which makes the distribution of N_{SI} hard to compute. Still the average number of strong interferers is a good metric to capture the MAC coordination require-

ments/overhead. Given our proposed modeling assumptions, $\mathrm{E}[N_{\mathrm{SI}}]$ can be computed and as given in the following result.

Theorem 2.2.1. *If users follow an HPPP with intensity λ and users' orientations are uniformly distributed on $[0, 2\pi)$, then for the proposed blockage model we have that,*

$$\begin{aligned}\mathrm{E}[N_{\mathrm{SI}}] = 2\pi\lambda p_{\mathrm{facing}}\Bigg(&\int_{r_{\min}}^{r_{\max}^{\mathrm{reflection}}} e^{-\mathrm{E}\left[N_{\mathrm{B}}^{\mathrm{NLOS}}(x)\middle||x|=r\right]} r dr \\ &+ \int_{r_{\max}^{\mathrm{reflection}}}^{r_{\max}} e^{-\mathrm{E}\left[N_{\mathrm{B}}^{\mathrm{LOS}}(x)\middle||x|=r\right]} r dr\Bigg),\end{aligned} \tag{2.5}$$

where $p_{\mathrm{facing}} = (\frac{\alpha}{2\pi})^2$ is the probability that two users face each other, $N_{\mathrm{B}}^{\mathrm{LOS}}(x)$ is the number of blockages of the LOS channel between 0 and x, excluding the user at 0 and the user at x, while $N_{\mathrm{B}}^{\mathrm{NLOS}}(x)$ is the number of users blocking the NLOS channel between 0 and x.

Before establishing this result, we first characterize the distribution of $N_{\mathrm{B}}^{\mathrm{LOS}}(x)$.

Theorem 2.2.2. *If user locations follow an HPPP with density λ, $N_{\mathrm{B}}^{\mathrm{LOS}}(x)$ has a Poisson distribution with mean $\mathrm{E}[N_{\mathrm{B}}^{\mathrm{LOS}}(x)] \approx \lambda|x|\mathrm{E}[D]$, where $\mathrm{E}[D]$ is the expected width of a user's cross section at height h_{device}. The probability that the LOS channel is not blocked is thus given by $e^{-\mathrm{E}[N_{\mathrm{B}}^{\mathrm{LOS}}(x)]}$.*

Proof. The number of blockages is given by,

$$N_{\mathrm{B}}^{\mathrm{LOS}}(x) = \sum_{(x_i,\theta_i)\in\tilde{\Phi}\setminus(x,\theta)} \mathbb{1}\left((x_i, \theta_i) \text{ blocks } l_{0,x}^{\mathrm{LOS}}\right). \tag{2.6}$$

$\tilde{\Phi}\backslash\{(x,\theta)\}$ is an IMPPP and $\mathbb{1}\left((x_i,\theta_i) \text{ blocks } l_{0,x}^{\text{LOS}}\right)$ is independent of other users, thus $N_{\text{B}}^{\text{LOS}}(x)$ is an independently thinned Poisson process, which is still a Poisson process [53]. The mean of $N_{\text{B}}^{\text{LOS}}(x)$ is given as follows,

$$\begin{aligned}
\mathrm{E}[N_{\text{B}}^{\text{LOS}}(x)] = & \int\limits_{\mathbb{R}^2\setminus b(0,r_{\min})} \int\limits_{[0,2\pi)} \mathbb{1}\left((x',\theta') \text{ blocks } (x,\theta)\right) \\
& \cdot F_{\Theta'}(\mathrm{d}\theta')\lambda(\mathrm{d}x') && (2.7)\\
\overset{(a)}{\approx} & \int\limits_{\mathbb{R}^2\setminus b(0,r_{\min})} \int\limits_{[0,2\pi)} \mathbb{1}\left(0 \in D_x(x',\theta')\right) \\
& \cdot \mathbb{1}\left(s_x(x') \in [0,|x|]\right) F_{\Theta'}(\mathrm{d}\theta')\lambda(\mathrm{d}x') && (2.8)\\
\overset{(b)}{\approx} & \lambda|x| \int\limits_{[0,2\pi)} |D_x(\cdot,\theta')| F_{\Theta'}(\mathrm{d}\theta') && (2.9)\\
\overset{(c)}{=} & \lambda|x|\mathrm{E}[D]. && (2.10)
\end{aligned}$$

In (a), we use the two conditions in Eq. 2.1 and Eq. 2.2 for the blockage of LOS channel to approximate $\mathbb{1}\left((x',\theta') \text{ blocks } (x,\theta)\right)$. In (b), we use the fact that users follow an HPPP with density λ. Since the dimensions and orientation of a user are independent of its location, the distribution of $|D_x(x',\theta')|$ is independent of x'. We neglect $b(0,r_{\min})$ for simplicity, an approximation which is suitable for large $|x|$. In (c), $\mathrm{E}[|D_x|]$ is the expectation of D_x over Θ', which is uniform over $[0,2\pi)$, thus $\mathrm{E}[|D_x|]$ is the same for all x, which we denote by $\mathrm{E}[D]$. □

For NLOS channels, $N_{\text{B}}^{\text{NLOS}}$ also follows a Poisson distribution. One can compute $\mathrm{E}[N_{\text{B}}^{\text{NLOS}}]$ in a similar way as above for $\mathrm{E}[N_{\text{B}}^{\text{LOS}}(x)]$ by substituting

the first indicator function in (2.8), $1\big(0 \notin D_x(x', \theta')\big)$, with the condition in Eq. 2.3.

Now with the distribution of $N_{\mathrm{B}}^{\mathrm{LOS}}$ and $N_{\mathrm{B}}^{\mathrm{NLOS}}$, we can prove Thm. 2.2.1 as follows.

Proof of Theorem 2.2.1. $\mathrm{E}[N_{\mathrm{SI}}]$ can be computed using the reduced Campbell's formula for IMPP of Corollary 2.2 in [53] as follows,

$$\begin{aligned}\mathrm{E}[N_{\mathrm{SI}}] &= \mathrm{E}\Bigg[\sum_{(X,\Theta)\in\tilde{\Phi}} f(X,\Theta,\tilde{\Phi}\backslash\{(X,\Theta)\},0,\Theta_0)\Bigg] \\ &= \int\limits_{[0,2\pi)}\int\limits_{\mathbb{R}^2\backslash b(0,r_{\min})}\int\limits_{[0,2\pi)}\int\limits_{\tilde{\mathbb{M}}} \lambda f(x,\theta,\tilde{\phi}\backslash\{(x,\theta)\},0,\theta_0) \\ &\qquad P^{!}_{\tilde{\Phi}}(\tilde{\phi})F_{\Theta}(d\theta)dxF_{\Theta_0}(d\theta_0),\end{aligned} \tag{2.11}$$

where $\tilde{\mathbb{M}}$ is the space of realizations of $\tilde{\Phi}$, $P^{!}_{\tilde{\Phi}}(\cdot)$ is the reduced Palm distribution of $\tilde{\Phi}$.

According to our blockage model, $\mathrm{E}[N_{\mathrm{SI}}]$ can be computed as follows,

$$\begin{aligned}\mathrm{E}[N_{\mathrm{SI}}] &= \int\limits_{\mathbb{R}^2\backslash b(0,r_{\min})} \mathrm{E}_{\Theta,\Theta_0}\big[\,\mathbb{1}\left((x,\Theta)\text{ faces }(0,\Theta_0)\right)\big] \\ &\quad\cdot\Bigg[\mathbb{1}\left(|x|\in[r_{\min},r_{\max}^{\text{reflection}}]\right)\cdot\Pr\left(N_{\mathrm{B}}^{\mathrm{NLOS}}(x)=0\right) \\ &\quad+\mathbb{1}\left(|x|\in(r_{\max}^{\text{reflection}},r_{\max}]\right)\cdot\Pr\left(N_{\mathrm{B}}^{\mathrm{LOS}}(x)=0\right)\Bigg]\lambda dx \\ &= 2\pi\lambda p_{\text{facing}}\Bigg(\int_{r_{\min}}^{r_{\max}^{\text{reflection}}} e^{-\mathrm{E}\left[N_{\mathrm{B}}^{\mathrm{NLOS}}(x)\big||x|=r\right]}rdr \\ &\quad+\int_{r_{\max}^{\text{reflection}}}^{r_{\max}} e^{-\mathrm{E}\left[N_{\mathrm{B}}^{\mathrm{LOS}}(x)\big||x|=r\right]}rdr\Bigg).\end{aligned} \tag{2.12}$$

Here we let $\mathrm{P}_{\text{facing}}(x) = \mathrm{E}_{\Theta,\Theta_0}\left[\mathbb{1}\left((x,\Theta) \text{ faces } (0,\Theta_0)\right)\right]$, i.e.,

$$\mathrm{P}_{\text{facing}}(x) = \int\limits_{[0,2\pi)}\int\limits_{[0,2\pi)} \mathbb{1}\left((x,\theta) \text{ faces } (0,\theta_0)\right) \cdot F_{\Theta}(\mathrm{d}\theta) F_{\Theta_0}(\mathrm{d}\theta_0). \tag{2.13}$$

Θ_0 and Θ are uniform over $[0, 2\pi)$, thus $\mathrm{P}_{\text{facing}}(x) = p_{\text{facing}} = \left(\frac{\alpha}{2\pi}\right)^2$ for all x. By Thm. 2.2.1, $N_{\mathrm{B}}^{\mathrm{LOS}}(x)$ follows a Poisson distribution with mean $\lambda\,\mathrm{E}[D]|x|$, thus $\Pr\left(N_{\mathrm{B}}^{\mathrm{LOS}}(x) = 0\right) = e^{-\mathrm{E}[N_{\mathrm{B}}^{\mathrm{LOS}}(x)]}$, which is a function of $|x|$. Similarly, $\Pr\left(N_{\mathrm{B}}^{\mathrm{NLOS}}(x) = 0\right) = e^{-\mathrm{E}[N_{\mathrm{B}}^{\mathrm{NLOS}}(x)]}$ is also a function of $|x|$. Combine the above facts, we get Eq. 2.12 and this finishes the proof. □

2.2.2 Stability of Strong Interferers

In this part we study the stability of LOS strong interferers in the presence of users' small scale movements. The stability of strong interferers influences the cost and benefit of tracking and coordinating scheduling with such neighbors: if the set of strong interferers changes quickly, the tracking of neighbors is unreliable thus requires more frequent signaling and associated overheads. For simplicity, we focus on the stability of only LOS strong interferers, but the results are similar for NLOS ones.

We use the following small scale mobility model for our analysis. Suppose that in a time interval $[t, t + \Delta t]$, users make independent small scale movements, i.e., translation ΔX_i and rotation $\Delta\Theta_i$. Denote by $\tilde{\Phi}^t$ the network at time t. Given $\tilde{\Phi}^t = \tilde{\phi}^t$ and the user at 0 is $(0, \theta_0)$ at t, the changes of

the network can be summarized as follows:

$$(0, \theta_0) \to (\Delta X_0, \theta_0 + \Delta\Theta_0),$$

$$\tilde{\phi}^t = \{(x_i, \theta_i)\} \to \tilde{\Phi}^{t+\Delta t} = \{(x_i + \Delta X_i, \theta_i + \Delta\Theta_i)\}.$$

We assume the following simplified local mobility model. ΔX_i and $\Delta\Theta_i$ are IID, ΔX_i is uniformly distributed in $b(0, r_{\text{move}})$, r_{move} is the maximum range of movements, $\Delta\Theta_i$ is uniformly distributed in $[-\omega, \omega]$. Our local mobility model includes both translation and rotation of users. Users may follow different mobility patterns, e.g., moving in fixed directions or rotate at constant rate. We expect the trend scalability of stability are the same as our general simplified model.

Denote by $Y_x^t = f(x, \Theta, \tilde{\Phi}^t \backslash (x, \Theta), 0, \Theta_0)$ as a random variable representing whether user x is a strong interferer at time t, and $Y_x^{t+\Delta t}$ a random variable representing the state of the same user at $t + \Delta t$, i.e.,

$$Y_x^{t+\Delta t} = f(x + \Delta X, \Theta + \Delta\Theta, \tilde{\Phi}^{t+\Delta t} \backslash (x + \Delta X, \Theta + \Delta\Theta), \Delta X_0, \Theta_0 + \Delta\Theta_0), \tag{2.14}$$

where ΔX, $\Delta\Theta$ are random variables having the same distribution as ΔX_i and $\Delta\Theta_i$ respectively, Y_x^t and $Y_x^{t+\Delta t} \in \{0, 1\}$. We define the *stability* of an interferer originally located at x for an interval of length Δt, $S(x, \Delta t)$, based on the autocorrelation of the state of the interferer at t and $t + \Delta t$ as follows,

$$S(x, \Delta t) = \text{Corr}(Y_x^t, Y_x^{t+\Delta t}) = \frac{\text{Cov}(Y_x^t, Y_x^{t+\Delta t})}{\sigma_{Y_x^t} \cdot \sigma_{Y_x^{t+\Delta t}}}, \tag{2.15}$$

where $\text{Cov}(Y_x^t, Y_x^{t+\Delta t}) = \text{E}[Y_x^t Y_x^{t+\Delta t}] - \text{E}[Y_x^t]\,\text{E}[Y_x^{t+\Delta t}]$, is the covariance of Y_x^t and $Y_x^{t+\Delta t}$, and $\sigma_{Y_x^t}$, $\sigma_{Y_x^{t+\Delta t}}$ are the variance of Y_x^t and $Y_x^{t+\Delta t}$, $S(x, \Delta t) \in [-1, 1]$.

The stability metric we define here works as a measure on the correlation of previous measurements and current channel state. If $S(x, \Delta t)$ is small, i.e., close to 0, the correlation of the channel state of an interferer at different times, t and $t + \Delta t$, is low and the interferer channel state is unstable. In this case, previous measurements at Δt before are not reliable and the frequency of channel measurements need to be higher and the users may need to change their clustering and scheduling strategy more frequently. If $S(x, \Delta t)$ is close to 1, the correlation is high and the interferer is stable, and the overhead would be lower.

How to compute $S(x)$. Based on our assumptions that movements are IID, $\tilde{\Phi}^t$ is stationary according to the Displacement Theorem [54]. As a result,

$$\sigma^2_{Y_x^t} = \mathrm{P_{SI}}(x) \cdot \big(1 - \mathrm{P_{SI}}(x)\big), \tag{2.16}$$

where $\mathrm{P_{SI}}(x) = \Pr(f_0(x, \Theta, \tilde{\Phi}\backslash(x, \Theta), 0, \Theta_0) = 1)$. We use $\sigma^2_{Y_x^t}$ to approximate $\sigma^2_{Y_x^{t+\Delta t}}$. To compute $\mathrm{Cov}(Y_x^t, Y_x^{t+\Delta t})$, we have $\mathrm{E}[Y_x^{t+\Delta t}] \approx \mathrm{E}[Y_x^t] = \mathrm{P_{SI}}(x)$. $\mathrm{E}[Y_x^t \cdot Y_x^{t+\Delta t}]$ is the probability that user at x is strong interferer at times t and $t + \Delta t$,

$$\mathrm{E}[Y_x^t \cdot Y_x^{t+\Delta t}] = \Pr\big(\{Y_x^t = 1\} \cap \{Y_x^{t+\Delta t} = 1\}\big). \tag{2.17}$$

The user at x at time t, is a strong interferer at t and $t+\Delta t$ if it is facing user 0 and the channel between them is not blocked at t and $t + \Delta t$. The probability of users facing each other can be computed by taking the expectation over $\Theta_0, \Theta, \Delta\Theta_0, \Delta\Theta$. Let us denote $N_{\mathrm{B}}^{t,t+\Delta t}$ as the number of users blocking the channel between user x and user 0 at t or $t + \Delta t$. Since $\tilde{\Phi}^t$ is IMPP and

the movements are IID, it follows that $N_{\mathrm{B}}^{t,t+\Delta t}$ has a Poisson distribution and $\mathrm{E}[N_{\mathrm{B}}^{t,t+\Delta t}]$ can be computed using Campbell's formula and the mobility model.

We consider two metrics for the stability of strong interferers based on $S(x)$. The first metric is the stability of strong interferers at a given distance, d, i.e.,

$$\mathrm{E}\left[S(x,\Delta t)\middle||x|=d\right]. \tag{2.18}$$

The second metric we consider, is the stability of a random LOS strong interferer, $\mathrm{E}[S]$,

$$\mathrm{E}[S] = \frac{\lambda \int_{\mathbb{R}^2 \setminus b(0,r_{\min})} S(x,\Delta t)\cdot \mathrm{P}_{\mathrm{SI}}(x)\mathrm{d}x}{\mathrm{E}[N_{\mathrm{SI}}]}. \tag{2.19}$$

$\mathrm{E}[S]$ is the average sensitivity of the strong interferers normalized by the probability that a user is a strong interferer. This metric estimates the average stability of the interferers that user tracks and the coordination costs for tracking a neighboring strong interferer.

2.2.3 Numerical Results on Interference

We first present the numerical results for the number of strong interferers. In a dense scenario, the HPPP may not be a good model for user locations as users in reality will not overlap with each other. This may affect the accuracy of our model for $\mathrm{E}[N_{\mathrm{SI}}]$. In Fig. 2.5 we compare our analytical results with simulation results in which the users are excluded from overlapping. For these numerical and simulation results, users are modeled as cylinders with a diameter of 0.6 m, and we use Matérn III process [55] to model the user locations in our simulation and the minimum distance between users is 0.6 m to prevent

overlapping. $h_{\text{body}} = 1.754\,\text{m}$, $h_{\text{device}} = 1\,\text{m}$, $h_{\text{ceiling}} = 2.8\,\text{m}$, $|\Gamma|^2 = 0.2166$, $\alpha = 4\pi/3$. PBSSs work in the 60GHz band and the threshold of path loss for strong interferers is -88 dB, i.e., $r_{\max} = 10\,\text{m}$, and $r_{\max}^{\text{reflection}} = 3.1\,\text{m}$. The average sum interference in (b) is from analysis using the same analytical model, transmit power is 20 dB, antenna gain is $G_t = G_r = 0$ dB. As can be seen, our analytical results are in line with the simulation, validating the accuracy of the approximation by the HPPP. Also as can be seen, $\mathrm{E}[N_{\text{SI}}]$ first grows with the user density, but as user density further increases, close by neighbors block the interference from more distant users, thus $\mathrm{E}[N_{\text{SI}}]$ saturates and begins to decrease with density. Users see the largest number of strong interferers at moderately high user densities. By contrast, the average sum interference a typical user receives is increasing with the user density, see Fig. 2.5(b), which is in line with the results in [19, 20]. The trend for $\mathrm{E}[N_{\text{SI}}]$ is similar for the case where users use directional transmissions.

To understand the reasons behind these phenomena, we study how the distribution of strong interferers changes in the user density in Fig. 2.6 and Fig. 2.7. Fig. 2.6 illustrates the distribution for the distance of LOS strong interferers for varying user densities. Fig. 2.7 shows the locations of strong interferers in one realization of the network. As user density increases, the strong interferers tend to concentrate close to the receiver. When the user density is very high, the network reaches a "jamming regime", where strong interferers are mostly close by and block further away interferers as shown in Fig. 2.7(c). This also helps explain the results in Fig. 2.5(b): although the

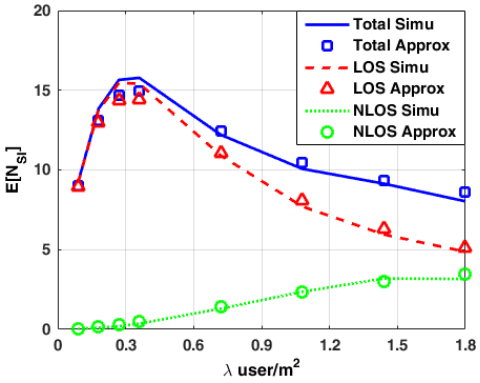

(a) Expected number of strong interferers

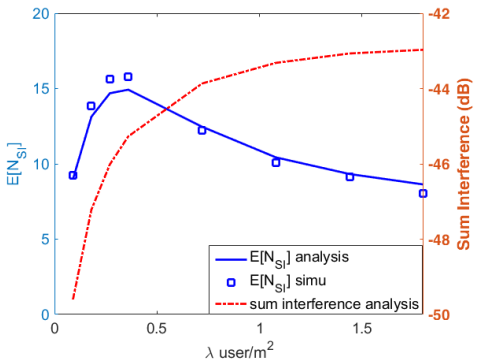

(b) Number of strong interferers v.s. average sum interference

Figure 2.5: (a) How $\mathrm{E}[N_{\mathrm{SI}}]$ changes with user density, and (b) comparison of $\mathrm{E}[N_{\mathrm{SI}}]$ and sum interference from other users.

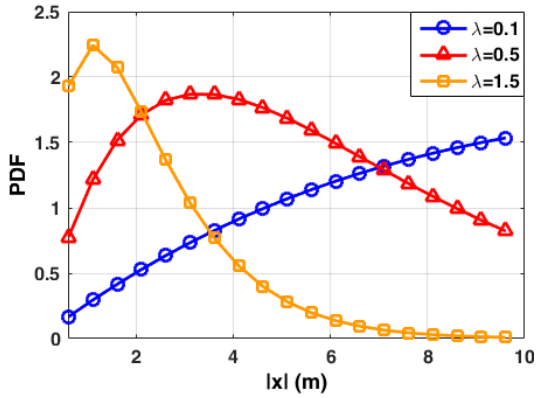

Figure 2.6: Probability density function of LOS strong interferers as a function of the distance to the reference user at 0, $|x|$.

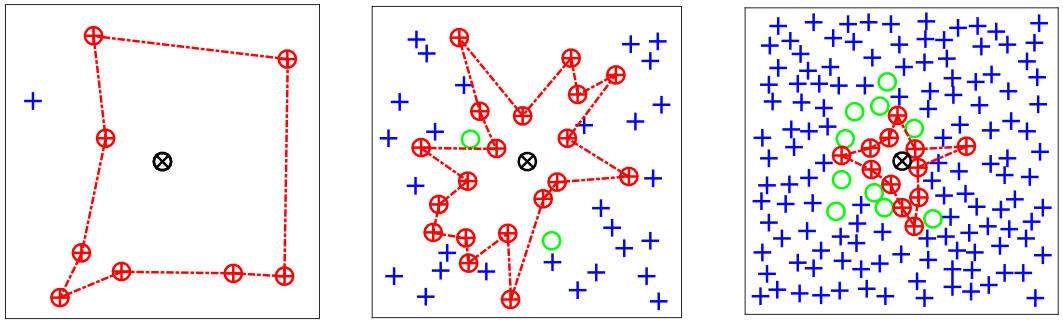

(a) $\lambda = 0.1/m^2$ (b) $\lambda = 0.5/m^2$ (c) $\lambda = 1.5/m^2$

Figure 2.7: The locations of strong interferers for different densities, neglecting self blockage. The joint red circles represent LOS interferers, green hollow circles are NLOS interferers and blue crosses are non strong interferers. The area shown above is 10m $\times$ 10m.

number of strong interferers is limited as the density grows, they get closer and each contributes an increasing amount of interference, resulting in a sum interference which increases in the user density. These results imply that at high user densities we might be able to mitigate interference with appropriate MAC schedulers since there are only a small number of strong interferers. In addition, the MAC coordination costs might not be too high.

We present the numerical results on the stability of LOS strong interferers in Fig. 2.8. For these results, Δt was set to be 1s. We assumed r_{move} is a function of λ and may decrease at high user densities, i.e.,

$$r_{\text{move}}(\lambda) = \begin{cases} 0.2\,\text{m} & \text{if } \lambda \leq 0.71/\text{m}^2 \\ 0.6\left(\sqrt{\frac{0.9}{\pi\lambda}} - 0.3\right)\text{m} & \text{if } \lambda > 0.71/\text{m}^2 \end{cases}.$$

In our model for r_{move}, the range of user translation is fixed at low user densities, i.e., $r_{\text{move}} = 0.2\,\text{m}$, since the distance among users is large and the local

movements of users are less likely to be constraint by other users. At high user densities, users are close to each other and the movements of users are assumed to be more limited. Assuming each user occupies a circle centered at the user's initial location and the circles of different users do not overlap, then, in the dense packing case, the radius of the circle is approximately $\sqrt{0.9/\lambda\pi}$ and the maximum range of movement is $r_{\text{move}}^{\max}(\lambda) = (\sqrt{0.9/\lambda\pi} - r_{\text{body}})m$, where $r_{\text{body}} = 0.3$m is the radius of user body. Thus we set $r_{\text{move}} = 0.6 \cdot r_{\text{move}}^{\max}(\lambda)$. This rough model captures the impact of the limitations of local movements at high densities. The range for rotation was assumed to be 48, i.e., $\omega = 24$.

Fig. 2.8(a) exhibits the stability of users at different distances. As can be seen, close by interferers are more stable to user movements than distant interferers. This supports the observation that closely interferers will be robust to movements and information regarding interference from closely neighbors is more reliable. Fig. 2.8(b) exhibits the stability of a typical strong interferer, E[S], for different user densities. Strong interferers first become less stable as $S(x, \Delta t)$ decreases with λ. In highly dense scenarios, strong interferers are closer and their movements are more constraint, thus effectively the strong interferers are more "stable". Our numerical results show that coordination with closely neighbors may work well in dense wearable settings as the channels are relative stable and the coordination costs are limited. If the movement of users scale differently with user density, e.g., r_{move} does not change with λ, stability may keep decreasing with user density. The rate of decrease is smaller at high densities as long as user mobility does not increase with user density.

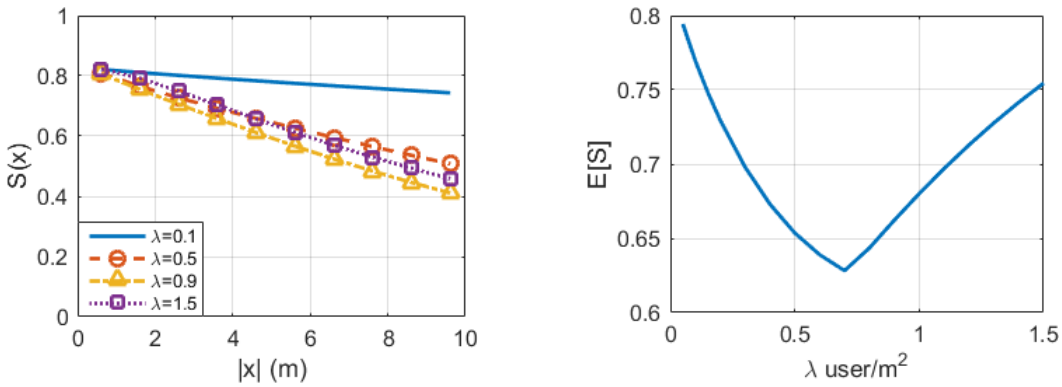

(a) Stability of user x

(b) Average stability of strong interferers

Figure 2.8: (a) Stability of users at different distance $|x|$, and (b) average stability of a typical strong interferer $\mathrm{E}[S]$ for different user densities.

Our results here implicate the possibility that stability may not monotonically decrease with user density and in dense environments the stability of channels may increase as movements are limited. Our focus here is on dynamics of wearable networks under small scale local movements. We study the impact of large scale movements, e.g., walking, in Chapter 3

2.3 Hierarchical Wearable MAC

In this section we propose a simple model to study the performance of a hierarchical MAC protocol which uses clustering, channel selection, and hierarchical scheduling. Our model is in line with current MAC designs, e.g., the distributed clustering in 802.11ad, but optimized for dense wearable settings based on our findings in the previous section.

2.3.1 Hierarchical MAC for Wearable Networks

When centralized control is absent, hierarchical clustering and scheduling work as a viable solution to coordinating transmissions amongst multiple PBSSs, see e.g., the distributed clustering in 802.11ad [2].

A hierarchical MAC consists of three parts, clustering, channel selection and scheduling at each PBSS. PBSSs form clusters, while the cluster head synchronizes the PBSSs in the cluster and schedules Beacon Transmission Intervals (BTIs) for each cluster member PBSS, see Fig. 2.9. Cluster heads do not schedule the data transmissions of cluster members. Channel selection is mainly used to mitigate interference among clusters and performed by the cluster heads. Clustering and channel selection help coordinate the PBSSs and are usually performed at a slower time scale. In each PBSS, the PCP schedules the data transmissions within the PBSS for each frame while trying to optimize reuse in dense scenarios.

To optimize MAC performance in wearable networks, e.g., handling blockage and improving reuse, we propose the following MAC.

Clustering and channel selection. For dense wearable networks, the basic principle underlying clustering is that the channels among the cluster head and cluster members should be strong and stable. To better mitigate inter-cluster interference through channel selection, it is also desirable that cluster members share a similar set of strong interferers. Based on our analysis of the interference environment and the above principles, a cluster shall consist

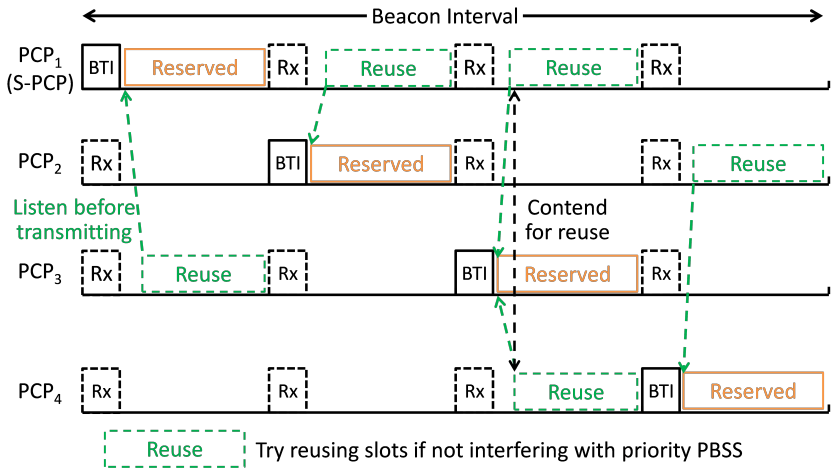

Figure 2.9: Frame structure of clustering with Hierarchical Resource Reuse.

of users in close proximity and operate in a channel distinct from that of nearby clusters.

Scheduling within clusters. Wearable devices on a user may have different quality of service (QoS) requirements and transmission capabilities. High end devices may have more directional transmissions and require high data rates and low latency. Low end devices, on the other hand, may use less directional transmissions and do not have strict QoS requirements. To achieve better resource reuse within each cluster and meet the basic QoS requirements of different types of devices in each PBSS, we propose the hierarchical scheduling method exhibited in Fig. 2.9. Our scheduling method follows the same basic structure as that in 802.11ad. The cluster head synchronizes the Beacon Interval (BI) for PBSSs in the cluster and schedules slots for Beacon Transmission Intervals (BTIs). In each BTI, only one PCP transmits its bea-

cons while other users listen to the beacons. The slots after the BTI (before the next BTI) are allocated to the PBSS that just sends the beacon, during which the PBSS has priority over the other PBSSs. The PBSS starts data transmission after sending the BTI. Other PBSSs may however try to contend with other non-priority PBSSs to reuse the slots if the their transmissions do not interfere with the transmissions of the priority PBSS. Non-priority PBSSs will first measure the channel and try to access the channel if they are not interfering with a priority user. To avoid interference among non-priority PBSSs, non-priority PBSSs may take turns in attempting to access the channel. A non-priority PBSS needs to avoid interference with any PBSSs that has accessed the channel in the cluster.

2.3.2 Modeling the Achievable Reuse for Hierarchical MAC Scheduling

We propose a model to compute the achievable reuse of our proposed MAC for dense wearable networks. Let us consider the average time that a PBSS can perform a successful data transmissions, denoted by *Successful Transmission Time (STT)* , as the performance metric of interest. A PBSS interferes with another PBSS if the interference power it causes at the receiver is above a threshold γ_{SI}. We say two users interfere with each other if either user is interfering with the other. Under this simplified model, a transmission is successful if there is no strong interferer. STT is then defined as follows,

$$STT = f_{\mathrm{data}} \times p_{\mathrm{access}} \times p_{\mathrm{success}}, \tag{2.20}$$

where f_{data} is the fraction of time reserved for data transmission, p_{access} is the probability that a PBSS in a given cluster may access the channel, with no intra-cluster interference after scheduling, and p_{success} is the probability that a data transmission is successful. We use the "protocol model" to decide whether a transmission is successful, i.e., a transmission is successful if the receiver does not see a strong interferer, which causes interference stronger than γ_{SI}. In dense wearable networks, due to blockage and directional transmissions, interference is dominated by a few strong interferers, and we suppose the criterion above is a good approximation for an SINR based criterion if an appropriate γ_{SI} is used.

There are two types of transmissions, beacon and data transmissions. To account for the heterogeneity of devices, e.g., transmission capabilities and QoS requirements, we classify data transmissions of each PBSS into two categories, primary data transmissions with higher QoS requirements and highly directional antennas and secondary data transmissions associated with lower QoS requirements and less directional antennas.

Modeling clustering and channel selection. We assume that clusters are of the same size K and share M channels. Each cluster includes the nearest neighbors of the cluster head and when possible each cluster chooses to operate on a channel different from those used by its closest neighboring clusters. For analytical purposes, we consider a typical cluster, where the cluster head is located at the center with the other $K-1$ cluster members being its closest neighbors. MAC performance is related to the intra-cluster resource

sharing and inter-cluster interference. To obtain a tractable simple model, we assume the cluster members are uniformly distributed on a disc centered at the cluster head with a fixed radius R_{cluster}, while channel selection, geared at ensuring neighboring clusters operate on different channels, effectively forms an inter-cluster interference protection region, see Fig. 2.10. An idealized protection area is modeled as a disc centered at the cluster head with a radius R_{protect}, where there are no inter-cluster interferers. For such a model, the performance of MAC is determined by the size of the cluster disc, R_{cluster}, and the radius of the protection region, R_{protect}. R_{cluster} determines the intra-cluster interference which in turn impacts the ability of users in the cluster to access their shared channel, p_{access}. R_{protect} and the density of users on the same channel outside the protection region determines the inter-cluster interference, and the probability of a successful transmission, p_{success}.

For users in the cluster, we shall assume user density on the disc is λ, then the expected number of users on the disc should be equal to the number of cluster members, $K-1$, which permits a rough estimate of the cluster radius:

$$\lambda\pi \cdot (R_{\text{cluster}}^2 - r_{\text{min}}^2) \approx K-1 \Rightarrow R_{\text{cluster}} \approx \sqrt{\frac{K-1}{\lambda\pi} + r_{\text{min}}^2}. \tag{2.21}$$

To model inter cluster interference, we assume that the fraction of clusters operating on each channel is equal, and the number of users in the protection area of each cluster is the same. Users using other channels of course will not interferer, but still play a role as possible blockage outside the cluster disc. We further assume the protection areas of clusters on the same channel are

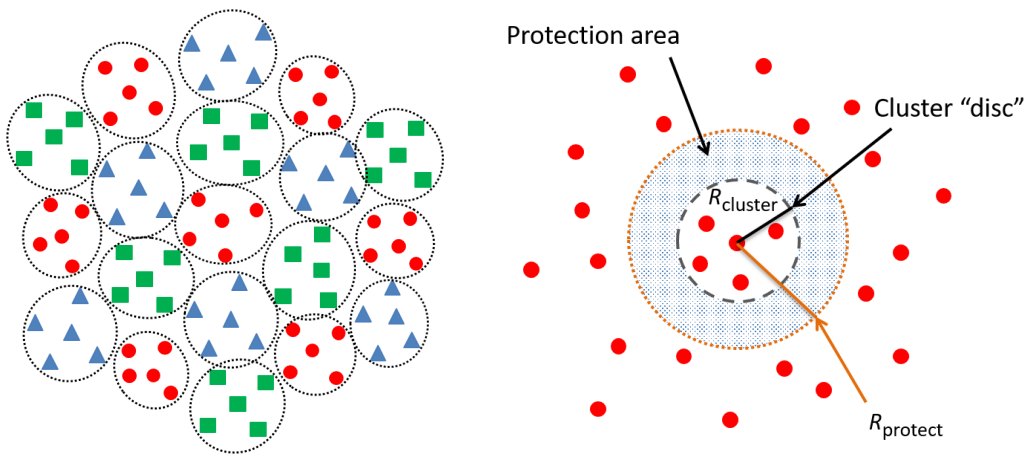

(a) Network after clustering and channel selection

(b) Analytical model for clustering

Figure 2.10: (a) illustrates the cluster and the channel each user works in after clustering and channel selection. Users of the same shape work in the same channel, while close by users in the same channel belong to the same cluster. (b) shows the analytical model for clustering and channel selection. Close by users are clustered together with the cluster head located at the center. Channel selection forms a protection area around the cluster, separating users working on the same channel. Interfering users on the same channel can be viewed as randomly located outside the protection area with density λ/M and working independently.

non-overlapping, thus on average there should be $M \cdot K$ users in the protection area. Suppose these users are uniformly distributed in the protection area with density λ, then under our idealized model, one can get a rough estimate of the protection radius:

$$\begin{aligned} &\lambda\pi \cdot (R_{\text{protect}}^2 - r_{\min}^2) \approx M \cdot K - 1 \\ &\Rightarrow R_{\text{protect}} \approx \sqrt{\frac{M \cdot K - 1}{\lambda\pi} + r_{\min}^2}. \end{aligned} \tag{2.22}$$

We shall assume users outside the protection area can be modeled as following an HPPP with density λ and operating on a given channel with probability $1/M$. All PBSSs outside the protection region are treated as working independently.

Modeling scheduling. We assume that there is at most one transmission in each PBSS in each slot. Let T_{frame} denote the length of a frame and T_{beacon} denote the length of beacon transmission time for one PBSS, see Fig. 2.9. The cluster head reserves exactly K BTIs in T_{frame} thus the fraction of time reserved for data transmission is given by

$$f_{\text{data}} = \frac{T_{\text{data}}}{T_{\text{frame}}} = \frac{T_{\text{frame}} - K \cdot T_{\text{beacon}}}{T_{\text{frame}}}. \tag{2.23}$$

When one PCP transmits its beacon, the other PCPs attempt to receive the beacon using an omni-directional receive mode. The PBSSs are assumed to have full buffers and schedule primary data transmissions a proportion $\rho_{\text{primary}} \in [0, 1]$ of slots and schedule secondary transmissions for the remaining $\rho_{\text{secondary}} = 1 - \rho_{\text{primary}}$ of the slots.

We will consider two types of scheduling within clusters: time division multiple access (TDMA) and hierarchical resource reuse (HRR). In TDMA scheduling, PBSSs share the slots equally within the cluster and the fraction of time that a PBSS can access the channel in a frame is given by,

$$p_{\text{access}}^{\text{TDMA}} = \frac{f_{\text{data}}}{K}. \tag{2.24}$$

Thus overall a PBSS schedules primary transmissions in $\rho_{\text{primary}} f_{\text{data}}/K$ slots, and secondary transmissions in the rest $(1 - \rho_{\text{primary}}) f_{\text{data}}/K$ slots.

In HRR, each PBSS is allocated $1/K$ of the slots where it is priority PBSS, i.e., having higher priority in scheduling. A PBSS first schedules primary transmissions in the reserved slots and schedules other transmissions by reusing slots allocated to other PBSSs. If $\rho_{\text{primary}} \leq 1/K$, the PBSS also schedules secondary transmissions in the slots not allocated for primary transmission. Otherwise PBSSs also try to reuse the slots if they do not interfere with the priority PBSS assigned to the slot. We shall chose a user located $\frac{\sqrt{2}}{2} R_{\text{cluster}}$ away from the cluster head as a representative user for the cluster. Such users capture what is "typically" achievable in the cluster, i.e., p_{access}, p_{success}, and thus STT. The probability that the representative PBSS can reuse a given slot can then be approximated by

$$p_{\text{access}}^{\text{reuse}} \approx \frac{1 - p_{\text{SI}}^{\text{priority}}}{1 + \text{E}[N_{\text{intra-cluster}}^{\text{reuse}}]}. \tag{2.25}$$

In the above, $p_{\text{SI}}^{\text{priority}}$ is the average probability that the representative user interferes with the priority user considering the channel path loss and antenna

gain, The random variable $N^{\text{reuse}}_{\text{intra-cluster}}$ denotes the number of non-priority PBSSs in the cluster, which do not interfere with the priority PBSS but interfere and contend with the representative PBSS to reuse the slot.

We further denote by $N_{\text{inter-cluster}}$ the number of inter-cluster interfering PBSSs seen by the representative PBSS. The transmission states of inter-cluster interferers outside the protection region are assumed to be mutually independent and the blockage states of their channels to the representative PBSS are assumed to be independent. It follows by the thinning property of Poisson process that $N_{\text{inter-cluster}}$ has a Poisson distribution and the probability of a successful transmission is given by,

$$p_{\text{success}} = e^{-\,\mathrm{E}[N_{\text{inter-cluster}}]}. \tag{2.26}$$

The distribution of $N_{\text{inter-cluster}}$ is related to the channel access probability of interfering PBSSs, and we assume all PBSSs outside the cluster on the same channel have the same channel access probability as the representative user.

2.3.3 Numerical Results and Discussion

In this section, we present results on the achievable STT of the representative user. We assume the secondary transmissions use omni-directional antenna and low transmit power while primary transmissions use directional antenna with $\beta =$, $\rho_{\text{primary}} = 0.5$. The other parameters used are listed in Table 2.3.3.

We begin by comparing our analytical model with simulations in Fig. 2.11.

Table 2.1: Parameters in wearable MAC performance analysis

Parameter	Value
Frequency	60 GHz
M	4
λ	1 user/m^2
P_t (primary)	10 dBm
P_t (secondary)	4 dBm
γ_{SI}	-78 dBm
g_{main} ($\beta = 60$)	5 dB
g_{side} ($\beta = 60$)	-5 dB
g_{main} ($\beta = 24$)	10 dB
g_{side} ($\beta = 24$)	-10 dB
T_{frame}	100 ms
T_{beacon}	2 ms

In our simulation, the locations of users follow a Matérn III process [55], i.e., users can not overlap each other. The blockage from other users follows the probabilistic model based on distance while self-blockage and antenna gain are calculated based on user locations and orientations and antenna directions. Users are first clustered using Affinity Propagation (AP) [56] based on a similarity metric between two users i and j, which is simply defined as the inverse squared distance, i.e., d_{ij}^{-2}, where d_{ij} is the distance between user i and j. The clustering algorithm used in our simulated MAC protocol requires the distance to other users to compute the similarity and implement the distributed clustering algorithm. In reality, users would estimate similarity metrics (not necessarily distance) based on channel measurements. After clustering, the cluster heads hop among channels, attempting to minimize the sum similarity between the cluster head and other users operating on the same channel but

which do not belong to its cluster. Channel selection is performed until cluster head choices stabilize. After clustering and channel selection, each cluster schedules users either using TDMA or HRR. In HRR, each non-priority PBSS is assigned a random reuse-priority, and a non-priority PBSS user can reuse the channel if it does not interfere with the priority PBSS, nor other non-priority PBSSs which have higher reuse priority and can access the channel for reuse. As shown in Fig. 2.11, the simulation results for this more realistic network model, e.g., with real clusters, channel selection and scheduling, are in accordance with our simplified analytical model.

Trade-offs associated with cluster size. Fig. 2.11 exhibits how the STT changes with cluster size. As can be seen the STT first increases with cluster size, then saturates and decreases, indicating that although large clusters may provide good inter-cluster interference mitigation, they increase the contention between users within a cluster as well as signaling overheads thus may reduce the spatial reuse.

In Fig. 2.12 we present the p_{success} for different cluster sizes. As expected, p_{success} increases with cluster size, as larger cluster sizes increase the size of the protection region and decrease interference. When using HRR, the interference is higher, thus p_{success} is smaller than that achieved under TDMA. We also observe that primary data transmission has larger p_{success} than secondary data transmissions as the transmit power and antenna gains are higher.

Impact of transmission capability of devices. Fig. 2.13 exhibits the STT when users have different beamwidths β for their primary transmissions. As

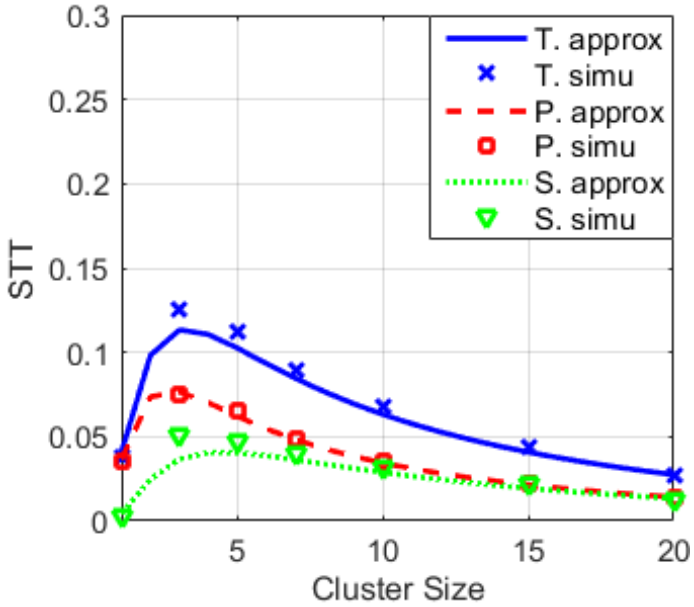

(a) STT in TDMA

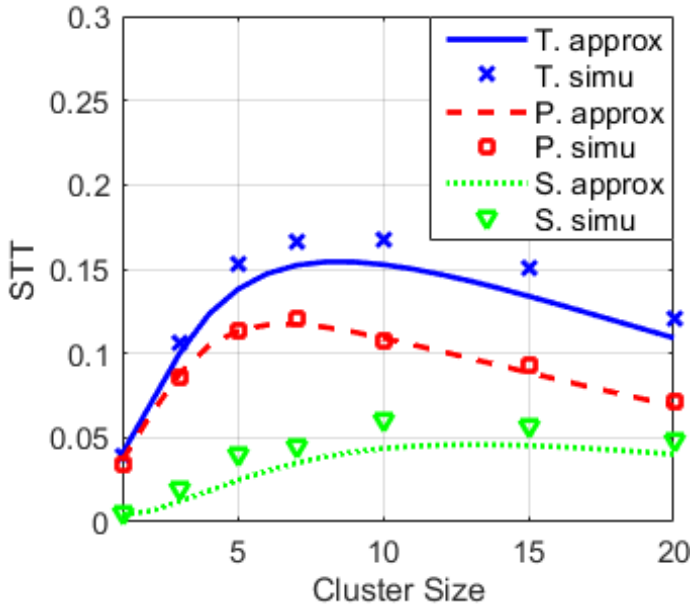

(b) STT in HRR

Figure 2.11: Total STT (T.), STT of primary transmissions (P.) and STT of secondary transmissions (S.) in TDMA and HRR for different cluster sizes.

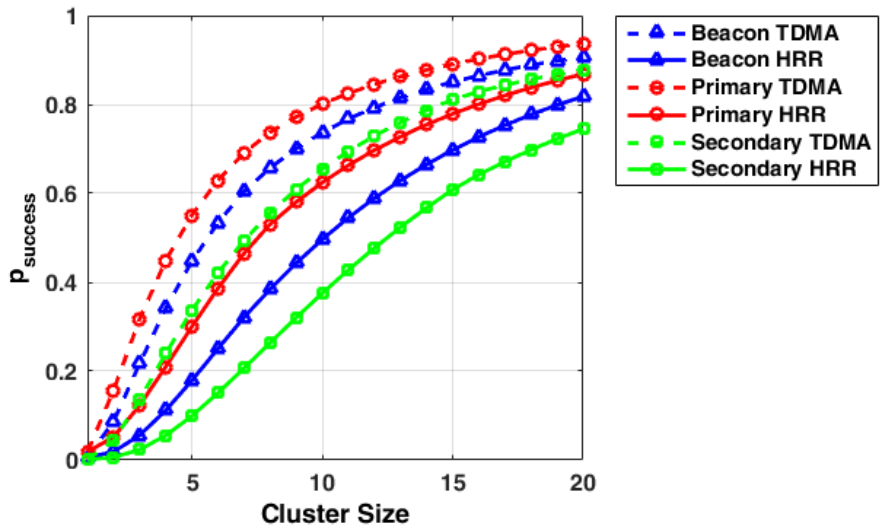

Figure 2.12: p_{success} for different cluster sizes.

might be expected, the optimal cluster size maximizing STT is smaller when the transmissions are more directional. Results suggest that highly directional devices are less dependent on clustering to mitigate interference, thus users with highly directional devices may favor small clusters or be better off not joining clusters at all.

Optimal cluster size v.s. user density. In Fig. 2.14 we show how the cluster size maximizing the sum STT of primary and secondary transmissions changes with user density. When user density is high, the optimal cluster size does not change very much. Indicating that in such regimes, a fixed near optimal cluster size can be chosen for a range of user densities – i.e. robust choice. Furthermore, since overheads increase in cluster size, the results suggest that for high densities, these overheads scale well. However, as we have discussed, the transmission capabilities of users influence the optimal cluster

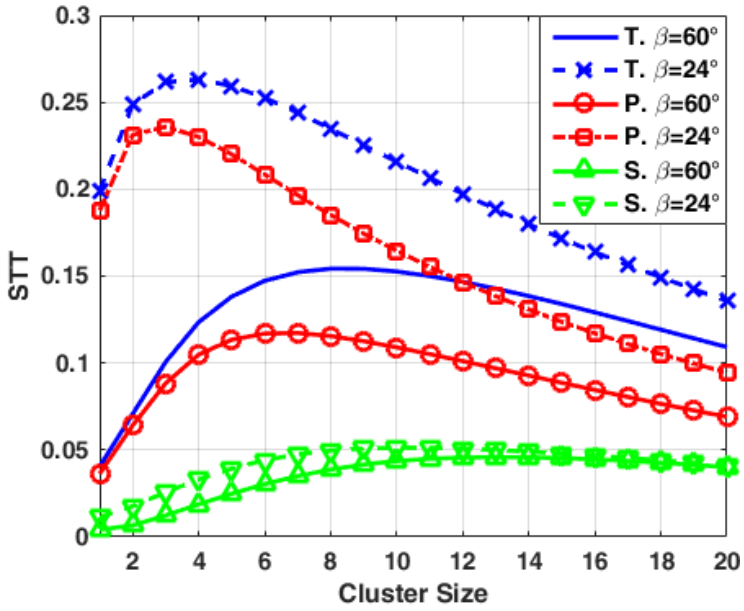

Figure 2.13: Comparison of STT for networks with different beamwidths β for primary transmissions.

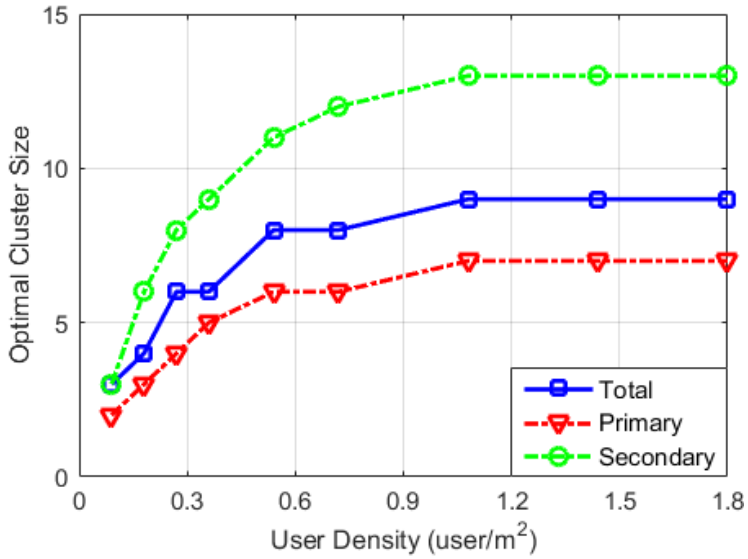

Figure 2.14: Cluster size that maximizes STT for different user densities.

size.

STT v.s. user density. In Fig. 2.15 we compare the STT for different MAC protocols, i.e., clustering+TDMA, cluster+HRR, and optimal Aloha, at different user densities. In clustering based protocols, the cluster size is chosen as the one that maximizes the STT at the user density. For optimal Aloha, channel access probability is chosen to maximize average STT, and we assume users select channels randomly. We observe that clustering and reuse provide moderate gains in STT, i.e., 50% over optimized Aloha, partly due to beacon overheads. The STT of users remains roughly constant with user densities, indicating that the per user throughput scales nicely at high densities. Combined with the observation that coordination costs saturate, we conclude that MAC schedulers for mmWave wearable network will be scalable.

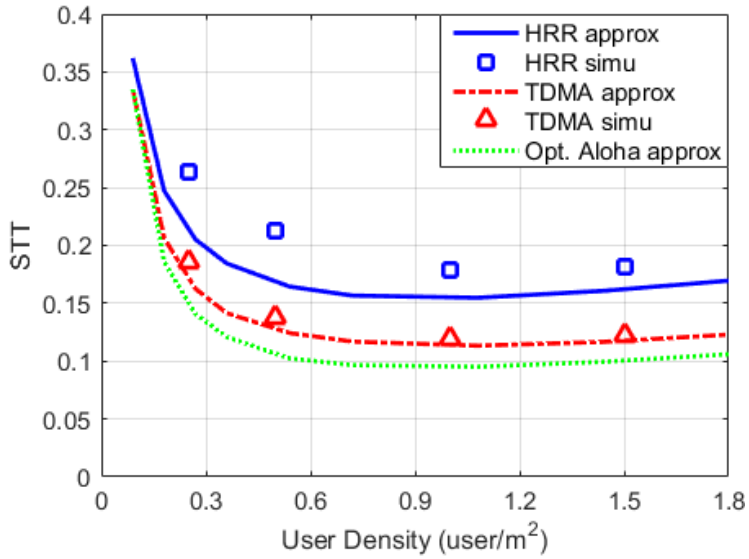

Figure 2.15: STT in different user densities for different MAC protocols: clustering+HRR, clustering+TDMA and optimal Aloha. In optimal Aloha, the channel access probability is optimized to maximize STT.

Compared with [19, 20], which assume all users contend, our results show that MAC scheduler can make user throughput scalable.

2.4 Conclusion

Our analysis of the character of interference and MAC performance in dense mmWave wearable networks suggests such networks might be quite viable for a range of user densities. Blockage and directionality help limit the number of strong interferers to a few that are close by and stable. For a relative stationary network, clustering with resource reuse is a viable solution to coordinating PBSS transmissions. An ideal cluster protocol should cluster close by stable and strong interfering neighbors and possibly adapt to users'

beamforming capabilities and QoS requirements. More importantly, the coordination costs and performance of MAC scale well at high densities. In fact when designing and evaluating a MAC design, one may want to focus on the most challenging scenario, i.e., one with a moderate density of users.

Chapter 3

Temporal Dynamics of Mobile Blocking in Millimeter Wave Based Wearable Networks[1]

In this chapter we characterize the temporal dynamics of mmWave based channels caused by large scale movements of blockages.

3.1 System Model and Background Results

In this section we introduce our system model for a mmWave network with mobile users along with some fundamental background results that are critical to have a clear understanding of the results in this chapter.

[1]This chapter is based on paper: Yicong Wang and Gustavo de Veciana, "Temporal dynamics of mobile blocking in millimeter wave based wearable networks," in *15th International Symposium on Modeling and Optimization in Mobile, Ad Hoc, and Wireless Networks (WiOpt)*, Paris, France, 2017. Prof. de Veciana supervised the project.

3.1.1 Background Notation and Key Results

We introduce some notations for set operations, see [53]. For $x \in \mathbb{R}^2$, $A, B \subset \mathbb{R}^2$,

$$A \oplus B = \{x + y : x \in A, y \in B\}, \tag{3.1}$$

$$x + B = \{x + y : y \in B\}, \tag{3.2}$$

$$\check{B} = \{x : -x \in B\}. \tag{3.3}$$

Here $\oplus$ denotes the Minkowski sum of sets.

The following results will be used repeatedly in the sequel and are fairly well known in the literature:

- Displacement Theorem in $\mathbb{R}^2$ [54]
- Boolean Model in $\mathbb{R}^2$ [57]
- Generalized Steiner Formula in $\mathbb{R}^2$ [57]

The above results provide the following key insights in the context of modeling mobile blockages. Displacement theorem indicates that starting with a Homogeneous Poisson Point Process (HPPP) of blockages locations, randomly displacing blockages gives another HPPP. If a set of blockages can be modeled as a Poisson Boolean Process in Boolean model, the number of such blockages intersecting a set follows a Poisson distribution. Generalized Steiner formula helps calculate the expected area of the Minkowski sum of random sets.

3.1.2 System Model

We use a similar model for wearable network as that in Chapter 2. Each user is equipped with multiple wearable devices. The devices on each user are assumed to form a Personal Basic Service Set (PBSS), coordinated by the PBSS Control Point (PCP), e.g., the user's smart phone. Data transmissions only happen between the PCP and non-PCP devices of the same PBSS. We shall assume each user is equipped with a device, e.g., a smart phone, which serves as coordinator for the user's wearable devices. The coordinating device will be assumed to be located in front of the user's body. We shall consider channels amongst the centers of users as approximating the channels among devices associated with different users.

We shall consider networks composed of two types of users, fixed and mobile users. Due to the low transmit power and high attenuation in the mmWave band, the maximum range of a potential interferer is limited in wearable networks, e.g., 10m. Consider a channel within this limited range, the movements of users/blockages can be approximated as constant velocity movements, i.e., the velocity and the direction of the blockages at that scale may be assumed to be fixed. We refer to this mobility model as the Constant Velocity Model (CVM)[2].

Channel model. We shall focus on the LOS channels in this work. We also consider human bodies as the main source of blockages. Human body

[2]Our analysis and results still hold if the direction of movement is fixed while the speed changes.

introduces more than 20dB path loss [13] thus we assume an LOS channel is unavailable if a human is in the way. In fact the blockage model in our analysis may also represent blockages other than human bodies. In the mmWave band, the path loss of NLOS channels are typically dominated by a few major reflected paths. The blockage of reflected channels over the floor and ceiling are typically also coupled with the blockage state of the LOS channel. For other reflected paths, e.g., reflection over the wall, we may assume they are independent of the LOS channel and approximate the temporal variation using the model for LOS channels. However such NLOS channels are much weaker than the LOS channel due to longer path and reflection loss and are more likely to be blocked. In this initial work, we do not consider the diffraction of signals and NLOS channels. Self blockage is independent of other blockages thus in the sequel, we focus on the channels that are not self blocked by default. The impact of channel variation caused by self blockage and users' small local movement is studied in Chapter 2.

Location and shape of user cross section. We suppose the blockages are cylindrical and focus on the blockage on LOS channels. For simplicity we consider 2D model in our analysis. Suppose users are randomly located on $\mathbb{R}^2$ where the centers of fixed users are $\Phi^f = \{X_i^f\} \sim HPPP(\lambda^f)$ and centers of mobile users at time 0 are $\Phi^m = \{X_i^m\} \sim HPPP(\lambda^m)$. We further assume Φ^m is independent of Φ^f and mobile users' movements are independent, e.g., users can overlap with each other.

Denote by A_i^f (A_i^m) random closed convex sets modeling the shape of

fixed (mobile) user i's cross section. A_i^f (A_i^m) is centered at 0 and we denote by Θ_i^f (Θ_i^m) the random direction user i is facing. A_i^f, A_i^m are independent and identically distributed (IID) as are Θ_i^f, Θ_i^m, which are assumed to be uniformly distributed in $[0, 2\pi]$.

Mobility model. We let the random variable S_i^m model the speed of mobile user i, be IID, and such that $S_i^m \in [s_{\min}, s_{\max}]$ where $0 < s_{\min} \leq s_{\max} < \infty$. Mobile user i is assumed to move in its facing direction Θ_i^m. Denote by $W_i^m \in \mathbb{R}$ the width of mobile user i as viewed from the facing direction Θ_i^m, and $V_i^m \in \mathbb{R}^2$ its velocity vector, i.e.,

$$V_i^m = \left(S_i^m \cos\Theta_i^m, S_i^m \sin\Theta_i^m\right). \tag{3.4}$$

See Fig. 3.1a for an illustration of user body model. We shall further let $X_i^m(t)$ denote location of the center of mobile user i at time t, $t \geq 0$, thus

$$X_i^m(t) = X_i^m + t \cdot V_i^m. \tag{3.5}$$

The mobility model here corresponds to scenarios where users' movements are independent and random, e.g., crowded airport/shopping mall. Our model and analysis can also be extended to other mobility models, e.g., blockages move in the same direction.

The locations, cross sections, facing directions and velocities, of fixed and mobile users at time 0 can be represented by two independent Independently Marked Poisson Point Processes (IMPPP) [57], $\tilde{\Phi}^f$ and $\tilde{\Phi}^m$, given by

$$\tilde{\Phi}^f = \{(X_i^f, A_i^f, \Theta_i^f)\},$$
$$\tilde{\Phi}^m = \{(X_i^m, A_i^m, \Theta_i^m, S_i^m)\}.$$

Denote by $\Phi^m(t)$ the point process representing the locations of mobile users at time t, $\tilde{\Phi}^m(t)$ the marked point process for mobile users at t. It follows immediately from the Displacement theorem [54] that $\Phi^m(t)$ is also an HPPP with intensity λ^m and we have the following proposition.

Proposition 3.1.1. *Users make constant velocity movements, $\tilde{\Phi}^m$ is an IMPPP with intensity λ^m and Θ_i^m and S_i^m are IID, then at any time t $\tilde{\Phi}^m(t)$ is an IMPPP with the same distribution.*

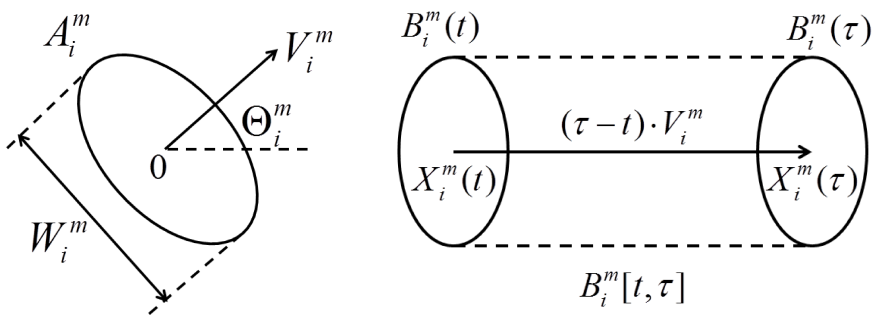

(a) User body. (b) User trace.

Figure 3.1: (a) Model for mobile user i. A_i^m is centered at 0 and the actual cross section of mobile user i is $X_i^m + A_i^m$. $V_i^m = (S_i^m \cos\Theta_i^m, S_i^m \sin\Theta_i^m)$. (b) Trace of mobile user i in $[t,\tau]$, $B_i^m[t,\tau]$.

Blockage model. We shall for simplicity assume a channel is blocked if a blockage intersects the LOS channel between two devices. Let $x \in \mathbb{R}^2$ and $l_{0,x} \subset \mathbb{R}^2$ be the line segment between 0 and x, representing the LOS channel between the two points. We shall let B_i^f and B_i^m, denote the region that fixed/mobile user i occupies at time 0, i.e.,

$$B_i^f = X_i^f + A_i^f \text{ and } B_i^m = X_i^m + A_i^m. \tag{3.6}$$

We further let $B_i^m(t)$ denote the region mobile user i occupies at time t, where

$$B_i^m(t) = B_i^m + t \cdot V_i^m = X_i^m(t) + A_i^m. \tag{3.7}$$

We say the channel between 0 and x is blocked at time t by mobile user i if $B_i^m(t) \cap l_{0,x} \neq \emptyset$ and for fixed user i if $B_i^f \cap l_{0,x} \neq \emptyset$.

Blockage traces. An important metric to capture interference temporal variation is the rate at which new blockages are seen by a channel. To compute these rates we shall determine if a mobile blockage i has blocked the channel in a given interval $[t, \tau]$, $t \leq \tau$, by defining the *blockage trace* in that time interval, denoted by $B_i^m[t, \tau]$ given by

$$\begin{aligned} B_i^m[t,\tau] &= \bigcup_{t \leq z \leq \tau} B_i^m(z) = \bigcup_{t \leq z \leq \tau} \big(A_i^m + X_i^m(z)\big) \\ &= A_i^m \oplus l_{X_i^m(t), X_i^m(\tau)} = X_i^m(t) + \big(A_i^m \oplus l_{0,(\tau-t)V_i^m}\big), \end{aligned} \tag{3.8}$$

see Fig. 3.1b. Clearly mobile user i has blocked channel $l_{0,x}$ in $[t, \tau]$ if $B_i^m[t, \tau] \cap l_{0,x} \neq \emptyset$.

To estimate the number of blockages in $[t, \tau]$ using the generalized Steiner formula, we need the area and perimeter of $B_i^m[t, \tau]$. $A_i^m(t)$ is convex and $l_{X_i^m(t), X_i^m(\tau)}$ is a line segment, thus $\nu_2(B_i^m[t, \tau])$ and $\nu_1(B_i^m[t, \tau])$ are as follows,

$$\nu_2(B_i^m[t,\tau]) = \nu_2(A_i^m) + (\tau - t) S_i^m W_i^m, \tag{3.9}$$

$$\nu_2(\partial B_i^m[t,\tau]) = \nu_1(\partial A_i^m) + 2(\tau - t) S_i^m. \tag{3.10}$$

$B_i^m[t, \tau]$ can be viewed as stretching $B_i^m(t)$ by $(\tau - t)V_i^m$, the increase in area is $(\tau - t)S_i^m W_i^m$ and the increase in perimeter is $2(\tau - t)S_i^m$.

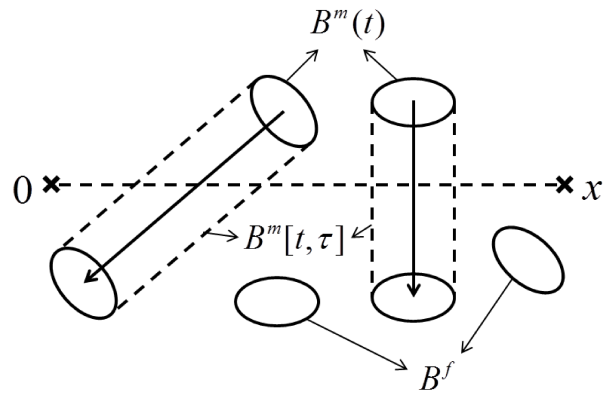

Figure 3.2: Illustration of fixed blockages B^f, mobile blockages at time t, $B^m(t)$, and traces of mobile blockages in $[t,\tau]$, $B^m[t,\tau]$. B^f, $B^m(t)$ and $B^m[t,\tau]$ are Poisson Boolean Processes.

Boolean model. Denote by B^f the region covered by all fixed users, $B^m(t)$ the region covered by mobile users at time t, $B^m[t,\tau]$ the cumulative region covered by mobile users in the time interval $[t,\tau]$, i.e.,

$$B^f = \bigcup_{i=1}^{\infty} B_i^f \qquad = \bigcup_{i=1}^{\infty} \big(X_i^f + A_i^f\big), \tag{3.11}$$

$$B^m(t) = \bigcup_{i=1}^{\infty} B_i^m(t) \quad = \bigcup_{i=1}^{\infty} \big(X_i^m(t) + A_i^m\big), \tag{3.12}$$

$$B^m[t,\tau] = \bigcup_{i=1}^{\infty} B_i^m[t,\tau] = \bigcup_{i=1}^{\infty} \big(X_i^m(t) + (A_i^m \oplus l_{0,(\tau-t)\cdot V_i^m})\big). \tag{3.13}$$

$\Phi^f, \Phi^m(t)$ are HPPPs, $A_i^f, A_i^m, A_i^m \oplus l_{0,(\tau-t)\cdot V_i^m}$ are IID random sets, thus B^f, $B^m(t)$ and $B^m[t,\tau]$ correspond to Poisson Boolean Process model [57], see Fig. 3.2.

Number of blockages. For a closed convex set $K \subset \mathbb{R}^2$, we denote by N_K^f the number of fixed users whose cross-sections intersect K, $N_K^m(t)$ the number of mobile users intersecting K at time t, $N_K^m[t,\tau]$ the cumulative number of

mobile users that have intersected K in $[t,\tau]$. N_K^f, $N_K^m(t)$ and $N_K^m[t,\tau]$ are defined as follows,

$$N_K^f = \sum_{i=1}^{\infty} \mathbb{1}(B_i^f \cap K \neq \emptyset), \tag{3.14}$$

$$N_K^m(t) = \sum_{i=1}^{\infty} \mathbb{1}(B_i^m(t) \cap K \neq \emptyset), \tag{3.15}$$

$$N_K^m[t,\tau] = \sum_{i=1}^{\infty} \mathbb{1}(B_i^m[t,\tau] \cap K \neq \emptyset) \tag{3.16}$$

Since B^f, $B^m(t)$ and $B_m[t,\tau]$ correspond to Poisson Boolean Processes, it follows by the Boolean model that N_K^f, $N_K^m(t)$ and $N_K^m[t,\tau]$ have Poisson distributions. Denote by A, Θ, S and W, random variables having the same distributions as A_i^f (A_i^m), Θ_i^f (Θ_i^m), S_i^m and W_i^m respectively. Θ is uniform in $[0,2\pi]$ thus A is isotropic and $\mathrm{E}[\nu_2(K \oplus \check{A})]$ can be computed using the generalized Steiner formula. The expected number of blockages are given as follows,

$$\mathrm{E}[N_K^f] = \lambda^f \left(\nu_2(K) + \mathrm{E}\left[\nu_2(A)\right] + \frac{\mathrm{E}\left[\nu_1(\partial A)\right] \cdot \nu_1(\partial K)}{2\pi} \right), \tag{3.17}$$

$$\mathrm{E}[N_K^m(t)] = \lambda^m \left(\nu_2(K) + \mathrm{E}\left[\nu_2(A)\right] + \frac{\mathrm{E}\left[\nu_1(\partial A)\right] \cdot \nu_1(\partial K)}{2\pi} \right), \tag{3.18}$$

$$\begin{aligned} \mathrm{E}\left[N_K^m[t,\tau]\right] = \lambda^m \Bigg(& \nu_2(K) + \mathrm{E}\left[\nu_2(A)\right] + (\tau - t)\,\mathrm{E}[S]\,\mathrm{E}[W] \\ & + \frac{\left(\mathrm{E}[\nu_1(\partial A)] + 2(\tau - t)\,\mathrm{E}[S]\right) \cdot \nu_1(\partial K)}{2\pi} \Bigg), \end{aligned} \tag{3.19}$$

where we use the fact that for a convex set A, $\nu_2(\check{A}) = \nu_2(A)$, $\nu_1(\partial(\check{A})) = \nu_1(\partial A)$.

Strong interfering neighbor. User located at x has a strong channel to user at 0 if $l_{0,x}$ is unobstructed, i.e., an LOS channel, and $|x| \leq r_{\max}$, where $r_{\max}$ is the maximum length of a strong channel. If $|x| > r_{\max}$, we assume the channel is weak and user at 0 can ignore such neighbors.

3.2 Time-varying Blocking for a Fixed Channel

Let us now consider the blocking state of fixed channels. Without loss of generality we consider the LOS channel between 0 and x, $l_{0,x}$, and denote by $|x|$ the length of $l_{0,x}$. The channel can be blocked by fixed and mobile blockages. We study the probability that the channel is blocked, then characterize the temporal variation in the blocking.

3.2.1 Probability of Having LOS Link

Denote by $\mathrm{P}^{\mathrm{LOS},f}_{l_{0,x}}$ the probability $l_{0,x}$ is not blocked by fixed blockages, $\mathrm{P}^{\mathrm{LOS},m}_{l_{0,x}}(t)$ the probability $l_{0,x}$ is not blocked by mobile blockages at t, $\mathrm{P}^{\mathrm{LOS}}_{l_{0,x}}(t)$ the probability $l_{0,x}$ is LOS at time t. For line segment $l_{0,x}$, $\nu_2(l_{0,x}) = 0$, $\nu_1(l_{0,x}) = 2|x|$, and the expected numbers of blockages for $l_{0,x}$ are given as follows,

$$\mathrm{E}[N^f_{l_{0,x}}] = \lambda^f \left(\mathrm{E}[\nu_2(A)] + \frac{\mathrm{E}[\nu_1(\partial A)] \cdot |x|}{\pi} \right), \tag{3.20}$$

$$\mathrm{E}[N^m_{l_{0,x}}(t)] = \lambda^m \left(\mathrm{E}[\nu_2(A)] + \frac{\mathrm{E}[\nu_1(\partial A)] \cdot |x|}{\pi} \right). \tag{3.21}$$

The probability of having LOS link is then given as follows,

$$\mathrm{P}^{\mathrm{LOS},f}_{l_{0,x}} = \mathrm{P}(N^f_{l_{0,x}} = 0) \qquad = e^{-\mathrm{E}[N^f_{l_{0,x}}]}, \tag{3.22}$$

$$\mathrm{P}^{\mathrm{LOS},m}_{l_{0,x}}(t) = \mathrm{P}(N^m_{l_{0,x}}(t) = 0) \quad = e^{-\mathrm{E}[N^m_{l_{0,x}}(t)]}, \tag{3.23}$$

$$\mathrm{P}^{\mathrm{LOS}}_{l_{0,x}}(t) = \mathrm{P}^{\mathrm{LOS},f}_{l_{0,x}} \cdot \mathrm{P}^{\mathrm{LOS},m}_{l_{0,x}}(t) = e^{-\mathrm{E}[N^f_{l_{0,x}}]-\mathrm{E}[N^m_{l_{0,x}}(t)]}. \tag{3.24}$$

3.2.2 Temporal Variation of Fixed Channels

Next we consider the temporal variation of blocking caused by mobile users. Let us assume $l_{0,x}$ is not blocked by fixed users. Under our model, a mobile blockage moves in a fixed direction, thus each blockage blocks the channel at most once. A mobile user may start to block the channel, if so it blocks the channel for some time then stops blocking. We say a blockage arrives at the channel if it begins to block the channel, i.e., the region the blockage intersects the channel. Denote by $T^m_i(l_{0,x}) \subset \mathbb{R}$ the (bounded) time interval mobile user i blocks channel $l_{0,x}$, i.e.,

$$T^m_i(l_{0,x}) = \{t \in \mathbb{R} \,|\, B^m_i(t) \cap l_{0,x} \neq \emptyset\}. \tag{3.25}$$

If the mobile user ever blocks the channel, i.e., $T^m_i(l_{0,x}) \neq \emptyset$, the mobile blockage i arrives at the channel at time $\min\{t|t \in T^m_i(l_{0,x})\}$ and leaves the channel at time $\max\{t|t \in T^m_i(l_{0,x})\}$. The duration of blocking is $|T^m_i(l_{0,x})|$.

The following theorem characterizes the temporal variation in blocking for $l_{0,x}$.

Theorem 3.2.1. *Under CVM model, if the LOS channel $l_{0,x}$ is not blocked by fixed users/blockages, then the blocking of $l_{0,x}$ is an alternating renewal process.*

The length of an LOS period, $T^{\text{LOS}}_{l_{0,x}}$, has an exponential distribution with mean

$$\mathrm{E}[T^{\text{LOS}}_{l_{0,x}}] = \frac{1}{\lambda^m \cdot \mathrm{E}[S] \cdot \big(\mathrm{E}[W] + 2|x|/\pi\big)}. \tag{3.26}$$

The length of an NLOS period, $T^{\text{NLOS}}_{l_{0,x}}$, has mean

$$\mathrm{E}[T^{\text{NLOS}}_{l_{0,x}}] = \frac{1 - \mathrm{P}^{\text{LOS},m}_{l_{0,x}}(t)}{\mathrm{P}^{\text{LOS},m}_{l_{0,x}}(t)}\, \mathrm{E}[T^{\text{LOS}}_{l_{0,x}}], \tag{3.27}$$

where $\mathrm{P}^{\text{LOS},m}_{l_{0,x}}(t)$ is given in Eq. 3.23.

To prove the theorem, we first prove the following lemma characterizing the arrivals of mobile blockages.

Lemma 3.2.2. *For a channel $l_{0,x}$ subject to CVM blockages, the arrival of mobile blockages follows a Poisson process with rate*

$$\lambda^Q_{l_{0,x}} = \lambda^m \cdot \mathrm{E}[S] \cdot (\mathrm{E}[W] + 2|x|/\pi). \tag{3.28}$$

Proof. Denote by $N^{\text{new}}_{l_{0,x}}(t,\tau]$ the number of blockages that arrive at $l_{0,x}$ during $(t,\tau]$, $\tau \geq t$. By the displacement theorem, at time t, the mobile blockages follow an HPPP. The movements of blockages are independent thus $N^{\text{new}}_{l_{0,x}}(t,\tau]$ has a Poisson distribution. Based on our definition of $N^m_K[t,\tau]$, we have that

$$N^{\text{new}}_{l_{0,x}}(t,\tau] = N^m_{l_{0,x}}[t,\tau] - N^m_{l_{0,x}}(t), \tag{3.29}$$

$$\mathrm{E}\left[N^{\text{new}}_{l_{0,x}}(t,\tau]\right] = \mathrm{E}\left[N^m_{l_{0,x}}[t,\tau]\right] - \mathrm{E}\left[N^m_{l_{0,x}}(t)\right]. \tag{3.30}$$

Using Eq. 3.18 and 3.19, $\mathrm{E}[N^{\text{new}}_{l_{0,x}}(t,\tau]]$ is given by,

$$\mathrm{E}\left[N^{\text{new}}_{l_{0,x}}(t,\tau]\right] = \lambda^m\, \mathrm{E}[S]\big(\mathrm{E}[W] + 2|x|/\pi\big)(\tau - t). \tag{3.31}$$

For any time interval $(t, \tau]$, $N_K^{\text{new}}(t, \tau]$ follows a Poisson distribution with mean proportional to $\tau - t$, thus the arrival of blockages follows a Poisson process [54]. We denote by $\lambda_{l_{0,x}}^Q$ the Poisson arrival rate of mobile blockages on link $l_{0,x}$, then we have, $\lambda_{l_{0,x}}^Q = \lambda^m \cdot \mathrm{E}[S] \cdot \big(\mathrm{E}[W] + 2|x|/\pi\big)$. □

Lemma 3.2.2 indicates, as might be expected, that the arrival rate of mobile blockages is proportional to blockage density λ^m and moving speed $\mathrm{E}[S]$. If we ignore the term for blockage width, $\mathrm{E}[W]$, the arrival rate is also proportional to link length. With Lemma 3.2.2, we can prove Theorem 3.2.1 as follows.

Proof. We can model the channel state as an $M/GI/\infty$ queue. The fixed channel can be viewed as an infinite server queue while mobile blockages are "jobs" that need service. The time that a blockage blocking the channel is "job" service time. By Lemma 3.2.2, mobile blockages follow Poisson arrival, which is memoryless (M). Furthermore, the typical time that a mobile user blocks the channel depends on the velocity and cross section of the blockage, thus has a general distribution (GI). By the CVM assumption, the movements of users are independent from each other and the time each mobile blockage blocks the channel is independent from others (infinite servers).

The state of the $M/GI/\infty$ queue captures whether the channel is LOS (on) or blocked NLOS (off), thus blocking can be modeled by an on/off renewal process, where $T_{l_{0,x}}^{\text{LOS}}$ and $T_{l_{0,x}}^{\text{NLOS}}$ are IID. In an $M/GI/\infty$ queue, the time that the queue is empty, which in our case is $T_{l_{0,x}}^{\text{LOS}}$, follows an exponential

distribution with mean $1/\lambda^Q_{l_{0,x}}$, i.e.,

$$\mathrm{E}[T^{\mathrm{LOS}}_{l_{0,x}}] = \frac{1}{\lambda^m \,\mathrm{E}[S]\big(\mathrm{E}[W] + 2|x|/\pi\big)}. \tag{3.32}$$

The distribution of the length of busy period, $T^{\mathrm{NLOS}}_{l_{0,x}}$, depends largely on the distribution of service time of each user, i.e., $|T^m_i(l_{0,x})|$, and is somewhat complex, see [58]. In CVM, the probability that the channel is not blocked by mobile users is $\mathrm{P}^{\mathrm{LOS},m}_{l_{0,x}}(t)$, thus we can compute $\mathrm{E}[T^{\mathrm{NLOS}}_{l_{0,x}}]$ without computing the exact distribution of $|T^m_i(l_{0,x})|$. For a renewal process, we have the following relationship among $\mathrm{P}^{\mathrm{LOS},m}_{l_{0,x}}(t)$, $\mathrm{E}[T^{\mathrm{LOS}}_{l_{0,x}}]$ and $\mathrm{E}[T^{\mathrm{NLOS}}_{l_{0,x}}]$,

$$\mathrm{P}^{\mathrm{LOS},m}_{l_{0,x}}(t) = \frac{\mathrm{E}[T^{\mathrm{LOS}}_{l_{0,x}}]}{\mathrm{E}[T^{\mathrm{LOS}}_{l_{0,x}}] + \mathrm{E}[T^{\mathrm{NLOS}}_{l_{0,x}}]}, \tag{3.33}$$

from which we can derive Eq. 3.27 □

The author of [59] shows that as the arrival rate of jobs goes to infinity, the busy period of $M/GI/\infty$ queue is asymptotically exponential with mean equal to expected busy period if the distribution function of service time, H, satisfies that,

$$(\log z)\int_z^\infty \{1 - H(y)\}\mathrm{d}y \to 0, \tag{3.34}$$

as $z \to \infty$. For our CVM model, we have the following result on the distribution of $T^{\mathrm{NLOS}}_{l_{0,x}}$.

Theorem 3.2.3. *In CVM, the distribution of* $T^{\mathrm{NLOS}}_{l_{0,x}}$ *approximates exponential distribution with mean* $\mathrm{E}[T^{\mathrm{NLOS}}_{l_{0,x}}]$ *as* $\lambda^Q_{l_{0,x}} \to \infty$*, i.e,* λ^m*,* $\mathrm{E}[S]$ *and/or* $|x|$ *goes to infinity.*

Proof. $S_i^m \geq s_{\min} > 0$, thus $|T_i^m(l_{0,x})|$ is upper bounded by $(|x| + d_A)/s_{\min}$, where d_A is the diameter of the smallest circle that contains A. $H(y) = 1$ for $y > (|x| + d_A)/s_{\min}$ thus Eq. 3.34 is satisfied. By Theorem 1 in [59], as $\lambda_{l_{0,x}}^Q \to \infty$,

$$\mathrm{P}\big(T_{l_{0,x}}^{\mathrm{NLOS}} \leq z\,\mathrm{E}\left[T_{l_{0,x}}^{\mathrm{NLOS}}\right]\big) \to 1 - e^{-z}, z > 0. \tag{3.35}$$

□

The key idea of Theorem 3.2.3 is that exponential distribution is a good approximation for the tail distribution of $T_{l_{0,x}}^{\mathrm{NLOS}}$ if $\lambda_{l_{0,x}}^Q$ is large. By Lemma 3.2.2, $\lambda_{l_{0,x}}^Q$ is large if user density is high, user speed is large and/or channel is long. There are potential problems with approximating the distribution of $T_{l_{0,x}}^{\mathrm{NLOS}}$ with an exponential distribution. If $\lambda_{l_{0,x}}^Q$ is small, the exponential distribution may not fit $T_{l_{0,x}}^{\mathrm{NLOS}}$ well. The probability that the channel is blocked by more than one blockage is small and the distribution of $T_{l_{0,x}}^{\mathrm{NLOS}}$ is close to the conditional distribution of $|T_i^m(l_{0,x})|$ given $|T_i^m(l_{0,x})| > 0$. If $\lambda_{l_{0,x}}^Q$ is large, the assumption that user movements are independent and users can overlap may not be accurate.

If, for tractability, we approximate the distribution of $T_{l_{0,x}}^{\mathrm{NLOS}}$ with an exponential distribution with mean $\mathrm{E}[T_{l_{0,x}}^{\mathrm{NLOS}}]$, then the blocking of the channel becomes a renewal process with $T_{l_{0,x}}^{\mathrm{LOS}}$ and $T_{l_{0,x}}^{\mathrm{NLOS}}$ having exponential distributions, which can be modeled by a two-state continuous time Markov model [16], see Fig 3.3. The rate that the channel changes from LOS to NLOS is $\lambda_{l_{0,x}}^Q$,

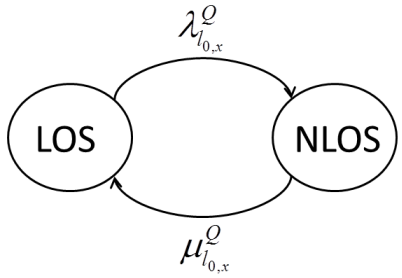

Figure 3.3: Two-state continuous time Markov model for temporal variation of link $l_{0,x}$, which is not blocked by fixed users.

while the rate channel changes from NLOS to LOS $\mu^Q_{l_{0,x}}$ is,

$$\mu^Q_{l_{0,x}} = \mathrm{E}[T^{\mathrm{NLOS}}_{l_{0,x}}]^{-1}. \tag{3.36}$$

3.3 Rate of Change for Strong LOS Neighbors Seen by a Typical Receiver

In this section we study how the aggregate rate at which blocked/weak LOS neighbors change into strong LOS neighbors as seen by a typical fixed "reference" user. In principle, when a user becomes a strong LOS neighbor, the reference user needs to make channel measurements and initiate keeping track of that user. Thus the overall rate of change is a reasonable proxy for signaling overheads and the stability of the links the reference user sees.

We define the rate of change as seen by a reference user located at 0 at time t as follows. Denote by $N_0^{\mathrm{change}}[t,\tau]$ the number of users that became strong LOS neighbors of the reference user at 0 during $[t,\tau]$, given the fixed users $\tilde{\Phi}^f$ and mobile users $\tilde{\Phi}^m$. The mean rate of change as seen by the

reference user, f^{total}, is defined by

$$f^{\text{total}} = \lim_{\tau \to t^+} \frac{\mathrm{E}_{\tilde{\Phi}^f, \tilde{\Phi}^m}\left[N_0^{\text{change}}[t,\tau]\right]}{\tau - t}. \tag{3.37}$$

Based on our CVM model, f^{total} is invariant to t and can be characterized as follows.

Theorem 3.3.1. *Under CVM model, the rate of change for strong LOS neighbors seen by a typical fixed user, f^{total}, is given by*

$$f^{\text{total}} = f^{\text{range}} + f^{\text{fixed}} + f^{\text{mobile}}, \tag{3.38}$$

where f^{range} is the rate at which mobile users enter $b(0, r_{\max})$, circle centered at 0 with radius $r_{\max}$, and have LOS channels, i.e, are not blocked, f^{fixed} is the rate of change associated with temporal channel variations to other fixed users in $b(0, r_{\max})$, and f^{mobile} is the rate of change associated temporal variations in channels to other mobile users in $b(0, r_{max})$. These three contributions are characterized as follows:

$$f^{\text{range}} = 2\lambda^m \cdot r_{\max} \cdot \mathrm{E}[S] \cdot \mathrm{P}^{\text{LOS}}_{l_{0,(0,r_{\max})}}, \tag{3.39}$$

$$f^{\text{fixed}} = \lambda^f \cdot \int_{b(0,r_{\max})} \mathrm{P}^{\text{LOS}}_{l_{0,x}} \cdot \lambda^Q_{l_{0,x}} \, dx, \tag{3.40}$$

$$f^{\text{mobile}} = \lambda^m \cdot \int_{b(0,r_{\max})} \int\int \left(\delta^{\text{LOS}}_{(x,\theta,s)} + \mathrm{P}^{\text{LOS}}_{l_{0,x}} \cdot \left(\lambda^{Q,f}_{(x,\theta,s)} + \lambda^{Q,m}_{(x,\theta,s)}\right)\right) P_m(ds, d\theta) \, dx, \tag{3.41}$$

where $P_m(S, \Theta)$ is the probability measure of S and Θ, $\delta^{\text{LOS}}_{(x,\theta,s)}$ is the rate that $\mathrm{P}^{\text{LOS}}_{l_{0,x}}$ changes due to movement, $\lambda^{Q,f}_{(x,\theta,s)}$ and $\lambda^{Q,m}_{(x,\theta,s)}$ are the expected rate over $\tilde{\Phi}^f$ and $\tilde{\Phi}$, that the channel between the reference fixed user at 0 and a mobile user

at location x with orientation θ and speed s, i.e., (x, θ, s), sees new blockages as a result of other fixed users and mobile users respectively.

$$\delta^{\text{LOS}}_{(x,\theta,s)} = -(\lambda^f + \lambda^m) \cdot s \cdot \cos(\omega) \cdot \frac{\mathrm{E}\left[\nu_1(\partial A)\right]}{\pi}, \tag{3.42}$$

$$\lambda^{Q,f}_{(x,\theta,s)} = \lambda^f \cdot s \cdot \left(\frac{|x| \cdot |\sin(\omega)|}{2} + \frac{\mathrm{E}[\nu_1(\partial A)]}{\pi} \cdot \big(1 + \cos(\omega)\big) \right), \tag{3.43}$$

$$\lambda^{Q,m}_{(x,\theta,s)} \approx \lim_{\tau \to t^+} \frac{\lambda^m \cdot \mathrm{E}_{A,V}\left[\nu_2\big(\check{A} \oplus M_{(x,v,V,\tau-t)}\big)\right]}{\tau - t}. \tag{3.44}$$

ω is the angle between v and vector from 0 to x, see Fig. 3.4a, $M_{(x_0,v_0,v,\tau-t)} = l_{0,x_0} \cup \big(-(\tau - t) \cdot v + l_{0,x_0+(\tau-t)\cdot v_0}\big)$, see Fig. 3.4b.

(a) (b)

Figure 3.4: (a) Movement of user at x with velocity v in$[t, \tau]$. ω is the angle between v and vector 0 to x. (b) Illustration of $M_{(x_0,v_0,v,\tau-t)}$.

The proof is in the appendix (Section 3.7.1). Theorem 3.3.1 can also be extended for the rate of change seen by mobile users. If self blockage is considered, the rate of change becomes $p_{\text{facing}} \cdot f^{\text{total}}$, where p_{facing} is the probability that the channel between two users is not self blocked given that users are facing random directions. Actually f^{range} is not proportional to p_{facing}, but it is small compared to f^{change}, see Section 3.5.

3.4 Impact on MAC in mmWave Networks

In this section, we analyze the impact of temporal variation caused by mobility on MAC scheduler in mmWave wearable networks. In particular, we focus on a simple clustering based MAC design as used in Chapter 2 and [2]. Fixed users form clusters with close by neighbors while mobile users work independently and do not cooperate with each other. In each cluster, a user is selected as cluster head, which synchronizes cluster members, schedules signaling transmissions and coordinates data transmissions. Such a MAC involves formation and maintenance of clusters, and we study how user mobility would impact the overhead and performance of these two procedures.

We consider two scenarios: 1) a fixed user joins a network and connects to the closest strong LOS cluster head it finds within a probing interval, and 2) a user performs re-clustering after losing the strong LOS channel to cluster head for a given period time. The distribution of users is the same as described in Section 3.1. Let us denote by M the average number of users in a cluster, and assume that each fixed user has a probability of $1/M$ to be a cluster head. As a simple model, we assume the locations of cluster heads follow an HPPP with density λ^f/M. We assume the state of channels are independent, and we use the two-state Markov model developed earlier to model the impact of dynamic blocking.

Joining Network. A randomly located fixed user joins the network at time 0. It scans the channel for some time t_{probe} and connects to the closest cluster head that it has strong LOS channel to during $[0, t_{\text{probe}}]$. We want to

study the probability that the user finds at least one cluster head in $[0, t_{\text{probe}}]$ and the distribution of the distance to the cluster head it connects to. Use the location of the fixed user as the reference point 0, and denote by $\mathrm{P}^{\text{LOS}}_{l_{0,x}}[0, t_{\text{probe}}]$ the probability that $l_{0,x}$ has ever been LOS in $[0, t_{\text{probe}}]$, then we have

$$\mathrm{P}^{\text{LOS}}_{l_{0,x}}[0, t_{\text{probe}}] = \mathrm{P}^{\text{LOS},f}_{l_{0,x}} \cdot \big(1 - (1 - \mathrm{P}^{\text{LOS},m}_{l_{0,x}}(0)) \cdot e^{-\mu^{Q}_{l_{0,x}} \cdot t_{\text{probe}}}\big), \tag{3.45}$$

where $e^{-\mu^{Q}_{l_{0,x}} \cdot t_{\text{probe}}}$ is the probability the channel is kept blocked by mobile users in $[0, t_{\text{probe}}]$. Denote by $N^{\text{CH}}_{b(0,r)}(t_{\text{probe}})$ the number of cluster heads in $b(0, r)$ with an LOS channel to the new user in $[0, t_{\text{probe}}]$. Channels are independent thus $N^{\text{CH}}_{b(0,r)}(t_{\text{probe}})$ has a Poisson distribution with mean

$$\mathrm{E}\left[N^{\text{CH}}_{b(0,r)}(t_{\text{probe}})\right] = \frac{\lambda^f}{M} \cdot \int_{b(0,r)} \mathrm{P}^{\text{LOS}}_{l_{0,x}}[0, t_{\text{probe}}] dx. \tag{3.46}$$

Denote by D_{CH} the distance to the closest cluster head that user finds in $[0, t_{\text{probe}}]$, and $G_{D_{\text{CH}}}(\cdot)$ the cumulative density function (CDF) of D_{CH}, then we have

$$G_{D_{\text{CH}}}(r) = 1 - \exp\big(-\mathrm{E}\left[N^{\text{CH}}_{b(0,r)}(t_{\text{probe}})\right]\big). \tag{3.47}$$

The probability that the new user has found a cluster head in $[0, t_{\text{probe}}]$, $\mathrm{P}_{\text{connect}}(t_{\text{probe}})$, is $G_{D_{\text{CH}}}(r_{\max})$.

Re-clustering. We assume a user performs re-clustering if its channel to the cluster head is blocked for t_{out}. Assume the reference fixed user is located at 0, with the cluster head located at x. $l_{0,x}$ is LOS at time 0. Denote by $T^{\text{recluster}}_{l_{0,x}}$ the time before the user re-clusters. In Theorem 3.2.1 we have shown that the blocking of the channel is an alternating renewal process, thus re-clustering is performed if $T^{\text{NLOS}}_{l_{0,x}} \geq t_{\text{out}}$.

Denote by $\overline{G}_{T^{\text{NLOS}}_{l_{0,x}}}(t)$ the complementary CDF of $T^{\text{NLOS}}_{l_{0,x}}$, which is approximated by that of an exponential distribution with mean $\mu^{Q}_{l_{0,x}}$. The number of LOS periods before re-clustering is $1/\overline{G}_{T^{\text{NLOS}}_{l_{0,x}}}(t_{\text{out}})$, and the number of NLOS periods, excluding the NLOS period when re-clustering is performed, is $1/\overline{G}_{T^{\text{NLOS}}_{l_{0,x}}}(t_{\text{out}}) - 1$. The time with LOS channel before re-clustering is

$$\frac{1}{\overline{G}_{T^{\text{NLOS}}_{l_{0,x}}}(t_{\text{out}})} \cdot \mathrm{E}\left[T^{\text{LOS}}_{l_{0,x}}\right],$$

and the time spent with no LOS connection to cluster head is

$$t_{\text{out}} + \left(\frac{1}{\overline{G}_{T^{\text{NLOS}}_{l_{0,x}}}(t_{\text{out}})} - 1\right) \cdot \mathrm{E}\left[T^{\text{NLOS}}_{l_{0,x}} \middle| T^{\text{NLOS}}_{l_{0,x}} < t_{\text{out}}\right].$$

3.5 Numerical Results

In this section we evaluate the accuracy of our analysis and discuss the impact of mobile blockages on MAC design using numerical results. Users are assumed to have the same cross-section A which is a rectangle of size $0.45\,\text{m} \times 0.25\,\text{m}$, with their facing directions perpendicular to the long side of the rectangle. The speed of users is $1\,\text{m}/\text{sec}$ and $r_{\max}$ is $10\,\text{m}$.

Fig. 3.5 exhibits the CDF of $T^{\text{LOS}}_{l_{0,x}}$ and $T^{\text{NLOS}}_{l_{0,x}}$ for $\lambda^m = 0.5/\text{m}^2$. For $T^{\text{LOS}}_{l_{0,x}}$ our analysis is an exact match of simulation results. For $T^{\text{NLOS}}_{l_{0,x}}$ we can see that approximation using the two-state Markov model gives a good estimate for the distribution for large t, but not accurate for small t.

Fig. 3.6 exhibits the rate of change as seen by a typical fixed user characterized in Theorem 3.3.1. In Fig. 3.6a, λ^f is the same as λ^m. In

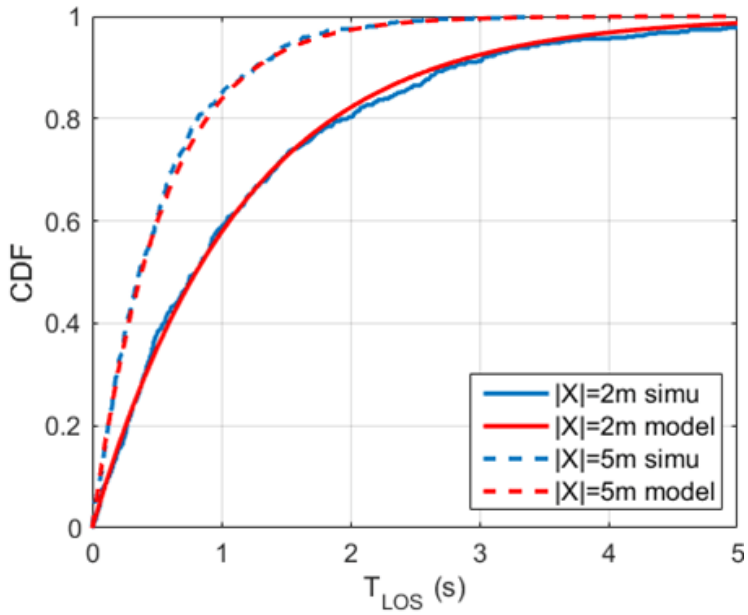

(a) CDF of $T_{l_{0,x}}^{\text{LOS}}$

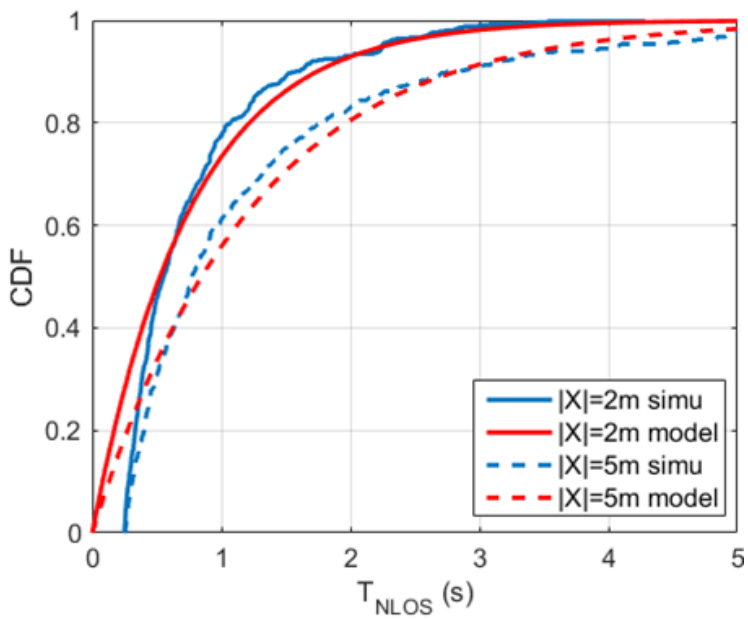

(b) CDF of $T_{l_{0,x}}^{\text{NLOS}}$

Figure 3.5: CDF of $T_{l_{0,x}}^{\text{LOS}}$ and $T_{l_{0,x}}^{\text{NLOS}}$, given $l_{0,x}$ is not blocked by fixed users.

Fig. 3.6b, $\lambda^f + \lambda^m = 1$ user per m^2 while the proportion of mobile users, $\rho^m = \lambda^m/(\lambda^m + \lambda^f)$ changes. Comparing the analysis to the simulations shows that the analysis is a good match. From Fig. 3.6a we can see that as user density increases, the rate of change first increases due to increased mobility, then saturates and even begins decreasing. The reason is that in highly dense scenarios, most neighbors are blocked thus their impact on variability of the interference environment becomes limited. Also the rate of change contributed by mobile users is higher than that from fixed users. In Fig. 3.6b the rate of change increases almost linearly with the proportion of mobile users, ρ^m. The takeaway of these results is that for dense environments, the channels may be poor due to blockage, but the overheads associated with tracking users may scale with density. However, the overheads would increase with the proportion of mobile users. The design insight here is that fixed users may track other users when the proportion of mobile users is low. When the environment is highly mobile, i.e., with high proportion of mobile users, users may choose not to coordinate with mobile users due to excessive overheads.

Fig. 3.7 exhibits results on a fixed user joining the network. As expected, $\mathrm{P}_{\mathrm{connect}}$ increases with t_{probe} while decreases with λ^m. The distribution of the distance to cluster head is pretty robust to t_{probe} and λ^m, but depends on the fixed user density λ^f and cluster size M. Such results indicate that clustering takes more time when there is more mobile blockages. The distance to cluster head, however, is not very sensitive to mobile blockages.

Fig. 3.8 exhibits how mobile blockages impact re-clustering. As can be

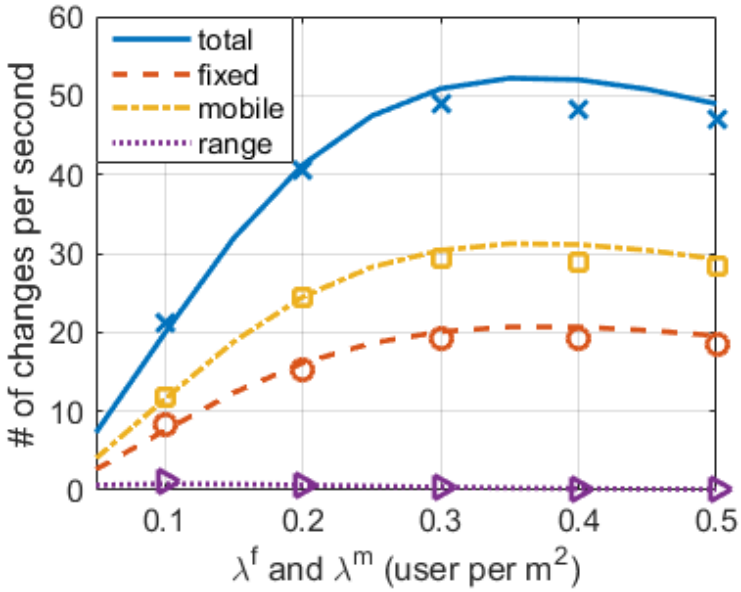

(a) Rate of change for $\lambda^f = \lambda^m$.

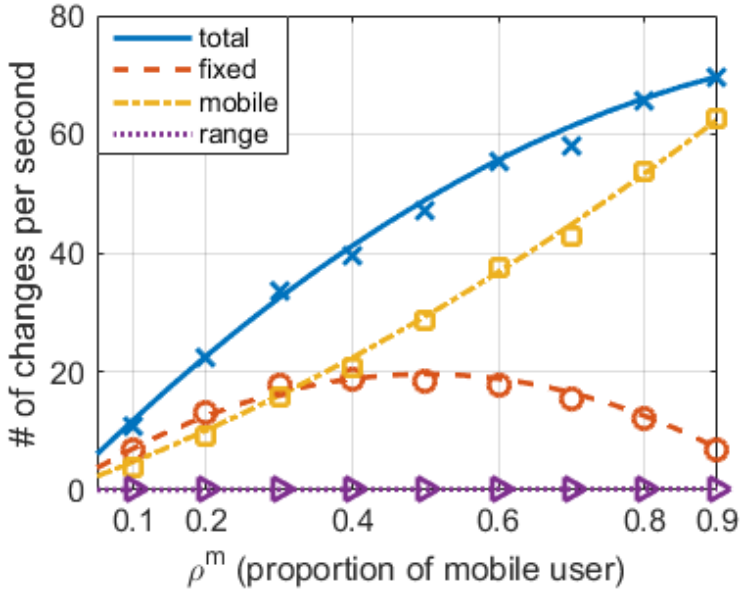

(b) Rate of change for different ρ^m.

Figure 3.6: Rate of change as seen by a typical fixed user. The markers represent results from simulations.

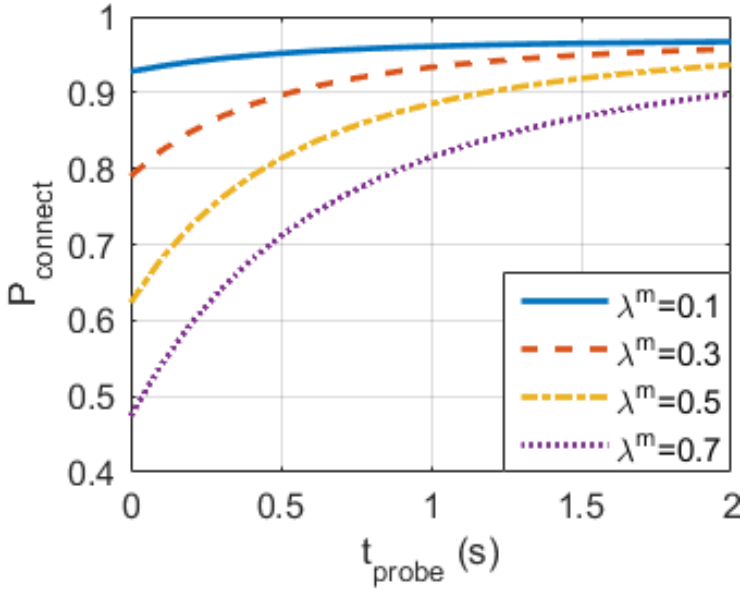

(a) Prob. finding cluster head in t_{probe}

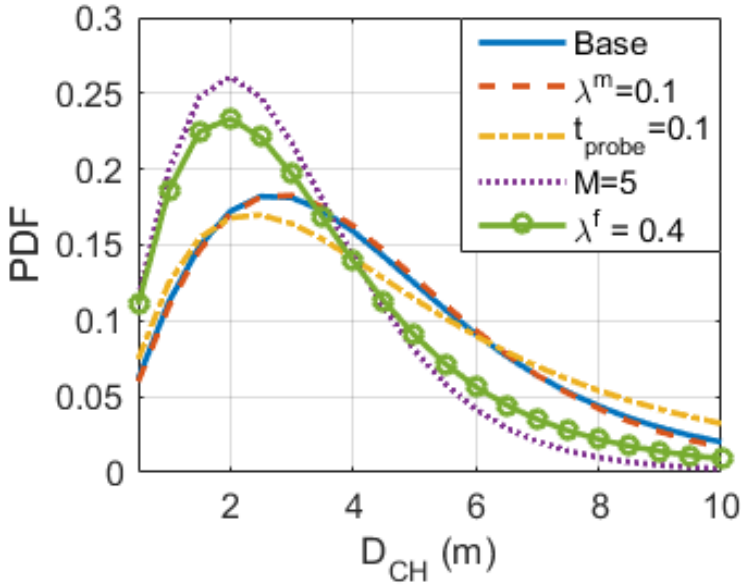

(b) PDF of distance to cluster head

Figure 3.7: (a) Probability of finding a cluster head in $[0, t_{\text{probe}}]$ and (b) the PDF of distance to the connected cluster head. In the Base case, $\lambda^f = 0.2/\text{m}^2$, $\lambda^m = 0.5/\text{m}^2$, $M = 10$, $t_{\text{probe}} = 2s$.

seen in Fig. 3.8a, the time before re-clustering grows super-linearly with t_{out}, indicating that a longer t_{out} can help reduce re-clustering overheads. However, as shown in Fig. 3.8b, the connection to the cluster head can be poor if t_{out} is large. Choosing t_{out} requires making a trade-off between reducing re-clustering and improving connection quality for signaling. When λ^m is high, the frequency of re-clustering is high and the channel quality is poor, thus users should connect to closer cluster heads, or not use a coordination based MAC.

3.6 Conclusion

In this chapter we introduce a new model and analysis tools to study mobile blockages in mmWave settings where channel dynamics (LOS/NLOS) have an impact on MAC overheads/performance. Our formal results show the temporal variations between LOS/NLOS state of a channel follow an on/off renewal process, whose holding time in each state is characterized. Based on our analysis, we derive the rate of change for channel states and estimate the associated signaling overheads resulting from user/blockage mobility. In dense and mobile networks, fixed users should perhaps track nearby fixed users, and not be too reactive to changes due to blockages, most likely associated with moving users. Meanwhile, they should avoid coordinating with distant and/or mobile users. From a MAC perspective the challenge is to differentiate among mobile and fixed neighbors so as to optimize coordination and scheduling.

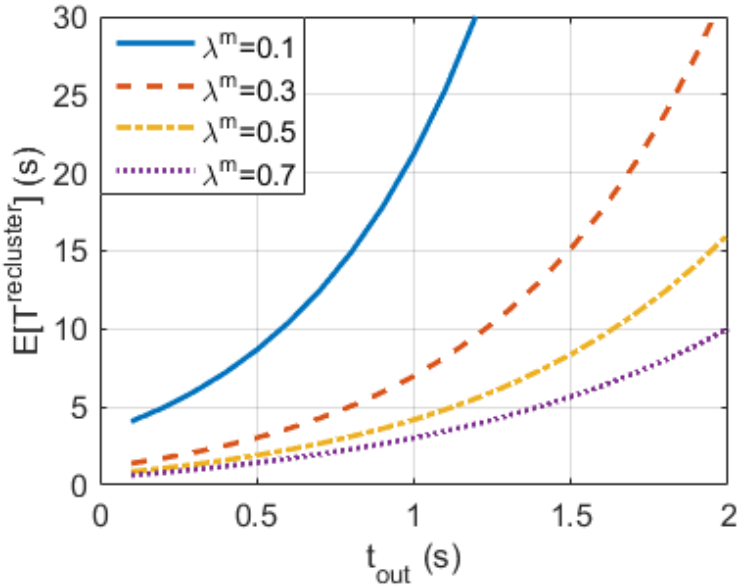

(a) Average time before re-clustering.

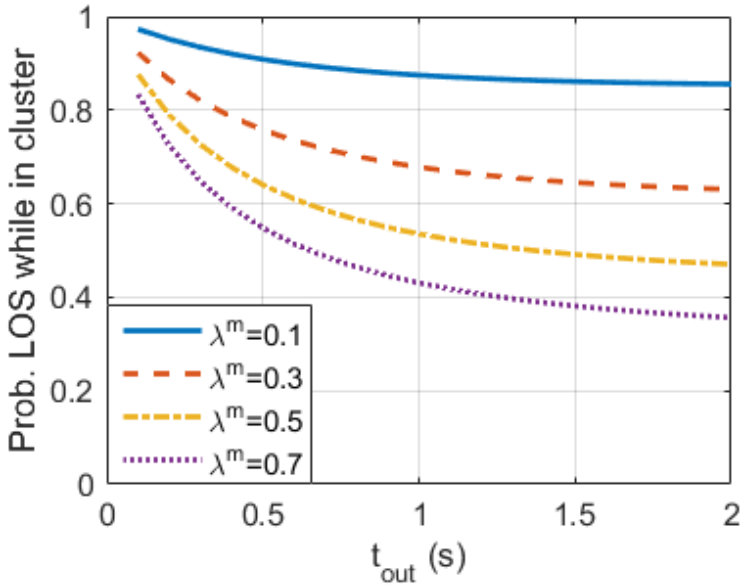

(b) Proportion of time with LOS channel before re-clustering

Figure 3.8: Impact of mobile blockages on re-clustering given $|x| = 4\,\mathrm{m}$.

3.7 Appendix

3.7.1 Proof of Theorem 3.3.1

Proof. $N_0^{\text{change}}[t,\tau]$ consists of three parts, mobile users move in $b(0,r_{\max})$ with LOS channels, the channels to fixed and mobile users in $B(0,r_{\max})$ change from NLOS to LOS.

Denote by $N^{new}_{b(0,r_{\max})}(t,\tau]$ the number of mobile users that enter $b(0,r_{\max})$ in $(t,\tau]$. $\nu_2(b(0,r_{\max})) = \pi r_{\max}^2$, $\nu_1(\partial\, b(0,r_{\max})) = 2\pi r_{\max}$. Following the same steps in Lemma 3.2.2, we have

$$N^{new}_{b(0,r_{\max})}(t,\tau] = 2\lambda^m \cdot r_{\max} \cdot \mathrm{E}[S] \cdot (\tau - t), \tag{3.48}$$

thus $f^{\text{range}} = 2\lambda^m \cdot r_{\max} \cdot \mathrm{E}[S] \cdot \mathrm{P}^{\text{LOS}}_{l_{0,(0,r_{\max})}}(t)$.

Denote by $N_0^{\text{change},f}[t,\tau]$ the number of fixed users whose channels to 0 change from NLOS to LOS in $[t,\tau]$, i.e.,

$$N_0^{\text{change},f}[t,\tau] = \sum_{(x,a,\theta)\in\tilde{\Phi}^f} g^{\text{fixed}}\big([t,\tau],(x,a,\theta),\tilde{\Phi}^f\backslash(x,a,\theta),\tilde{\Phi}^m\big), \tag{3.49}$$

where $g^{\text{fixed}}\big([t,\tau],(X,A,\Theta),\tilde{\Phi}^f\backslash(X,A,\Theta),\tilde{\Phi}^m\big)$ is an indicator function that the channel between fixed user (X,A,Θ) and 0 changes from NLOS to LOS during $[t,\tau]$, given other fixed users, $\tilde{\Phi}^f\backslash(X,A,\Theta)$, and mobile users $\tilde{\Phi}^m$. Using the Reduced Campbells formula for IMPPP in [53], we can compute $\mathrm{E}_{\tilde{\Phi}^f,\tilde{\Phi}^m}\left[N_0^{\text{change},f}[t,\tau]\right]$ as follows,

$$\mathrm{E}_{\tilde{\Phi}^f,\tilde{\Phi}^m}\left[N_0^{\text{change},f}[t,\tau]\right] = \int\limits_{b(0,r_{\max})} \lambda^f \cdot \mathrm{E}^!\big[g^{\text{fixed}}\big]\, dx, \tag{3.50}$$

where $\mathrm{E}^{!}[g^{\text{fixed}}]$ is the expectation of g^{fixed} over $\tilde{\Phi}^m$ and the reduced Palm probability of $\tilde{\Phi}$, given $X = x$.

Denote by $f^{\text{fixed}}(x)$ the expected rate that fixed user located at x changes from NLOS to LOS, i.e.,

$$f^{\text{fixed}}(x) = \lim_{\tau \to t^+} \frac{\mathrm{E}^{!}\left[g^{\text{fixed}}([t,\tau],(x,A,\Theta),\cdot,\cdot)\right]}{\tau - t}. \tag{3.51}$$

Under CVM assumptions, user's cross section and speed are bounded, thus $f^{\text{fixed}}(x)$ is bounded and we have

$$f^{\text{fixed}} = \lambda^f \cdot \int_{b(0,r_{\max})} f^{\text{fixed}}(x)\, dx. \tag{3.52}$$

Denote by $f^{\text{fixed}}_{\text{NLOS}}(x)$ the expected rate that the channel between fixed user at x and 0 changes from LOS to NLOS, then f^{fixed} and $f^{\text{fixed}}_{\text{NLOS}}$ satisfy the following equation,

$$f^{\text{fixed}} - f^{\text{fixed}}_{\text{NLOS}} = \frac{d}{dt}\mathrm{P}^{\text{LOS}}_{l_{0,x}}(t), \tag{3.53}$$

where $\frac{d}{dt}\mathrm{P}^{\text{LOS}}_{l_{0,x}}(t)$ is rate that the probability of having LOS channel changes. For fixed users, $\frac{d}{dt}\mathrm{P}^{\text{LOS}}_{l_{0,x}}(t) = 0$, thus we have $f^{\text{fixed}}(x) = f^{\text{fixed}}_{\text{NLOS}}(x)$. By Lemma 3.2.2, the mobile blockages follows Poisson arrival with rate $\lambda_{l^Q_{0,x}}$. The channel can change from LOS to NLOS only if it is LOS at time t. Combine the above two facts, $f^{\text{fixed}}(x)$ is given by

$$f^{\text{fixed}}(x) = f^{\text{fixed}}_{\text{NLOS}}(x) = \mathrm{P}^{\text{LOS}}_{l_{0,x}}(t) \cdot \lambda^Q_{l_{0,x}}. \tag{3.54}$$

For f^{mobile} we can derive Eq. 3.41 following the similar steps as those for f^{fixed}. Conditioning on that there is a mobile user (x,θ,s), the rate that

$l_{0,x}$ changes from NLOS to LOS is $f^{\text{mobile}}(x,\theta,s) = \frac{d}{dt}\mathrm{P}^{\text{LOS}}_{l_{0,x}}(t) + f^{\text{mobile}}_{\text{NLOS}}(x,\theta,s)$. By Eq. 3.24, the rate that $\mathrm{P}^{\text{LOS}}_{l_{0,x}}(t)$ changes is given by,

$$\delta^{\text{LOS}}_{(x,\theta,s)} = \frac{d}{dt}\mathrm{P}^{\text{LOS}}_{l_{0,x}}(t) = -(\lambda^f + \lambda^m)\cdot s \cdot \cos(\omega) \cdot \frac{\mathrm{E}\left[\nu_1(\partial A)\right]}{\pi}. \tag{3.55}$$

The blockages follow Poisson arrival, thus we have

$$f^{\text{fixed}}_{\text{NLOS}} = \mathrm{P}^{\text{LOS}}_{l_{0,x}}(\lambda^{Q,f}_{(x,\theta,s)} + \lambda^{Q,m}_{(x,\theta,s)}). \tag{3.56}$$

$\lambda^{Q,f}_{(x,a,\theta,s)}$ is given by,

$$\lambda^{Q,f}_{(x,\theta,s)} = \lim_{\tau\to t} \frac{\mathrm{E}\left[N^f_K[t,\tau] - N^f_{l_{0,x}}\right]}{\tau - t}, \tag{3.57}$$

where the convex set K here is the triangle consisting of 0, x and $x+(\tau-t)\cdot v$, see Fig. 3.4a. By the generalized Steiner formula and the law of cosines, we can get Eq. 3.43.

For $\lambda^{Q,m}_{(x,\theta,s)}$, we denote by $N^m_{(x,\theta,s)}[t,\tau]$ the number of mobile blockages that have intersected the channel of mobile user (x,θ,s) in $[t,\tau]$, i.e.,

$$N^m_{(x,\theta,s)}[t,\tau] = \sum_{i=1}^{\infty} \mathbb{1}\left(\exists z \in [t,\tau] \text{ s.t. } B^m_i(z) \cap l_{0,x+(z-t)v} \neq \emptyset\right), \tag{3.58}$$

where v is the velocity vector of mobile user (x,θ,s). Given that we only need to compute $N^m_{(x,\theta,s)}[t,\tau]$ for $\tau \to t^+$, we approximate the condition in Eq. 3.58 by $\mathbb{1}\left(\exists z \in \{t,\tau\} \text{ s.t. } B^m_i(z) \cap l_{0,x+(z-t)v} \neq \emptyset\right)$. Take expectation over $\tilde{\Phi}^m$ and we can get Eq. 3.44. □

Part II

Impact of Blockage and Mobility on Collaborative Sensing for Automated Driving Applications

Chapter 4

Performance and Scaling of Collaborative Sensing and Networking for Automated Driving Applications

In this chapter we present new models and performance scaling analysis for vehicular collaborative sensing and networking. We quantify the coverage and reliability gains as are their dependence on the penetration of collaborative vehicles. We further evaluate the associated communication loads in terms of the V2V and V2I capacity requirements and how these depend on penetration.

4.1 Modeling Sensing in Obstructed Environments

We begin by introducing a simple stochastic geometric model to study the character of collaborative sensing.

4.1.1 Obstructed Environments and Sensing Capabilities

The environment includes all objects, i.e., vehicles, pedestrians, buildings, etc. In some settings there may be substantial a priori knowledge regarding the environment, e.g., static elements that are part of a previously computed HD maps [60]. While the presence of such objects is already known

they still impact collaborative sensing as they can obstruct a sensor's field of view, e.g., a building may obstruct a vehicle's view when entering an intersection. For simplicity we shall not differentiate among static and dynamic objects, and focus on sensing at a snapshot in time[1].

The centers of objects are located on 2-D plane according to a Homogeneous Poisson Point Process (HPPP) Φ with intensity λ, i.e.,

$$\Phi = \{X_i | X_i \in \mathbb{R}^2,\ i = \mathbb{N}^+\} \sim \text{HPPP}(\lambda),$$

where X_i is the location of object i, and $\mathbb{N}^+$ is the set of positive integers. Each object, say i, has a shape modeled by a random closed convex set denoted $A_i \subset \mathbb{R}^2$ referenced to the origin 0 and independent of X_i. We let E_i denote the region it occupies which is given by

$$E_i = \{X_i\} \oplus A_i \triangleq \{X_i + x | x \in A_i\},$$

i.e., the object's shape A_i shifted to its location X_i, where $\oplus$ is the Minkowski sum, see Fig. 4.1a. Thus $E = \bigcup_{i=1}^{\infty} E_i$ denotes the region occupied by objects in the environment. We refer to the region not occupied by objects, $E^c = \{x | x \notin E\}$, as the *void space*. Fig. 4.1b illustrates our model for the environment.

It is unavoidable that as automated driving technologies are progressively introduced, only a fraction of vehicles will be equipped with sensors and/or participate in collaborative sensing. Thus only the subset equipped

[1]In practice collaborative sensing system will track objects over time. Thus taking the snapshot point of view can be considered "worst case" assumption.

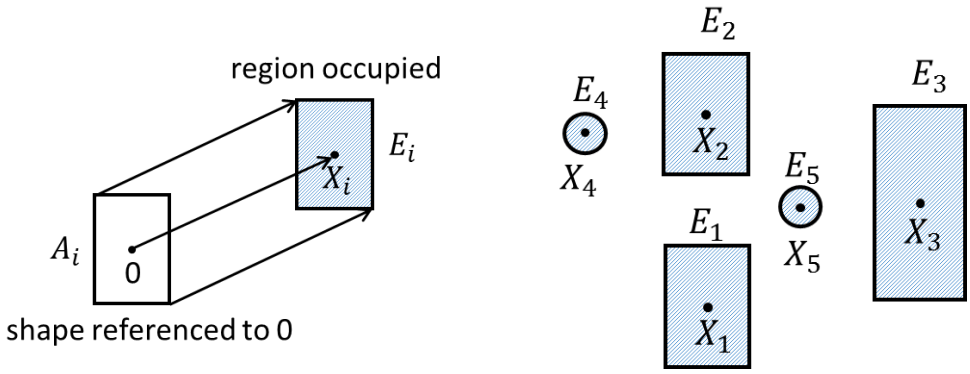

(a) Model for object i. (b) Model for environment.

Figure 4.1: Model for environment based on randomly located and shaped objects.

with sensors can participate in collaborative sensing – we shall refer to such objects as sensors. Each object has an independent probability p_s of being a sensor. Thus the locations of sensors, Φ^s, correspond to an independent thinning [57] of Φ, and $\Phi^s \sim$HPPP(λ^s) where $\lambda_s = p_s\lambda$. For such objects we assume for simplicity each has *one* sensor, and denote by $Y_i \in \mathbb{R}^2$ the relative placement of the sensor on object i referenced to X_i, so the location of sensor i is given by $X_i + Y_i \in E_i$. Each sensor i is assumed to have a radial sensing support $S_i^0 \subset \mathbb{R}^2$ referenced to the location of the sensor which is defined as follows.

Definition 4.1.1. *(Radial sensing support) The* radial sensing support *of a sensor i referenced to the origin, S_i^0, is the set of locations that can be viewed if the sensor is located at* 0 *and the LOS to the location is not obstructed. The*

set S_i^0 can be represented in polar coordinates as follows,

$$S_i^0 = \left\{(r,\theta)\middle| r \in [0, r_{\max}^i(\theta)], \theta \in [0, 2\pi]\right\}, \tag{4.1}$$

where $r_{\max}^i(\theta)$ is the maximum sensing range in direction θ.

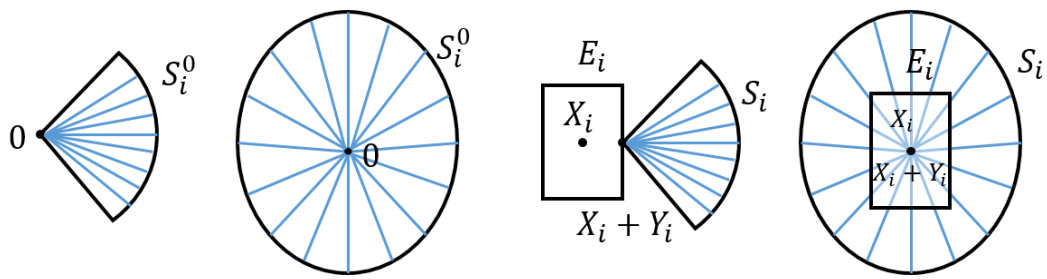

(a) Radial sensing support S_i^0 (b) Sensing support S_i

Figure 4.2: (a) Radial support referenced to the origin 0 and (b) the sensing support of sensor i.

Fig. 4.2 illustrates examples of sector and omni-directional radial sensing supports. We denote by $S_i = \{X_i + Y_i\} \oplus S_i^0$ the sensing support of sensor i. For an object, say j, which is not a sensor, we let $Y_j = 0$ and $S_j^0 = \emptyset$. The environment and the sensing field are thus modeled by an independently marked PPP (IMPPP), $\tilde{\Phi}$, which associates independent marks $M_i = (A_i, Y_i, S_i^0)$ to each object i, i.e.,

$$\tilde{\Phi} = \left\{\left(X_i, M_i\right), i \in \mathbb{N}^+\right\}.$$

Note that (A_i, Y_i, S_i^0) is independent of X_i, but A_i, Y_i, S_i^0 need not be mutually independent. Indeed if i is a sensor, $Y_i \in A_i$ since the sensor should be mounted on the object. The distribution of the shape of objects with sensors, e.g., vehicles, can be different from that of other objects, e.g., pedestrians.

4.1.2 Vehicle's Region of Interest

We shall assume each sensing vehicle is interested in information within a certain range around it – usually measured in time, e.g., t_{interest} sec. Specifically, since human drivers respond slower than automated driving systems, a larger communication range is needed for SAE Level 2 and 3 automation [61] (partial and conditional automation) than SAE Level 4 and 5 automation (high and full automation). The actual spatial range depends on the vehicle's speed s and is given by $s \cdot t_{\text{interest}}$. We model a sensing vehicle's *region of interest* as follows.

Definition 4.1.2. *(Region of interest) The* region of interest *for sensor vehicle i, D_i, is modeled as a disc, $b(X_i, r)$, centered at X_i with radius $r = s \cdot t_{\text{interest}}$.*

For a vehicle located at the center of a multi-lane road, its region of interest can be approximated by a rectangular set $[-s \cdot t_{\text{interest}}, \quad s \cdot t_{\text{interest}}] \times [-\frac{w_{\text{road}}}{2}, \frac{w_{\text{road}}}{2}]$, where w_{road} denotes the width of the road.

4.1.3 Collaborative Sensing in an Obstructed Environment

Next we define a sensor's coverage set given the environment and sensor model $\tilde{\Phi}$ as follows – see Fig. 4.3.

Definition 4.1.3. *(Sensor coverage set) For sensor i in the environment and sensor model $\tilde{\Phi}$, we let $E^{-i} = \bigcup_{j:j\neq i} E_j$ denote the environment excluding E_i. The* coverage set *of sensor i, $C_i(\tilde{\Phi})$, is given by*

$$C_i(\tilde{\Phi}) = \left\{x \in S_i \middle| x \in E_i \text{ or } l_{X_i+Y_i,x} \cap E^{-i} \subseteq \{x\}\right\}, \tag{4.2}$$

where $l_{y,z}$ *denotes the closed line segment between* $y, z \in \mathbb{R}^2$. *The* coverage area *of sensor* i *is the area of its coverage set which we denote* $|C_i(\tilde{\Phi})|$.

In the above definition, we assume that a sensor is aware of E_i, the space its associated object occupies, i.e. no "self blocking". Also $l_{X_i+Y_i,x} \cap E^{-i} \subseteq \{x\}$ verifies that the LOS channel between the sensor at X_i+Y_i and location x is not blocked by other objects. A location $x \in C_i(\tilde{\Phi})$ may be in the void space or on the surface of an object. The coverage set of sensor i represents the surrounding environment that it is able to view under environmental obstructions.

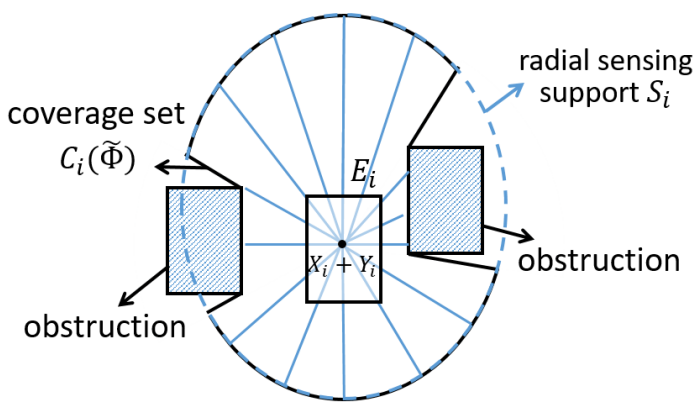

Figure 4.3: Coverage set of sensor i in $\tilde{\Phi}$.

Let C^0 denote the coverage set of a typical sensor shifted to the origin [2] and A^0, Y^0 and S^0 are the associated shape, location of sensor, and radial support set, referred to the origin. Denote by A denotes a random set with the same distribution as the shape of objects and is independent of A^0. Their distributions may be different, since the latter is conditioned on an environmental

[2]Its distribution is formally referred to as the Palm distribution [57].

object being a sensor, i.e., being a sensing vehicle. Given these notations, the expected coverage area of a *typical* sensor is given in the following theorem, and the proof is in the appendix (Section 4.6.1).

Theorem 4.1.4. *Under our environment and sensor model* $\tilde{\Phi}$ *the expected coverage area of a typical sensor is given by*

$$\mathrm{E}\big[|C^0|\big] = \mathrm{E}[|(\{Y^0\} \oplus S^0) \cap A^0|] + \mathrm{E}\bigg[\int_{(\{Y^0\}\oplus S^0)\setminus A^0} e^{-\lambda\cdot\mathrm{E}[|l_{Y^0,x}\oplus\check{A}|]}dx\bigg], \quad (4.3)$$

where $\check{A} = \{x| - x \in A\}$.

The set $(\{Y^0\} \oplus S^0) \cap A^0$ denotes the region, if any, in the sensing support overlapping with the object, while $(\{Y^0\} \oplus S^0)\setminus A^0 = \{x|x \in \{Y^0\} \oplus S^0, x \notin A^0\}$ is the region in the sensing support excluding the sensing object.

For example if objects are modeled as discs of radius r, i.e., $A = b(0, r)$, with probability 1, and sensor is mounted at the center, i.e., $Y^0 = 0$, we have that $|l_{0,x}\oplus\check{A}| = \pi r^2 + 2r\cdot|x|$ (see [57]), so $\mathrm{E}\left[|C^0|\right]$ is straightforward to compute. The theorem shows how the coverage area of a *single* sensor decreases in the object density λ since the probability of sensing a given location (the term inside integral) decreases exponentially in λ.

4.1.4 Sensor Coverage Area: Numerical and Simulation Results

Below we verify the robustness of our idealized analytical model by comparing to a simulation of vehicles on a freeway. For the analytical model, the shape of all objects (vehicles) is a disc of radius 1.67 m, roughly corresponding to the area of a vehicle, and each has an omni-directional sensing

support with radius 100 m. For the typical vehicle we limit its sensing support and coverage set to a rectangular region of interest centered on the vehicle, say i, such that

$$D_i = b(X_i, 100\,\mathrm{m}) \cap ((-\infty, \infty) \times [X_i - 12\,\mathrm{m}, X_i + 12\,\mathrm{m}]). \tag{4.4}$$

This is geared at capturing the fact that vehicles are mainly interested in sensing nearby road and sidewalks and 12 m is roughly the width of three lanes.

Our simulations are based on the freeway scenario specified in [62] with 3 lanes in each direction and lane widths of 4 m. Vehicles are placed on each lane according to a linear Matérn process [55], i.e., randomly located but ensuring a minimum gap of 10m among the centers of vehicles on the same lane. Vehicles are modeled as 4.8m $\times$1.8m rectangles, and distance from the center locations to the lane center are uniformly distributed unif$[-1, 1]$m. The coverage area does not include the region off the road. Fig. 4.4 illustrates the difference between our analytical model and the freeway simulation.

Fig. 4.5 exhibits analytical and simulation results for the vehicle's coverage area normalized by the area of sensing support scales versus vehicle density λ. Confidence intervals are not shown as they are negligible. As expected, with increased vehicle density, sensor coverage area decreases due to increased obstructions. To reduce boundary effects, the simulation results correspond to the average sensor coverage area for vehicles in the two most central lanes. As can be seen the analytical and simulation results exhibit

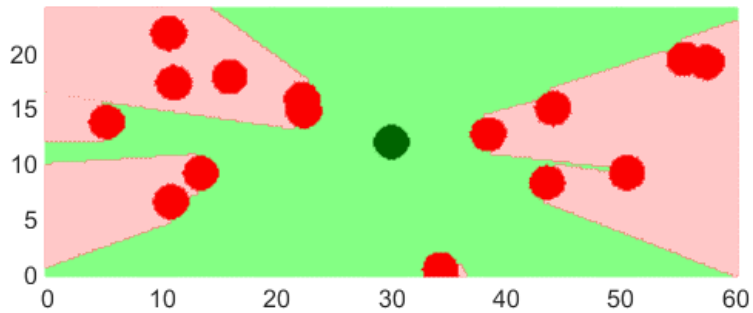

(a) Analytical model

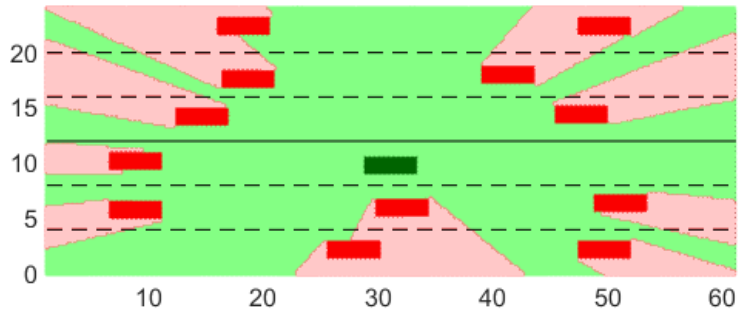

(b) Freeway simulation model

Figure 4.4: Analytical model (a) and freeway simulation model (b). In the analytical model, an object is randomly selected as the typical object, with a region of interest in Eq. 4.4. The dark green shape represents the reference object (sensor), the red shapes are other objects (obstructions). The light green region is covered by the reference sensor, while the light red region is obstructed void space. In the freeway simulation, we select a vehicle in the two central lanes as the reference vehicle to reduce boundary effect.

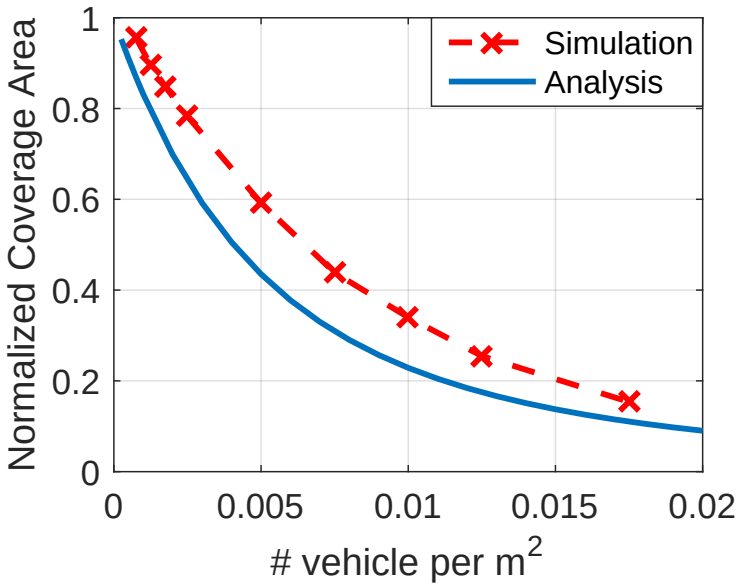

Figure 4.5: Coverage area of a typical vehicle normalized by the area of its sensing support.

similar trends. At high vehicle densities, the coverage area of a single vehicle is heavily limited, i.e., covering less than 20% of the sensing support. In an obstructed environment collaborative sensing will be critical to achieve better coverage and reliability for each vehicle's region of interest. We consider this next.

4.2 Performance Benefits of Collaborative Sensing

The benefits of collaborative sensing are twofold: (1) it increases sensing redundancy/diversity leading to improved reliability, and (2) it improves coverage and extends sensing range. We consider two metrics for the performance of collaborative sensing, i.e., *redundancy* and *coverage*.

4.2.1 Sensing Redundancy

We define sensing redundancy as the number of collaborative sensing vehicles that can view a location/object. Tracking objects based on multiple sensors' point of view provides greater reliability and robustness to sensor/communication link failures.

Definition 4.2.1. *(Sensing redundancy for a location) Given an environment and sensing field, $\tilde{\Phi}$, and a subset of sensors $K \subseteq \Phi^s$ collaborating, the* sensing redundancy for a location x *is the number of sensors in K that view x, denoted by*

$$R(\tilde{\Phi}, K, x) = \sum_{i:X_i \in K} \mathbb{1}\left(x \in C_i(\tilde{\Phi})\right). \tag{4.5}$$

In the most optimistic case $K = \Phi^s$, i.e., all sensors collaborate. The expected redundancy of a location in the void space is then given by the following theorem. The proof is in the appendix (Section 4.6.2).

Theorem 4.2.2. *Given an environment and sensing field $\tilde{\Phi}$ and all sensors collaborate, $K = \Phi^s$, the expected redundancy given a typical location x in the void space is*

$$\mathrm{E}[R(\tilde{\Phi}, \Phi^s, x) | x \notin E] = \frac{p_s \cdot \lambda \cdot \mathrm{E}[|C^0 \backslash A^0|]}{e^{-\lambda \cdot \mathrm{E}[|A|]}}, \tag{4.6}$$

where $\mathrm{E}[|C^0 \backslash A^0|]$ is given in Eq. 4.3.

Fig. 4.6 exhibits the expected sensing redundancy of a typical location in the void space. As can be gleaned from our analytical results, sensing redundancy for a location is proportional to p_s so we only exhibit results for

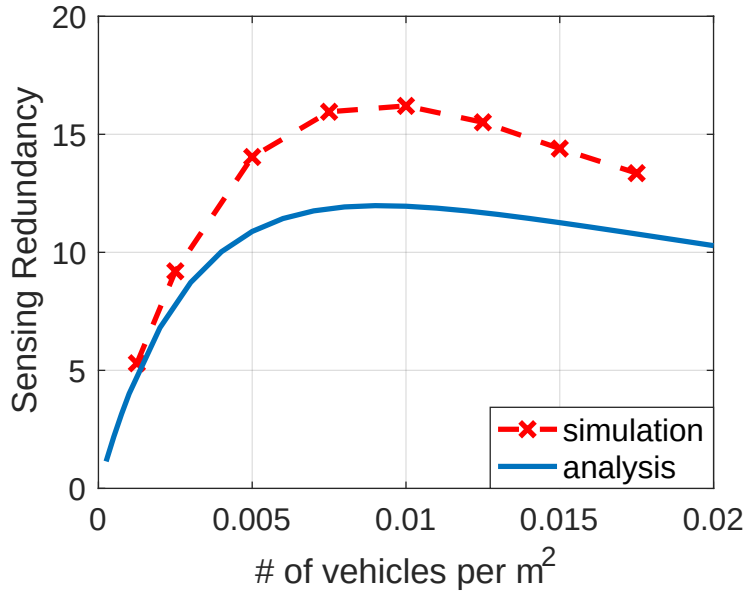

Figure 4.6: The expected sensing redundancy of a random void location versus object density. All vehicles participate in collaborating, i.e., $K = \Phi^s = \Phi$.

$p_s = 1$. At small densities sensors are not likely to be blocked thus redundancy first increases in the density of objects λ. However, at higher densities, the objects obstruct each other reducing the coverage area of each sensor and the resulting sensing redundancy. The simulation results show the expected redundancy of a random location in the central two lanes, and exhibit similar trends as the analysis. Overall one can conclude that collaborative sensing will provide highest redundancy at moderate densities, i.e., this is where in principle collaborative sensing is most reliable and robust to sensor/communication failures.

4.2.2 Collaborative Sensing Coverage and Reliability.

A location in a vehicle's region of interest of is covered by collaborative sensing if the location can be reliably sensed, i.e., sensed by a sufficient number of collaborating sensors. We define the collaborative sensing coverage and reliability for a vehicle as follows.

Definition 4.2.3. *(Collaborative sensing coverage and reliability) Given an environment and sensing field $\tilde{\Phi}$, a minimum redundancy requirement $\gamma \in \mathbb{N}^+$ for reliable sensing of a location, a subset of collaborating sensors, $K \subseteq \Phi^s$, and sensor i's region of interest D_i, the* γ-coverage set *of sensor i is the region within its region of interest, which is covered by at least γ sensors in K, denoted by*

$$C_c(\tilde{\Phi}, K, D_i, \gamma) \triangleq \big\{x \big| x \in D_i, R(\tilde{\Phi}, K, x) \geq \gamma\big\}. \tag{4.7}$$

The γ-coverage *of sensor i is the area of the γ-coverage set,*

$$|C_c(\tilde{\Phi}, K, D_i, \gamma)|. \tag{4.8}$$

The γ-coverage reliability *is the γ-coverage normalized by the area of region of interest,*

$$\frac{|C_c(\tilde{\Phi}, K, D_i, \gamma)|}{|D_i|}. \tag{4.9}$$

The γ-coverage reliability can be interpreted as the fraction of i's region of interest that can be reliably sensed. Denote by D^0 the possibly random[3]

[3]Recall the region may depend on the vehicle's speed.

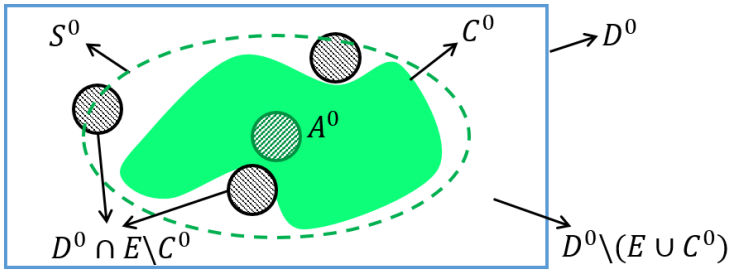

Figure 4.7: Decomposition of D^0 for collaborative sensing coverage approximation.

region of interest associated with a typical sensing vehicle, and $A^s \subset \mathbb{R}^2$ a random set having the same distribution of the shape within a the region occupied by the sensor and is covered in the sensor's sensor support, i.e., $\{Y^0\} \oplus S^0 \cap A^0$.

Approximation of γ-coverage. Denote by $\overline{Q}(k,m) = \mathrm{P}(N(m) \geq k)$, where $N(m)$ is a Poisson random variable with mean m. Denote by $\overline{R}_{\text{void}} = \mathrm{E}[R(\tilde{\Phi}, \Phi^s, x) | x \notin E]$ the expected redundancy of a location in the void space as given in Eq. 4.6. The γ-coverage can be approximated by

$$\begin{aligned}
&\mathrm{E}\left[|C_c(\tilde{\Phi},\Phi^s, D^0, \gamma)|\right] \approx \\
&\qquad \mathrm{E}[|D^0 \cap C^0 \cap A^0|] \cdot \overline{Q}(\gamma - 1, \lambda^s \cdot \mathrm{E}[|A^s|]) \\
&\qquad + \mathrm{E}[|D^0 \cap C^0 \backslash A^0|] \cdot \overline{Q}(\gamma - 1, \overline{R}_{\text{void}}) \\
&\qquad + \mathrm{E}[|D^0 \backslash A^0|] \cdot \overline{Q}(\gamma, \lambda^s \cdot \mathrm{E}[|A^s|]) \\
&\qquad + (\mathrm{E}[|D^0 \backslash A^0|] \cdot e^{-\lambda \cdot \mathrm{E}[|A|]} - \mathrm{E}[|D^0 \cap C^0 \backslash A^0|]) \cdot \overline{Q}(\gamma, \overline{R}_{\text{void}}). \qquad (4.10)
\end{aligned}$$

This approximation is based on decomposing D^0 into various sets, see Fig. 4.7 for example: $D^0 \cap C^0 \cap A^0$ the set occupied and sensed by the object,

$D^0 \cap C^0 \cap A^0$ the set outside the object but sensed by the object, $D^0 \cap E \backslash C^0$ the set occupied by objects but not in C^0, and $D^0 \backslash (E \cup C^0)$ the void space excluding C^0.

By Slivynak-Mecke theorem, the other objects as seen by the reference sensor follow an IMPPP with the same distribution as $\tilde{\Phi}$, the locations of other sensors follow HPPP(λ^s). The region covered by objects and sensors each form a Boolean process [57]. For a random location x, the number of sensors occupying and sensing x has a Poisson distribution with mean $\lambda^s \cdot \mathrm{E}[|A^s|]$, the number of objects occupying x has a Poisson distribution with mean $\lambda \cdot \mathrm{E}[|A|]$. For a location in the void spacer, we approximate the distribution of the redundancy with a Poisson distribution with mean $\overline{R}_{\text{void}}$. $\overline{R}_{\text{void}}$ is not conditioned on there being at typical sensor, thus $\overline{R}_{\text{void}}$ can be different from the expected redundancy of $x \in D^0 \backslash E$. In C^0 the reference object provides 1 redundancy and other sensors should provide $(\gamma - 1)$ redundancy, while in $D^0 \backslash C^0$ the other sensors should provide γ redundancy.

Based on the above approximation, the components of Eq. 4.10 are interpreted as follows: $\mathrm{E}[|D^0 \cap C^0 \cap A^0|] \cdot \overline{Q}(\gamma - 1, \lambda^s \cdot \mathrm{E}[|A^s|])$ is the area in A^0 that is occupied (and sensed) by $\gamma - 1$ other sensors. $\mathrm{E}[|D^0 \cap C^0 \backslash A^0|] \cdot \overline{Q}(\gamma - 1, \overline{R}_{\text{void}})$ is the area void space space in C^0 that is covered by $\gamma - 1$ other sensors. $\mathrm{E}[|D^0 \backslash A^0|] \cdot \overline{Q}(\gamma, \lambda^s \cdot \mathrm{E}[|A^s|])$ is the area in $D^0 \backslash A^0$ that is occupied (and sensed) by γ sensors. $\mathrm{E}[|D^0 \backslash A^0|] \cdot e^{-\lambda \cdot \mathrm{E}[|A|]} - \mathrm{E}[|D^0 \cap C^0 \backslash A^0|]$ is the area of void space in $D^0 \backslash A^0$ excluding C^0, and $\overline{Q}(\gamma, \overline{R}_{\text{void}})$ is the probability that a location is covered by γ other sensors.

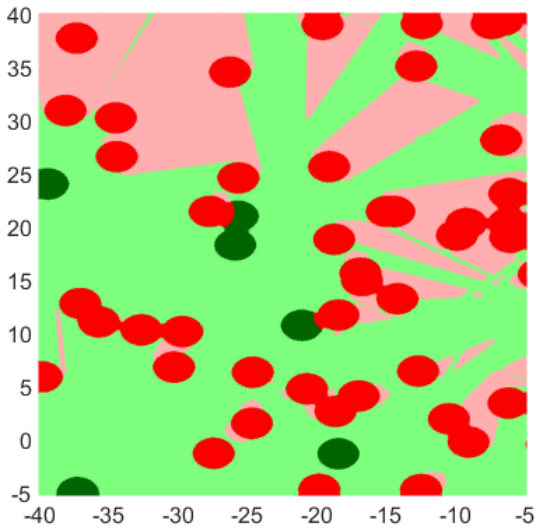

(a) Sensing in analytical model

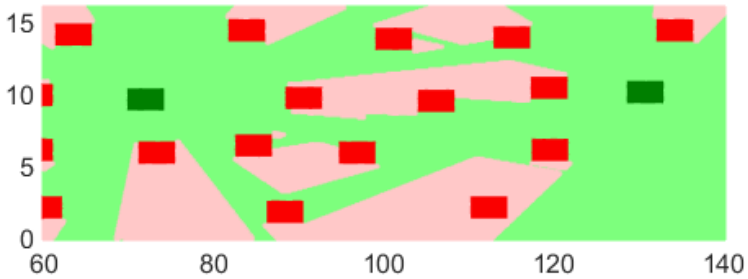

(b) Sensing in freeway scenario

Figure 4.8: Collaborative sensing in (a) analytical model, and (b) freeway simulation. Dark green shapes represent sensors, red shapes are non-sensing objects. Light green region can be sensed via collaborative sensing, while light red region are obstructed and not sensed.

Fig. 4.8 illustrates collaborative sensing in the analytical model and the freeway simulation. In the analytical model, objects are modeled as randomly distributed discs and may overlap. The objects are randomly placed thus the region covered by collaborative sensing will also be random in shape. In the freeway simulation, vehicles are randomly distributed along lanes, such that there is no overlap. The environment is more 'organized', and thus so is the collaborative sensing coverage set, e.g., the space between lanes is less likely to be obstructed.

We validate the accuracy of our generalized approximation in Fig. 4.9a, in which we consider a 2D infinite plane, $\lambda = 0.01/\text{m}^2$. The approximation is a good match of the analytical model, validating the accuracy of our approximation in Eq. 4.10. Fig. 4.9b exhibits the freeway simulation results, which show the same qualitative trend as the analytical results. As expected the minimum penetration to achieve a certain level of γ-coverage reliability increases in the required diversity γ.

Fig. 4.10 exhibits the expected 1-coverage reliability for varying penetrations p_s and vehicle densities λ. The freeway simulation results show the same trend as analytical results. Note that Eq. 4.10 is an approximation of the analytical model, which is different from our simulation of the freeway scenario. As expected, reliability increases monotonically in p_s. More importantly, collaborative sensing can greatly improve reliability even with a small penetration of collaborating vehicles, e.g., over 0.8 reliability when 20% of vehicles collaborate as compared to 0.2 reliability without collaboration at a

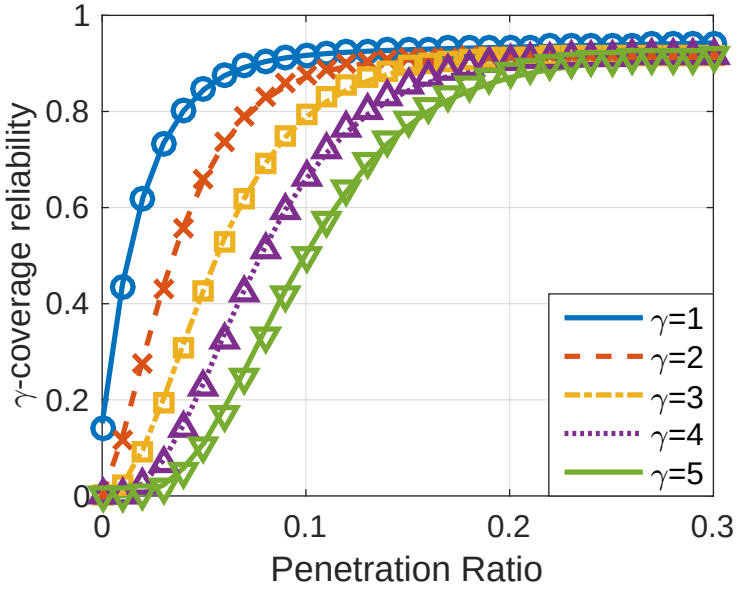

(a) Approximation validation

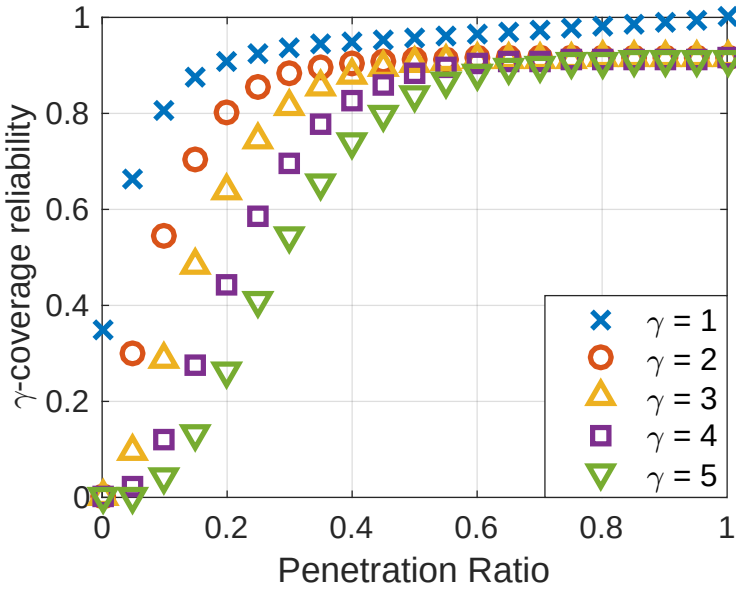

(b) Freeway simulation

Figure 4.9: γ-coverage reliability for different redundancy requirements γ. In (a) curves represent results from our approximation in Eq. 4.10, markers are simulation of the analytical model. (b) are freeway simulation results.

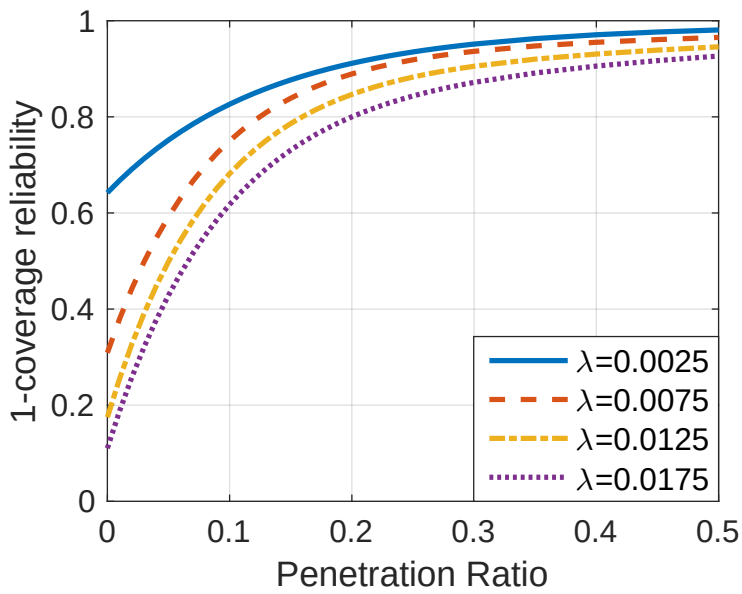

(a) Analysis

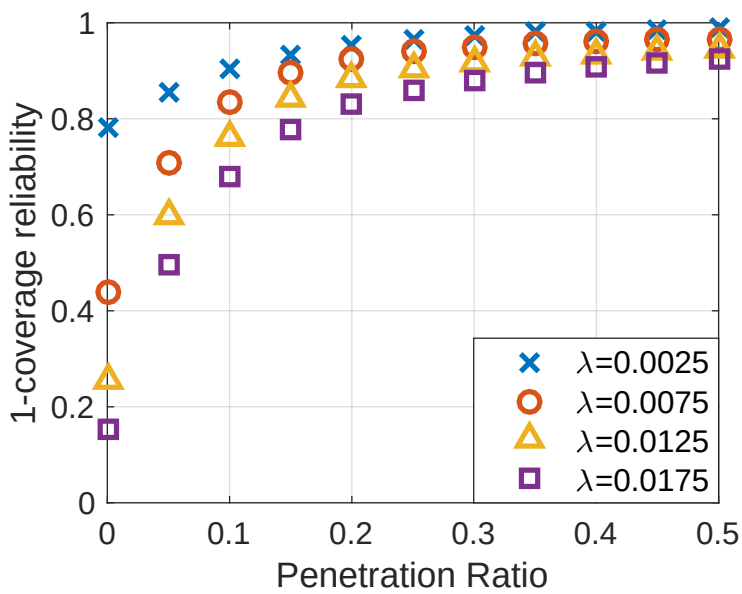

(b) Simulation

Figure 4.10: 1-coverage reliability: (a) based on analytical approximation in Eq. 4.10, and (b) obtained by simulation of freeway scenario.

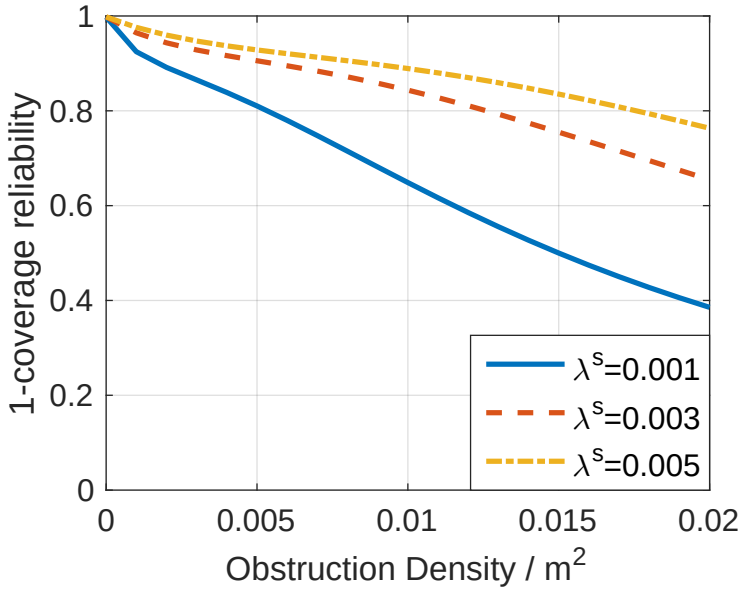

Figure 4.11: How 1-coverage reliability scales in obstruction densities, $\lambda - \lambda^s$, while sensor density λ^s is fixed.

vehicle density $\lambda = 0.0175/\text{m}^2$. Such results indicate that it can be beneficial to share sensor data even with only a subset of neighboring vehicles.

Impact of obstruction density. Another scenario we study with our analytical framework is how the collaborative sensing reliability scales in the obstruction densities when sensor density is fixed. One example of such a scenario is at some freeway junctions where vehicles entering the freeway are mainly non-sensing vehicles. Fig. 4.11 exhibits how 1-coverage reliability scales in the obstruction density based on our approximation in Eq. 4.10. The 1-coverage decreases approximately linearly with obstruction density. In Collaborative sensing with RSUs may be required to guarantee coverage in such scenarios.

4.2.3 Benefits of Collaboration with Sensing RSUs.

Despite the performance gains associated with vehicular collaborative sensing, achieving a high γ-coverage reliability at low penetrations will be difficult, especially for $\gamma > 1$. Joint collaborative sensing with RSUs having sensing capabilities can help improve coverage and reliability, e.g., RSU infrastructure could provide 100% 1-coverage reliability if located on top of the freeway (no obstruction) and their sensing support covering the freeway. If γ_{rsu} denotes the redundancy provided by RSU, the *gain* in γ-coverage associated with joint vehicle/RSU collaboration is given by

$$\mathrm{E}\left[\left|C_c(\tilde{\Phi}, \Phi^s, D^0, \gamma - \gamma_{\text{rsu}})\right|\right] - \mathrm{E}\left[\left|C_c(\tilde{\Phi}, \Phi^s, D^0, \gamma)\right|\right]. \tag{4.11}$$

In Fig. 4.9b, for $\gamma_{\text{rsu}} = 1$ and $p_s = 0.1$, collaboration with RSUs improves 2-coverage reliability by over 0.25. In summary deploying collaborative sensing RSUs will be beneficial especially at low penetrations, but possibly also at higher penetrations if $\gamma = 2$ or higher diversity is desired.

4.3 Data Volumes to Support Collaborative Sensing

In this section we model and study how vehicles sensor data rates vehicles would scale with the density of objects in the environment for different data models/representations.

4.3.1 Representations and Compression of Sensor Data.

Abstracted object model. The most compact representation of sensor data would likely be associated with sharing models for sensed objects, e.g., bounding boxes, along with additional information, e.g., type of object and/or direction and velocity of motion. The volume of data would thus be proportional to the number of objects sensed by the vehicle. We define *sensed data complexity* of sensor i, $N_i(\tilde{\Phi})$, as the number of objects that vehicle i can view, i.e.,

$$N_i(\tilde{\Phi}) = \big|\{j | j \in \mathbb{N}^+, j \neq i, E_j \cap C_i(\tilde{\Phi}) \neq \emptyset\}\big|. \tag{4.12}$$

$N_i(\tilde{\Phi})$ is a complex function of $\tilde{\Phi}$ whence we propose an upper bound, $N_i^{\text{upper}}(\tilde{\Phi})$, and an approximation (also lower bound), $N_i^{\text{approx}}(\tilde{\Phi})$. In particular

$$N_i^{\text{upper}} = \big|\{j | j \in \mathbb{N}^+, j \neq i, E_j \cap S_i \neq \emptyset\}\big|$$

denotes number of objects overlapping with vehicle i's sensing support, i.e., the maximum number of objects vehicle i can sense ignoring obstructions, and

$$N_i^{\text{approx}} = |\{j | j \neq i, X_j \in S_i \text{ and } l_{X_i,X_j} \cap E_k = \emptyset \ \forall k \neq j, i\}|$$

is the number of objects for which sensor i has an unobstructed view of their *centers* and thus a subset of the sensed objects. The expected sensing complexity of a typical sensor is then given in the following theorem, whose proof is relegated to the appendix.

Theorem 4.3.1. *Based on our system model, bounds on expected sensing complexity are given by:*

$$\mathrm{E}[N^{\text{upper},0}] = \lambda\, \mathrm{E}\left[\left|S^0 \oplus \check{A}\right|\right], \tag{4.13}$$

$$\mathrm{E}[N^{\mathrm{approx},0}] = \lambda \mathrm{E}\left[\int_{x \in S^0} e^{-\lambda\, \mathrm{E}[|l_{0,x} \oplus \check{A}|]} dx\right]. \tag{4.14}$$

where $N^{\mathrm{upper},0}$ and $N^{\mathrm{approx},0}$ denote random variables whose distribution are those as seen by a typical sensor.

2D occupancy grid map. A representation which leverages a lower level of abstraction is the 2D occupancy grid map [63], in which the environment is divided into small cells and each cell is associated a probability its being occupied by an object. If vehicles sensed data in the form of grid map , the data volume is approximately proportional to the sensors coverage area. In 2.5D maps and 3D grid maps, e.g., elevation maps, each cell has more information, e.g., height of the cell, while the data volume is still proportional to coverage area. Note that the scaling of coverage area in the density of objects was studied in Section 4.2.

Raw LIDAR sensor data. If raw LIDAR sensor data is shared, the volume of data may not be directly related to the characteristics of the environment. However, sharing all raw sensor data without any processing may not be always necessary, indeed a vehicle may compress such information based on the characteristics of the environment. For example one can consider compressing data based on the distance to sensed objects, while still preserving the valuable information. We consider two ways of compressing raw sensor data:

1. omit sensor data in the directions where no object is sensed within a predefined range;

2. subsample sensor data based on distance to sensed objects.

The sensing range of sensors is limited thus in some directions vehicles may sense no objects. Furthermore vehicles may have high resolution map of the fixed environment and raw data associated with the fixed environment can be omitted. For raw sensor data associated with surrounding objects, the resolution of data can be changed based on the distance to objects: close by objects might result a relatively large number of measurements, e.g., LIDAR data points, while distant objects have much fewer.

Let $f_i(r, \theta) \in [0, 1]$ denote the compression factor, measuring the ratio between compressed data and uncompressed data in direction θ, given the distance to measured object is r. We posit $f_i(r, \theta)$ as a non-decreasing function of r, $f_i(r, \theta) = 0$ for $r > r^i_{\max}(\theta)$. Given the environment $\tilde{\Phi}$, the length of measurements of sensor i in direction Θ is given by

$$r_i(\tilde{\Phi}, \Theta) = \max \Big\{ r \Big| r \in [0, \infty) \text{ and } \big((X_i + Y_i) \oplus l_{0,(r\cos\Theta, r\sin\Theta)} \big) \cap E^{-i} \subseteq \big\{ (r\cos\Theta, r\sin\Theta) \big\} \Big\} \quad (4.15)$$

The normalized volume of compressed raw data under our model is thus given by $\mathrm{E}_\Theta \big[f_i(r_i(\tilde{\Phi}, \Theta), \Theta) \big]$.

4.3.2 Scaling Behavior of Sensor Data Volumes

Fig. 4.12 exhibits how the sensor data volume would scale with the environment's object density. Fig. 4.12a exhibits results for sensed data complexity. As mentioned earlier upper bound does not consider blockage, and

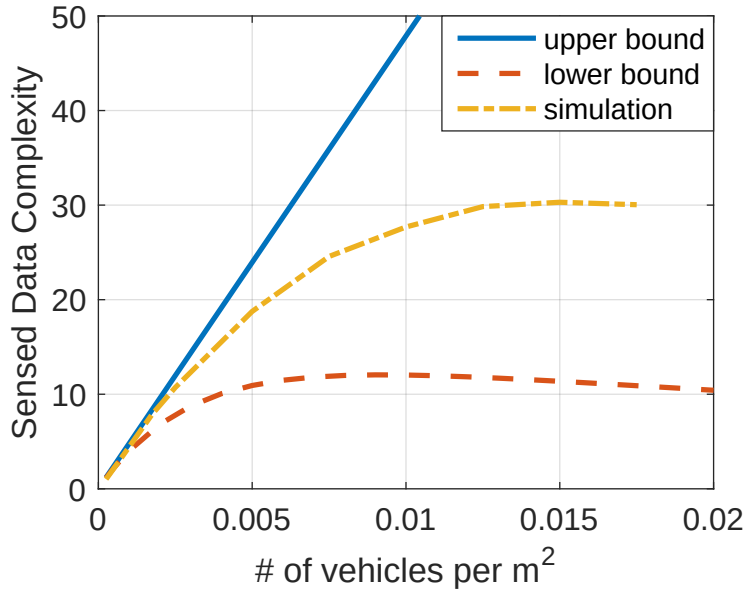

(a) Sensed data complexity

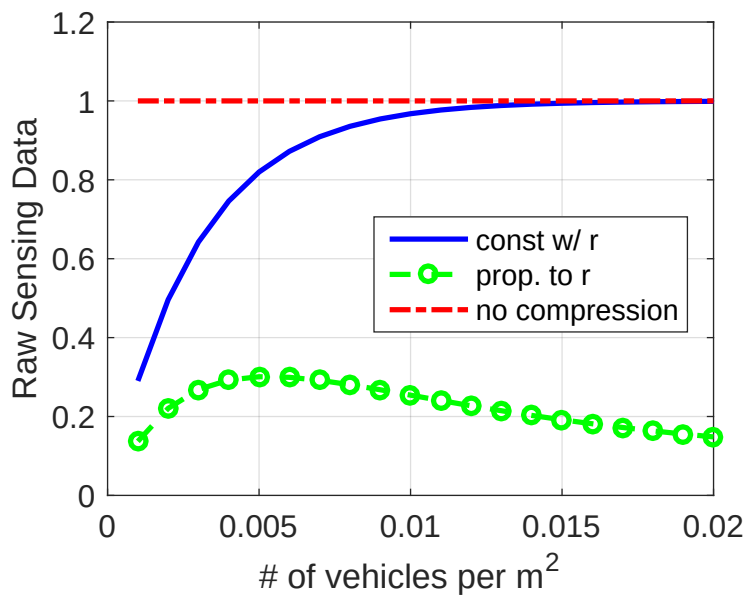

(b) Compressed LIDAR Data Volume

Figure 4.12: (a) How sensed data complexity scales with object density. (b) How LIDAR sensor data volume normalized by uncompressed LIDAR data volume scale with λ using different compression methods: omitting data with no objects (blue); omit data with no objects and $f_i(r, \theta) = r/r^i_{\max}(\theta)$ (green); no compression (red).

thus increases linearly with density. The true sensed data complexity (and approximation/lower bound) first increase in but then due to obstructions saturate and even starts decreasing in the object density. Fig. 4.12b exhibits the LIDAR data volume normalized by uncompressed LIDAR data volume under different compression methods. Omitting LIDAR sensor data in directions with no objects can effectively compress data at low density, but the save in data volume is limited at high densities as vehicles are surrounded by neighbor vehicles/objects. If sensors further compress sensor data based on distance to objects, e.g., $f_i(r, \theta) = r/r^i_{\max}(\theta)$ (measurement resolution is uniform for objects at different distances), the volume of sensor data can be reduced even at high vehicle densities.

Our results show that sensor data volume generated by one vehicle does not necessarily increase with object density due to obstructions and/or the use of compression on higher resolution data for close by objects.

4.4 Network Capacity Scaling for Collaborative Sensing

In this section we study the network capacity requirements for collaborative sensing. We first consider a setting with full penetration, i.e., *all* vehicles have sensing and V2V communication capabilities. We then turn to a setting with partial penetration, i.e., a fraction of the vehicles are not collaborating and in fact may obstruct (e.g., mmWave) communications amongst collaborating vehicles. In this setting we assume V2I links are used to overcome V2V blockages and study how V2I capacity requirements scale in the penetration

of collaboration. Our analysis provides a comprehensive view on a possible evolution of future network capacity requirements.

4.4.1 Capacity Scaling in V2V Network

When all vehicles are participating in collaborative sensing and networking one can leverage V2V links and hop-by-hop relaying to realize data sharing. Additionally since V2V links have typically short range, they can deliver high per-link rate and transmit parallelism. Still collaborative applications require many-to-many data sharing and thus capacity requirements can be quite high.

Broadcast versus unicast. In assessing capacity scaling for collaborative sensing we will differentiate V2V technologies supporting broadcast versus unicast. If broadcasting is available, a vehicle can ideally transmit data to all vehicles within its communication range. Vehicles receiving the data can then re-broadcast the data to more distant vehicles. A broadcasting mode is particularly attractive since it enables vehicles to share data with several neighboring vehicles with a single transmission. However in some settings, implementing a broadcast mode may be challenging, e.g., hard to broadcast narrow beams to each user to compensate for high penetration losses in the mmWave band. In a unicast mode a vehicle communicates with one vehicle at a time. The number of concurrent transmissions can be higher since unicast transmissions can be more directional and achieve higher rates, but more transmissions will be required.

High resolution data versus merged data. If vehicles share high resolution unprocessed sensing data, i.e., relaying is performed without processing, so per hop delays are substantially reduced. Alternatively vehicles can combine the received sensor data from neighbors with their own, send one merged data flow. This can substantially reduce the overall data rates exchanged by vehicles but requires standardization of sensing models and introduces merging delay. Given the time critical nature of vehicular collaborative sensing and need for reliability and robustness to failures/attacks, some consider relaying data without processing the preferred sharing option.

V2V capacity analysis. We shall evaluate the capacity scaling requirements for four different combinations: HD data broadcast (HB), HD data unicast (HU), merged data broadcast (MB), and merged data unicast (MU). To that end we introduce the following simple model. We consider vehicles on a road with l lanes, all vehicles have sensing and V2V communication capabilities and each has a region of interest of t_{interest} sec in both forward and backward directions. We shall consider the worst case scenario, i.e., the density of vehicles is high and the gap between (the centers of) vehicles in the same lane is the minimum gap for safe driving, t_{gap} sec. Thus if the velocity of vehicles is s m/sec, the range of interest is $s \cdot t_{\text{interest}}$ m and inter-vehicle gap is at least $s \cdot t_{\text{gap}}$ m. We denote by $\lambda_{\text{vehicle}} = \frac{1}{s \cdot t_{\text{gap}}}$ the density of vehicles on the lane. We assume vehicles need to receive data from all vehicles in their range of interest, and by symmetry vehicle also need to send data to all vehicles in their range of interest. We suppose vehicles use omni-directional antennas

but note that our results can be easily extended to the case with directional antennas as in [44]. We adopt the protocol model introduced in [64]. Each vehicle has a communication range r_{comm} and a transmission is successful if there is no other transmitter within the protection region of the receiver, i.e., a circle centered at the receiver with radius $(1+\Delta)r_{\text{comm}}$. Denote by ω the peak rate for V2V links, ν the sensor data rate per vehicle. Lower bounds on ω are given in the following result proven in the appendix (Section 4.6.3).

Theorem 4.4.1. *Under the protocol model for interference and assuming a communication range no more than the radius of region of interest, i.e.,* $r_{\text{comm}} \leq s \cdot t_{\text{interest}}$*, the lower bounds on* ω *for the four schemes are given as follows,*

$$\omega_{HB} \geq \nu \cdot 2l \cdot (1+\Delta) \cdot (2s \cdot t_{\text{interest}} - r_{\text{comm}}) \cdot \lambda_{\text{vehicle}}, \tag{4.16}$$

$$\omega_{HU} \geq \nu \cdot 4l^2 \cdot (1+\Delta) \cdot s \cdot t_{\text{interest}} \cdot r_{\text{comm}} \cdot \lambda^2_{\text{vehicle}}, \tag{4.17}$$

$$\omega_{MB} \geq \nu \cdot 2l \cdot (1+\Delta) \cdot r_{\text{comm}} \cdot \lambda_{\text{vehicle}}, \tag{4.18}$$

$$\omega_{MU} \geq \nu \cdot 4l^2 \cdot (1+\Delta) \cdot r^2_{\text{comm}} \cdot \lambda^2_{\text{vehicle}}. \tag{4.19}$$

V2V capacity scaling analysis. From the above results we see that the V2V link capacity requirements increase with communication range (except for ω_{HB}). Reducing r_{comm} can decrease the required V2V link capacity by increasing the number of concurrent transmissions, but r_{comm} should at least cover the gap between neighboring vehicles, i.e., $r_{\text{comm}} \geq s \cdot t_{\text{gap}}$. Moreover reducing r_{comm} results in more hops and thus higher end-to-end latency. In broadcast modes, $\omega_{HB}, \omega_{MB} \propto \lambda_{\text{vehicle}}$, while in unicast modes, $\omega_{HU}, \omega_{MU} \propto$

$\lambda^2_{\text{vehicle}}$. If $r_{\text{comm}} \propto s \cdot t_{\text{gap}} = 1/\lambda_{\text{vehicle}}$, i.e., covers the gap between back-to-back vehicles, the required capacity (except for ω_{HB}) does not change with λ_{vehicle}. Finally we note that when sharing HD data, the required V2V link capacity is proportional to the range of interest t_{interest}.

Based on these rough arguments let us consider the required capacity for a typical freeway scenario where: $l = 6$, $\Delta = 0.5$, $t_{\text{gap}} = 2$s, $s = 20$m/s, $t_{\text{interest}} = 10$s, r_{comm} is set to be the minimum, i.e., $r_{\text{comm}} = s \cdot t_{\text{gap}} = 40$m. Let $\nu = 50$ Mbps [38], then the lowest capacity requirement is broadcasting with merged data, $\omega_{MB} \geq 900$ Mbps, while the highest capacity requirement is for HD data with unicast, $\omega_{HU} \geq 54000$ Mbps. Note that even the lowest capacity requirement above is well beyond the capacity of current standards like IEEE 802.11p. If omni-directional transmissions were to be used, this analysis suggests that sharing HD data might be hard, and merging data and broadcasting will be necessary to reduce the network capacity requirements.

However, enabling V2V communications in the mmWave band has the potential to support the massive data rates required by collaborative sensing [39] [40]. If full-duplex mmWave unicast were used, the capacity requirement for V2V links, ω, would simply be the application per vehicle throughput requirements. The highest link capacity requirement, i.e., HD data unicast, in the above freeway scenario is 3000 Mbps, which can likely only be supported by mmWave technologies. Unfortunately mmWave links are subject to blockages, which might help reduce interference but makes the delivery of data to distant obstructed vehicles difficult, or results in higher delays due to additional multi-

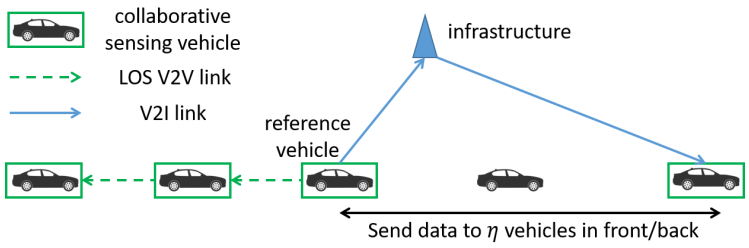

Figure 4.13: Collaborative sensing of vehicles in a single lane with V2V + V2I network. Vehicle uses V2I to relay data when LOS V2V links are blocked.

hoping.

4.4.2 Capacity Scaling in V2V+V2I Network

We envisage both V2V and V2I connectivity might be used to enable collaborative sensing in automotive settings. This might be critical to meet reliability and coverage requirements as we transition from legacy systems. In particular when the penetration of collaborative sensing vehicles is limited, the mmWave V2V links/paths required to share collaborative sensing data may be blocked/unavailable. When this is the case, V2I connectivity could serve as the fallback to share critical sensing/manouvering information. Below we study the V2I fallback capacity requirements scaling in the collaborative sensing penetration p_s.

We first consider a vehicle which is located on a single lane road according to the same model introduced in Section 4.4.1 with a penetration p_s. A sensing vehicle thus needs to send data to $\eta = \lfloor \frac{t_{\text{interest}}}{t_{\text{gap}}} \rfloor$ other vehicles in front and behind it, see Fig. 4.13. A vehicle has LOS V2V communication

channels to the neighboring vehicles in front and back. A non collaborating vehicle thus blocks the V2V relay path along the chain of vehicles. If a LOS V2V relay path is not available, we assume the reference vehicle relays data through the infrastructure and the receiving vehicle can then further relay data to upstream/downstream or vehicles via available V2V links. Let N_{UL} and $N_{\mathrm{DL}}^{\mathrm{U}}$ be random variables denoting the number of uplink and unicast downlink V2I transmissions required by a sensing vehicle. The expected required V2I uplink capacity c_{UL} and V2I downlink capacity for broadcast, $c_{\mathrm{DL}}^{\mathrm{B}}$, and unicast, $c_{\mathrm{DL}}^{\mathrm{U}}$, are given in the following theorem. The proof is in the appendix (Section 4.6.4).

Theorem 4.4.2. *Under the single lane model, the density of vehicles is $\lambda_{\mathrm{vehicle}}$, each sensing vehicle share data with $\eta = \lfloor t_{\mathrm{interest}}/t_{\mathrm{gap}} \rfloor$ vehicles in front and back. The V2I capacity requirements on a infrastructure serving the linear road segment of length $d\,\mathrm{m}$ are given by*

$$c_{\mathrm{UL}} = c_{\mathrm{DL}}^{\mathrm{B}} = p_s \cdot \lambda_{\mathrm{vehicle}} \cdot d \cdot \mathrm{E}[N_{\mathrm{UL}}] \cdot \nu, \tag{4.20}$$

$$c_{\mathrm{DL}}^{\mathrm{U}} = p_s \cdot \lambda_{\mathrm{vehicle}} \cdot d \cdot \mathrm{E}[N_{\mathrm{DL}}^{\mathrm{U}}] \cdot \nu, \tag{4.21}$$

where

$$\mathrm{E}[N_{\mathrm{UL}}] = 1 - \Big(\sum_{k=0}^{\eta} p_s^k \cdot (1-p_s)^{\eta-k}\Big)^2, \tag{4.22}$$

$$\mathrm{E}[N_{\mathrm{DL}}^{\mathrm{U}}] = \begin{cases} 2(\eta-1)p_s(1-p_s), & \text{if } \eta \geq 2, \\ 0, & \text{otherwise} \end{cases}. \tag{4.23}$$

The above results convey the *average* capacity requirements on V2I infrastructure. Unfortunately a single non-collaborating vehicle can block the

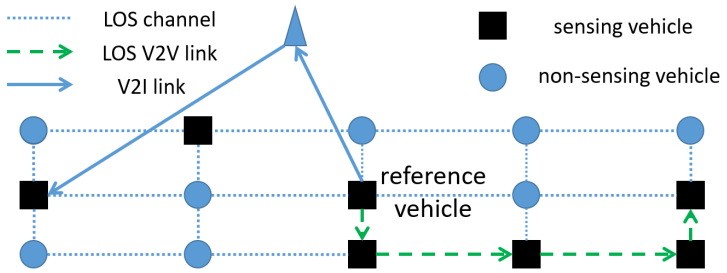

Figure 4.14: Collaborative sensing of vehicles in a single lane using V2V + V2I, with V2V relay assistance from vehicles in the two neighboring lanes.

V2V LOS links amongst a large number of vehicles and result in a *burst* of V2I traffic especially at high penetrations, e.g., when vehicles in front and back of the non-collaborating vehicle are all collaborating. The required V2I capacity to handle such bursts can thus be much higher.

The single lane relaying scenario studied above is a worst case, i.e., data can only be relayed by vehicles on the same lane. One can also consider scenarios where in addition collaborative vehicles on either of two neighboring lanes participate in V2V relaying. LOS links among vehicles on neighboring lanes are less likely to be blocked, but LOS links to distant vehicles in neighboring lanes will see larger path loss and may experience more interference, e.g., from transmissions of vehicles in the same lane. Thus for simplicity suppose vehicles only communicate with the closest vehicle in a neighboring lane and consider the simple grid connectivity model shown in Fig. 4.14. Each node on the grid corresponds to a vehicle, and each row represents a lane. Vehicles have LOS channels to neighboring vehicles on the grid. For comparison purposes we suppose, as before, that the reference vehicle needs to send data to η vehicles

in front and back in the *same* lane. Vehicles can receive data via V2V links if there is an LOS V2V relay path on the grid. To limit the number of hops and associated delays, we assume that a relay path can not include links in *both* forward and backward directions.

Based on this model, whether vehicles in the $(k+1)^{th}$ column from the reference vehicle can receive data via V2V links depends on whether the vehicles in the $(k+1)^{th}$ column are collaborating and can get data from vehicles in the kth column. In this setting one can again compute the expected V2I capacity requirements to deliver data to vehicles in each column and thus the total capacity requirements as a function of η and p_s – a detailed analysis is included in the appendix.

4.4.3 Numerical Results

Fig. 4.15 exhibits how the V2I capacity, c_{UL}, $c_{\mathrm{DL}}^{\mathrm{B}}$ and $c_{\mathrm{DL}}^{\mathrm{U}}$, normalized by $\lambda_{\mathrm{vehicle}} \cdot d \cdot \nu$ and the average V2V throughput per sensing vehicle normalized by V2V throughput at $p_s = 1$, vary with p_s in single lane and single lane assisted by vehicles in neighboring lanes scenarios. The results correspond to the case where $\eta = 5$. An increase in p_s causes an increase in the number of vehicles participating in collaborative sensing but also results in improved V2V connectivity. When p_s is small, both the number of collaborative sensing vehicles and the capacity per sensing vehicle increase, thus V2I traffic increases. However at higher penetrations, V2V connectivity improves and the V2I capacity requirements of a sensing vehicle decreases, resulting in

lower and eventually negligible V2I traffic. Comparing the results with and without assistance from vehicles in neighboring lanes, we observe, as expected, that V2I traffic is smaller when vehicles in neighboring lanes can help relay data. The V2V throughput per sensing vehicle increases with p_s. Note that if vehicles in neighboring lanes assist V2V relaying, the V2V throughput is higher than that in single lane scenario, and the c_{V2V} can be higher than the V2V throughput at full penetration.

Although the average V2I capacity is small at high penetrations, infrastructures may still see a burst in V2I traffic, e.g., failure in a single vehicle can block the V2V data flow along the fleet of vehicles and V2I is needed to relay all the data from vehicles in the front and behind. In Fig. 4.16 we consider the difference in average V2I capacity required at an infrastructure, given that a reference vehicle changes from a sensing and communicating vehicle to a non-collaborative vehicles. At low penetrations, the traffic relayed by a typical vehicle is limited, and V2I may also be needed to help relay the sensor data generated by the reference vehicle. Infrastructures should still have the ability to relay high rate V2V traffic.

In summary the V2I traffic resulting from collaborative sensing data would be highest at intermediate penetrations, e.g., ranging from 0.5 to 0.7, but eventually would decline once most vehicles participate in both collaborative sensing and V2V networking. This suggests an evolution path where V2I resources are initially critical to safety-related services like collaborative sensing, but eventually at high penetrations of sensing vehicles, traffic can

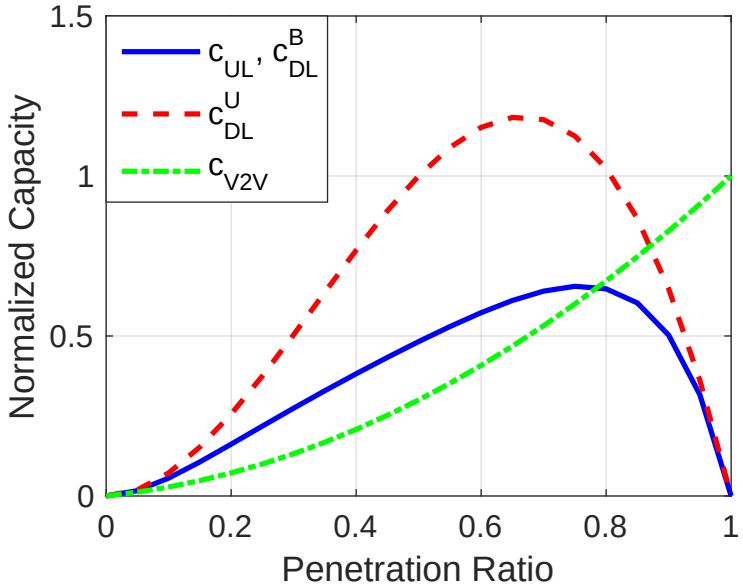

(a) Single lane

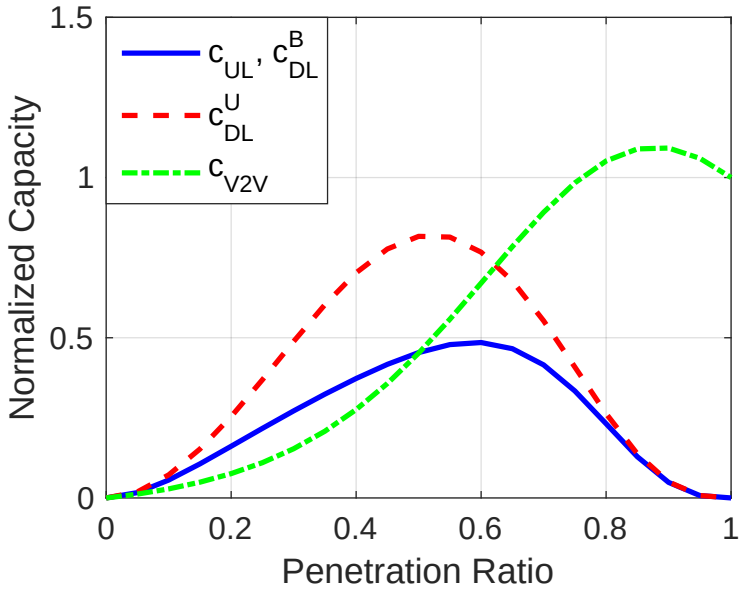

(b) Single lane assisted by neighbors

Figure 4.15: How V2I capacity requirements, normalized by $\lambda_{\text{vehicle}} \cdot d \cdot \nu$, scale with p_s in (a) single lane and (b) single lane assisted by vehicles in neighbor lanes. c_{UL} is uplink capacity, c^{B}_{DL} and c^{U}_{DL} are downlink capacity using broadcast and unicast. c_{V2V} is V2V throughput per sensing vehicle normalized by the V2V throughput at full penetration, $p_s = 1$.

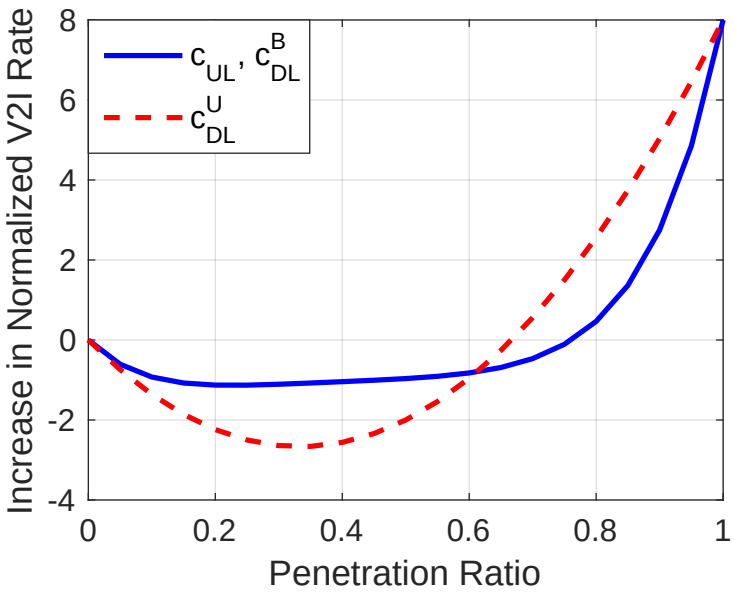

Figure 4.16: Difference in total V2I capacity when a sensing vehicle becomes disconnected in single lane scenario.

be effectively offloaded to V2V network, e.g., in the single lane assisted by neighboring lanes, $c_{\mathrm{UL}}, c^{\mathrm{B}}_{\mathrm{DL}}$ per vehicle is less than 0.25ν if $p_s > 0.8$, and the infrastructure may transition to supporting non-safety-related services, e.g., mobile high data rate entertainment and dynamic digital map update. These results are likely robust to improved models, yet more detailed analysis based on more accurate V2V mmWave channel and networking models would be needed to provide more accurate quantitative assessment.

4.5 Conclusion

Collaborative sensing can greatly improve a vehicle's sensing coverage and reliability, but suffers at low penetrations due to, both a lack of available

collaborators, and blockages in (mmWave) V2V relaying paths. Access to V2I connectivity will thus be important to provide communication for collaborative sensing when V2V relaying paths are unavailable. At higher penetrations, the average V2I traffic is low, but the infrastructure should still have the ability to support traffic bursts when the V2V network becomes disconnected.

To provide higher reliability one might consider supporting joint collaborative sensing amongst vehicles and RSUs with both sensing and communication capabilities. With sufficient RSU density and unobstructed placements, one can ensure 100% 1-coverage by collaborating only with RSUs. The associated capacity requirement can also be much smaller than collaboration with vehicles: vehicles receive data from one RSU instead of all neighboring vehicles. However sensing based only on RSUs deployed with 100% 1-coverage might not provide enough sensing redundancy and deploying even more RSUs to provide diversity would be costly. Furthermore, in order to navigate in a variety of environments, vehicles will need to have their own sensing capabilities which should clearly be leveraged. Thus we see the combination of vehicular/RSU collaborative sensing as the most cost effective way to achieve high coverage and reliability in vehicular automated driving applications.

4.6 Appendix: Proofs and Additional Results

4.6.1 Proof of Theorem 4.1.4

Proof. The locations associated marks of the objects, $\tilde{\Phi}$, follow an IMPPP, thus the occupied region can be modeled by a Boolean Process [57]. One can

thus properly define the distribution as seen by a typical vehicle referred to the origin 0. Let $Z^0 = (0, M^0)$, $M^0 = (A^0, Y^0, S^0)$, denote the typical vehicle. We let

$$f(x, z^0, \tilde{\phi}\backslash\{z^0\}) = \mathbb{1}(x \in c^0) \tag{4.24}$$

be the indicator function that location x is in the coverage set of the typical sensor z^0, where $\tilde{\phi}\backslash\{z^0\}$ denotes the other objects in the environment excluding z^0. The expected area of coverage set is given by,

$$\begin{aligned} \mathrm{E}[|C^0|] &= \mathrm{E}\Big[\int_{x\in\mathbb{R}^2} f(x, Z^0, \tilde{\Phi}\backslash\{Z^0\})dx\Big] \\ &= \int_{x\in\mathbb{R}^2}\int_{m\in\mathbb{M}}\int_{\tilde{\phi}} f(x, \tilde{\phi}\backslash\{z\}, z)P_z^!(d\tilde{\phi})F_{M^0}(dm)dx, \end{aligned} \tag{4.25}$$

where $\mathbb{M}$ is the support of M^0, $P_z^!(\cdot)$ is the reduced Palm distribution of $\tilde{\Phi}$ given a typical object is $z = (0, m)$, i.e., the distribution of other objects in the environment as seen by a typical object. For a Boolean Process, it follows by Slivnyak-Mecke theorem [57] that the reduced Palm distribution is the same as that of the original Boolean Process. Thus we have

$$\begin{aligned} &\int_{\tilde{\phi}} f(x, z, \tilde{\phi}\backslash\{z\})P_z^!(d\tilde{\phi}) = \int_{\tilde{\phi}} f(x, z, \tilde{\phi})P_{\tilde{\Phi}}(d\tilde{\phi}) \\ &\overset{(1)}{=} \mathbb{1}(x \in (\{y\} \oplus s) \cap a) + \mathbb{1}(x \in (\{y\} \oplus s)\backslash a)e^{-\lambda \mathrm{E}_A[|l_{y,x}\oplus \check{A}|]}, \end{aligned} \tag{4.26}$$

where $(\{y\} \oplus s)\backslash a$ is the sensing support of the typical sensor excluding the region covered by the typical sensor. In equality (1) we have used the fact that in a Boolean Process, the number of objects intersecting with a compact convex shape, e.g., $l_{y,x}$, has a Poisson distribution with mean $\lambda \cdot \mathrm{E}_A[|l_{y,x} \oplus \check{A}|]$, $\check{A} = \{x| - x \in A\}$ [57]. Apply the result of Eq. 4.26 to Eq. 4.25 and we get Eq. 4.3. □

4.6.2 Proof of Theorem 4.2.2

Proof. The locations of the objects follow an HPPP and the environment can be modeled as an IMPPP thus the environment is homogeneous in space. Without loss of generality we consider the redundancy of location 0. By definition, we have

$$\mathrm{E}[R(\tilde{\Phi}, \Phi^s, 0)|0 \notin E] = \frac{\mathrm{E}[R(\tilde{\Phi}, \Phi^s, 0) \cdot \mathbb{1}(x \notin E)]}{\mathrm{P}(0 \notin E)} \tag{4.27}$$

The region occupied by objects follow the Boolean Process thus the probability that 0 is not occupied by objects is given by, see [57],

$$\mathrm{P}(0 \notin E) = e^{-\lambda \cdot \mathrm{E}[|A|]}. \tag{4.28}$$

We let $h(x_0, x, m, \tilde{\phi} \backslash \{(x, m)\})$ be the indicator function that location x_0 is in the void space and sensed by object (x, m), given the environment excluding the reference object is $\tilde{\phi} \backslash \{(x, m)\}$. $\mathrm{E}[R(\tilde{\Phi}, \Phi^s, 0) \cdot \mathbb{1}(0 \notin E)]$ is then given by,

$$\begin{aligned}
&\mathrm{E}[R(\tilde{\Phi}, \Phi^s, 0) \cdot \mathbb{1}(0 \notin E)] \\
=&\mathrm{E}\left[\sum_{(X_i, M_i) \in \tilde{\Phi}, X_i \in \Phi^s} h\big(0, X_i, M_i, \tilde{\Phi} \backslash \{(X_i, M_i)\}\big)\right] \\
=&p_s \lambda \int_{x \in \mathbb{R}^2} \int_{m \in \mathbb{M}} \int_{\tilde{\phi}} h(0, x, m, \tilde{\phi}) P^!_{(x,m)}(d\tilde{\phi}) F_M(dm) dx \\
\overset{(1)}{=}&p_s \lambda \int_{x \in \mathbb{R}^2} \mathrm{E}_{M, \tilde{\Phi}}\big[h(0, x, M, \tilde{\Phi})\big] dx \\
\overset{(2)}{=}&p_s \lambda \int_{x \in \mathbb{R}^2} \mathrm{E}_{M, \tilde{\Phi}}\big[h(-x, 0, M, \tilde{\Phi})\big] dx \\
\overset{(3)}{=}&p_s \lambda \cdot \mathrm{E}[|C^0 \backslash A^0|].
\end{aligned} \tag{4.29}$$

The equality (1) follows for Slivnyak-Mecke theorem [57]. Equality (2) follows from the spatial homogeneity of the environmental model thus we have that

$$\mathrm{E}_{M,\tilde{\Phi}}\big[h(0,x,M,\tilde{\Phi})\big] = \mathrm{E}_{M,\tilde{\Phi}}\big[h(-x,0,M,\tilde{\Phi})\big]. \tag{4.30}$$

Equality (3) follows from the result of $\mathrm{E}[|C^0|]$ in Thm. 4.1.4. Note that function h is not equal to f introduced in the proof of Thm. 4.1.4, i.e., a point on the boundary of an object can be in the coverage set but can not be in the void space. However the area of the set of such points is 0, thus equality (3) holds. Combining the above results and we finish the proof.

□

4.6.3 Proof of Theorem 4.4.1

Proof. Denote by ρ the throughput per vehicle after scheduling. The average number of vehicles in the protection region of a vehicle, is roughly $2(1+\Delta)r_{\mathrm{comm}}\lambda_{\mathrm{vehicle}}$. There is at most one transmitting vehicle in a protection region, thus the highest throughput per vehicle is given by

$$\rho \leq \frac{\omega}{2l(1+\Delta)r_{\mathrm{comm}}\lambda_{\mathrm{vehicle}}}. \tag{4.31}$$

Denote by n_{tx} the minimum number of transmissions one piece of data needs to be sent, ρ should satisfy that

$$\rho \geq n_{\mathrm{tx}} \cdot \nu. \tag{4.32}$$

In HB mode, to cover all vehicles within $s \cdot t_{\mathrm{interest}}$ in both forward and backward directions using broadcast, the minimum number of transmissions

is roughly given by

$$n_{\text{tx}}^{HB} = 2 \cdot \left\lfloor \frac{s \cdot t_{\text{interest}}}{r_{\text{comm}}} \right\rfloor - 1. \tag{4.33}$$

In HU mode, the minimum n_{tx}^{HU} is the number of vehicles in the region of interest, i.e., $n_{\text{tx}}^{RU} = 2l \cdot s \cdot t_{\text{interest}} \cdot \lambda_{\text{vehicle}}$. If the vehicles share merged data, each vehicle only needs to transmit to vehicles within r_{comm}, i.e., $n_{\text{tx}}^{MB} = 1$ and $n_{\text{tx}}^{MU} = 2l \cdot r_{\text{comm}} \cdot \lambda_{\text{vehicle}}$. Combine the results on n_{tx}, Eq. 4.31 and Eq. 4.32, then we get the lower bounds on ω. □

4.6.4 Proof of Theorem 4.4.2

Proof. Consider the expected number of V2I transmissions required by a typical sensing vehicle.

V2I uplink. The probability that the V2I link will be required to share sensor data with collaborating vehicles in one direction, e.g., forward direction, is given by

$$p_{\text{front}}(\eta, p_s) = 1 - \sum_{k=0}^{\eta} p_s^k \cdot (1 - p_s)^{\eta - k}. \tag{4.34}$$

This expression can be interpreted as one minus the probability (associated with the sum) that the V2I link is not required: V2I link is not required if the first k vehicles are collaborative and can thus perform V2V relaying, and the remaining $\nu - k$ are not and so do not require the data. The forward and backward directions are independent and symmetric, thus the probability that V2I resources will be required is

$$p_{\text{V2I}}(\eta, p_s) = 1 - \big(1 - p_{\text{front}}(\eta, p_s)\big)^2. \tag{4.35}$$

Data need only sent up once irrespective of whether one or more sharing paths are blocked thus $\mathrm{E}[N_{\mathrm{UL}}] = p_{\mathrm{V2I}}$.

V2I downlink. If broadcast downlink is used, we have $N_{\mathrm{DL}}^{\mathrm{B}} = N_{\mathrm{UL}}$, thus $\mathrm{E}[N_{\mathrm{DL}}^{\mathrm{B}}] = \mathrm{E}[N_{\mathrm{UL}}]$. If only unicast downlink is available, a V2I downlink is required for every collaborative vehicle where no LOS V2V relay path is available. Given our modeling assumption that vehicles receiving data from infrastructure can further relay data via V2V links, the $(k+1)^{th}$ collaborative vehicle requires a downlink transmission if the kth vehicle is not sensing. $\mathrm{E}[N_{\mathrm{DL}}^{\mathrm{U}}]$ is the summation of the expected number of unicast downlink required by each kth vehicle and thus we have Eq. 4.23.

Given the expected V2I transmissions of a typical sensing vehicle, we get c_{UL}, $c_{\mathrm{DL}}^{\mathrm{B}}$, and $c_{\mathrm{DL}}^{\mathrm{U}}$ accordingly.

□

4.6.5 V2I Capacity with V2V Relay by Vehicles in Neighbor Lanes

Consider the vehicles in front of a reference vehicle placed in column 0 of the grid. Let $S_k = (S_k^1, S_k^2, S_k^3)$, $S_k^i \in \{0, 1\}$, denote whether the vehicles in the kth column from the reference vehicle ($1, 2, 3$ denotes vehicles from top row to bottom row) are collaborating where 0 denotes a non-collaborating vehicle and 1 the opposite. Denote by $X_k = (X_k^1, X_k^2, X_k^3)$, $X_k^i \in \{0, 1\}$, the state of the vehicles in the kth column are both collaborating and can receive data from the reference vehicle. We denote by $Y_k \in \{0, 1\}$ whether V2I downlink is required to relay sensing data to vehicles in the *first* k columns. The state of

the kth column is given by

$$Z_k = (X_k, Y_k). \tag{4.36}$$

Based on our assumption that relaying paths can not contain links in both forward and backward directions, X_{k+1} only depends on X_k and S_{k+1}. Since whether a vehicle is collaborating is independent from other vehicles, the probability distribution of Z_{k+1} depends on that of Z_k and p_s.

Denote by P the state transition probability of state from Z_k to Z_{k+1}, $k \geq 0$. The probability distribution of S_{k+1} is given by,

$$\mathrm{P}\left(S_{k+1} = (s_k^1, s_k^2, s_k^3)\right) = p_s^{s_k^1+s_k^2+s_k^3} \cdot (1-p_s)^{3-s_k^1-s_k^2-s_k^3}. \tag{4.37}$$

Denote by $\tilde{X}_{k+1}$ the indicator of whether vehicles in the kth column can send data to vehicles in the $(k+1)^{th}$ column via V2V links. Denote by $\wedge$ logical AND, $\vee$ logical OR, we have

$$\tilde{X}_{k+1} = (X_k^1 \wedge S_{k+1}^1, X_k^2 \wedge S_{k+1}^2, X_k^3 \wedge S_{k+1}^3). \tag{4.38}$$

Further consider the communication amongst vehicles in the same column. Denote by $\hat{X}_{k+1}$ the state of vehicles after vehicles in the $(k+1)^{th}$ column share data amongst themselves via V2V links, we have

$$\hat{X}_{k+1}^1 = \tilde{X}_{k+1}^1 \vee (S_{k+1}^1 \wedge (\tilde{X}_{k+1}^2 \vee (\tilde{X}_{k+1}^3 \wedge S_{k+1}^2))), \tag{4.39}$$

$$\hat{X}_{k+1}^2 = \tilde{X}_{k+1}^2 \vee (S_{k+1}^2 \wedge (\tilde{X}_{k+1}^1 \vee \tilde{X}_{k+1}^3)), \tag{4.40}$$

$$\hat{X}_{k+1}^3 = \tilde{X}_{k+1}^3 \vee (S_{k+1}^3 \wedge (\tilde{X}_{k+1}^2 \vee (\tilde{X}_{k+1}^1 \wedge S_{k+1}^2))), \tag{4.41}$$

i.e., a sensing vehicle can also receive data from other collaborating vehicles in the same column via V2V relaying.

For V2I relaying, we denote by $\tilde{Y}_{k+1}$ whether V2I relaying is required by the k+1th column. This occurs if the vehicle in the central lane is collaborating but can not receive data via V2V links, i.e., when

$$(S^2_{k+1} = 1) \text{ and } (\hat{X}^2_{k+1} = 0), \tag{4.42}$$

we have $\tilde{Y}_{k+1} = 1$. The vehicle can further relay data to neighboring collaborative vehicles in the $(k+1)^{th}$ column. The state transition is now given by

$$Y_{k+1} = Y_k \vee \tilde{Y}_{k+1}, \tag{4.43}$$

$$X_{k+1} = \begin{cases} \hat{X}_{k+1}, & \text{if } \tilde{Y}_{k+1} = 0 \\ S_{k+1}, & \text{otherwise} \end{cases}. \tag{4.44}$$

Based on the above state transition rules, we can compute P based on p_s. Denote by $\mathcal{Z}$ the support of Z_k, $\pi_k = (\pi^1_k, \pi^2_k, \ldots, \pi^{|\mathcal{Z}|}_k)$ the probability distribution of Z_k, where π^i_k is the probability of state i at column k. We have that

$$\pi_k = P^k \cdot \pi_0. \tag{4.45}$$

Denote by $\mathcal{Z}_{\text{V2I}} \subseteq \mathcal{Z}$ the set of states with $Y = 1$. The probability that V2I communication is required to relay data to vehicles in the forward direction, conditioning on the probability distribution of column Z_0 being π_0, is given by

$$p_{\text{front}}(\eta, p_s, \pi_0) = \sum_{i \in \mathbb{Z}_{\text{V2I}}} \pi^i_\eta, \tag{4.46}$$

where $\pi_\eta = P^\eta \pi_0$. Conditioning that the reference vehicle is a sensing vehicle, we can compute π_0 based on p_s. p_{V2I} is thus given by

$$p_{\text{V2I}} = \sum_{i=1,\ldots,|\mathcal{Z}|} \pi_0^i \cdot \big(1 - (1 - p_{\text{front}}(\eta, p_s, e_i))^2\big), \tag{4.47}$$

where $e_i \in \{0,1\}^{|\mathcal{Z}|}$, $e_i^i = 1$ and $e_i^j = 0$ for $j \neq i$.

For the number of $\mathrm{E}[N_{\text{DL}}^{\text{U}}]$, we can define Y_k as the state for number of V2I unicast downlinks required by vehicles in each column. Similarly as above, we can compute the corresponding state transition probability and $\mathrm{E}[N_{\text{DL}}^{\text{U}}]$ is given by

$$\mathrm{E}[N_{\text{DL}}^{\text{U}}] = \sum_{k=1}^{\eta} \mathrm{E}[Y_k] \tag{4.48}$$

In the above analysis we assume the reference vehicle only needs to share data to vehicles in the same lane, e.g., vehicles are moving in platoons and mainly require data from the same platoon. In fact, vehicles may also need to share data with vehicles in neighboring lanes for applications like advanced automated driving and collaborative sensing [37]. In this case we can analyze the required capacity on V2I network following similar steps. One major difference is that the condition in Eq. 4.42 should be replaced by

$$\exists i \in \{1,2,3\} \text{ s.t. } \hat{X}_{k+1}^i \neq S_{k+1}^i, \tag{4.49}$$

i.e., there is a sensing vehicle not receiving the sensor data via V2V relay. Also in Eq. 4.44 we have $X_{k+1} = S_{k+1}$, i.e., all sensing vehicles would get the data by either V2V or V2I.

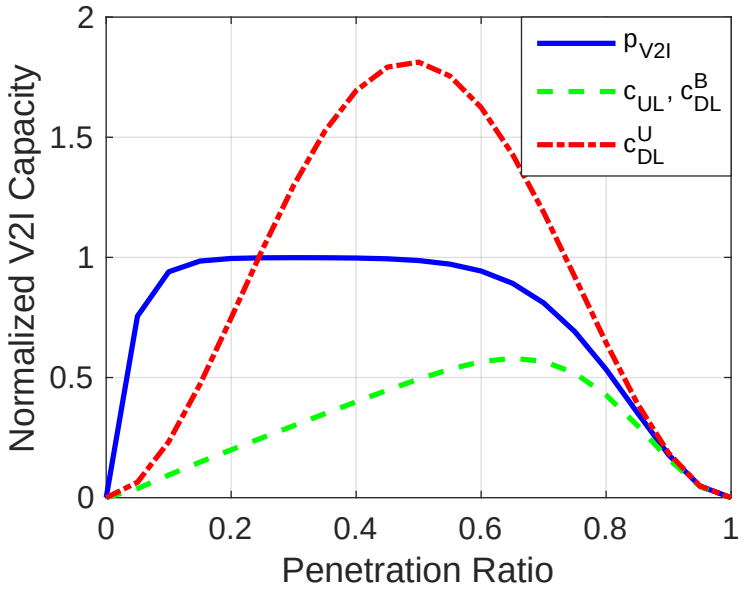

Figure 4.17: How $p_{\mathrm{V2I}}(\eta, p_s)$, normalized c_{UL}, $c^{\mathrm{B}}_{\mathrm{DL}}$, and $c^{\mathrm{U}}_{\mathrm{DL}}$ change with p_s when vehicles send data to vehicles in the same lane and the two neighboring lanes.

In Fig. 4.17 we exhibit the result when vehicles need to share data with vehicles on neighboring lanes. Compared with the case that vehicle needs to share data with only vehicles in the same lane, the V2I capacity requirements here is much higher. Such result is as expected as more vehicles are requiring data. Note that p_{V2I} is almost 1 for a large range of penetrations, e.g., from 0.1 to 0.6. This indicate that assistance from V2I would be necessary for reliable collaborative sensing ever since the early stage of the penetration of automated driving vehicles.

Chapter 5

Infrastructure Assisted Collaborative Sensing

In this chapter we explore the performance of infrastructure assisted sensing of roads under various deployment schemes.

5.1 Comparison of RSU and Cellular Based Sensing

In this section we study the performance of infrastructure based sensing, i.e., sensing performed by infrastructure without the help of vehicles, under two deployment scenarios:

- sensors on RSUs placed along the road,
- sensors on cellular infrastructure, e.g., BSs, which are randomly placed in space.

We provide a comparison of the two approaches leveraging simple stochastic geometry models.

5.1.1 System Model

We model the road system using a Manhattan Poisson line process (MPLP) [65] on an infinite 2D plane, see [66] [67]. The road network is modeled

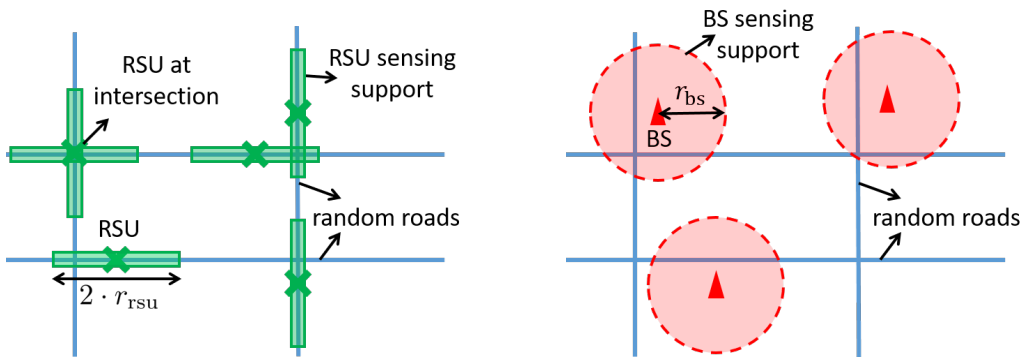

(a) RSU based sensing (b) Cellular based sensing

Figure 5.1: Manhattan Poisson line process model for roads. (a) Model for RSU based sensing. (b) Model for cellular (BS) based sensing.

based on two HPPPs, $\Psi_x, \Psi_y \subset \mathbb{R}$, along the x-axis and y-axis respectively. At each point of Ψ_x (Ψ_y) there is a vertical (horizontal) line corresponding to a road. We shall initially neglect the width of the roads in this section. The intensities of Ψ_x and Ψ_y, $\lambda^{\text{v}}_{\text{road}}$ and $\lambda^{\text{h}}_{\text{road}}$, corresponding to the density of vertical and horizontal roads. The total density of roads, and the average length of roads per unit area, are both given by

$$\lambda_{\text{road}} = \lambda^{\text{h}}_{\text{road}} + \lambda^{\text{v}}_{\text{road}}. \tag{5.1}$$

See Fig. 5.1 for example.

RSU based sensing We shall assume RSUs are distributed along each road with intensity μ_{rsu} RSUs/meter, resulting in a spatial density of RSUs, λ_{rsu}, given by,

$$\lambda_{\text{rsu}} = \lambda_{\text{road}} \cdot \mu_{\text{rsu}}. \tag{5.2}$$

We shall assume RSUs are distributed along each road with intensity μ_{road} RSUs/m, resulting in a spatial density

$$\lambda_{\text{rsu}} = \lambda_{\text{road}} \cdot \mu_{\text{rsu}}. \tag{5.3}$$

For simplicity we assume a road can only be sensed by RSUs deployed along the road, i.e., RSUs on other roads are obstructed. RSUs are placed above vehicles and objects on the road, thus are assumed to be able to sense all objects on the road. An RSU deployed at an intersection can sense all the roads joining at the intersection. We consider three ways of deploying RSUs:

1. randomly distributed, i.e., RSUs follow HPPP(μ_{road}) along each road;
2. evenly spaced, RSUs are deployed along roads at an interval $1/\mu_{\text{rsu}}$;
3. first deployed at intersections, then randomly deployed along roads.

The optimal placement of RSUs is beyond the scope of this work, thus we only consider the above simple approaches. Placing RSUs at intersections and/or at even spacings would be most effective in covering roads with fewest RSUs. However in early stage of deployments, RSUs may be placed at busy road segments first, and subject to environmental limitations, e.g., availability of backbone infrastructure power and RSU installation space. The deployment of RSUs may also consider performance of communication, e.g., [68] [69] [70]. These considerations may bring randomness to the placement of RSUs, and the HPPP model represents a "worst case" deployment with the most randomness.

RSU deployments in the real world would likely to be a compromise among these deployment models.

Cellular based sensing Cellular BSs are typically modeled as randomly placed on the 2D plane, i.e., follow an HPPP with intensity λ_{BS} [65] [71]. We assume each base station has a sensing support in the shape of a disc with radius r_{BS}, e.g., a BS located at x can sense the region $b(x, r_{\mathrm{BS}})$ if unobstructed, see Fig. 5.1b. Unlike dedicated RSUs along the road, we model cellular based sensing as being subject to building obstructions. We consider the 3D model shown in Fig. 5.2. Consider a typical location, 0, on the center of a typical horizontal road, i.e., the x-axis (we neglect other roads).[1] We assume there is a minimum distance from the road to locations where cellular infrastructure can be placed (i.e., width of road + sidewalk) given by $d_{\mathrm{road}}^{\mathrm{BS,min}}$, and BSs follow an HPPP(λ_{BS}) on the set

$$D_{\mathrm{BS}} = (-\infty, \infty) \times \big((-\infty, -d_{\mathrm{road}}^{\mathrm{BS,min}}) \cup (d_{\mathrm{road}}^{\mathrm{BS,min}}, \infty)\big). \tag{5.4}$$

The height of BSs is h_{BS}.

Buildings are the only obstructions. Each building is associated with a location $X_{\mathrm{b}} \in \mathbb{R}^2$ and a 3D shape modeled by a random cuboid parametrized by

$$A_{\mathrm{b}} = (L_{\mathrm{b}}, W_{\mathrm{b}}, H_{\mathrm{b}}),$$

[1] It is straight forward that the results for vertical roads would be similar.

where $L_{\mathrm{b}}, W_{\mathrm{b}}, H_{\mathrm{b}} \in \mathbb{R}^{+}$ correspond to the length, width and height of the cuboid. The side corresponding to L_{b} is assumed to be parallel to the road. The location of the building, X_b, is at the center of the side closest to the road. Note that X_b is on different sides for buildings above and below the road. See Fig. 5.2a for an example. We assume the shape of buildings are independent of the locations of the buildings, and building shapes are independent of each other. We assume the locations of buildings follow an HPPP of intensity λ_{b} in

$$D_{\mathrm{b}} = (-\infty, \infty) \times \big((-\infty, -d_{\mathrm{road}}^{\mathrm{b,min}}) \cup (d_{\mathrm{road}}^{\mathrm{b,min}}, \infty)\big), \tag{5.5}$$

i.e., ensuring that the minimum distance from the side of a building to the road is $d_{\mathrm{road}}^{\mathrm{b,min}}$.

The location 0 can be viewed by a sensor at location x if it falls in the sensing range of the sensor, i.e.,

$$|l_{0,x}| \leq r_{\mathrm{BS}}. \tag{5.6}$$

and there are no buildings obstructing the LOS sensing channel. Indeed consider the LOS sensing channel between 0 and a BS located at x. Denote by $l_{0,x} \in \mathbb{R}^2$ the line segment between 0 and x, $|l_{0,x}|$ the length of the segment. Suppose there is a building of height h_{b}, whose projection on the plane occupies a region $e \subseteq \mathbb{R}^2$ with area $l_{\mathrm{b}} \times w_{\mathrm{b}}$. Let $\rho \cdot (x_1, x_2) = (\rho \cdot x_1, \rho \cdot x_2)$. The projection on the plane of the part of the sensing channel which is subject to obstructions of height h_{b}, i.e., lower than h_{b}, is given by a segment $l_{0,\rho\cdot x}$, where $\rho = \min(1, h_{\mathrm{b}}/h_{\mathrm{BS}})$, The building will obstruct the channel if $e \cap l_{0,\rho\cdot x} \neq \emptyset$. See Fig. 5.2b for an example.

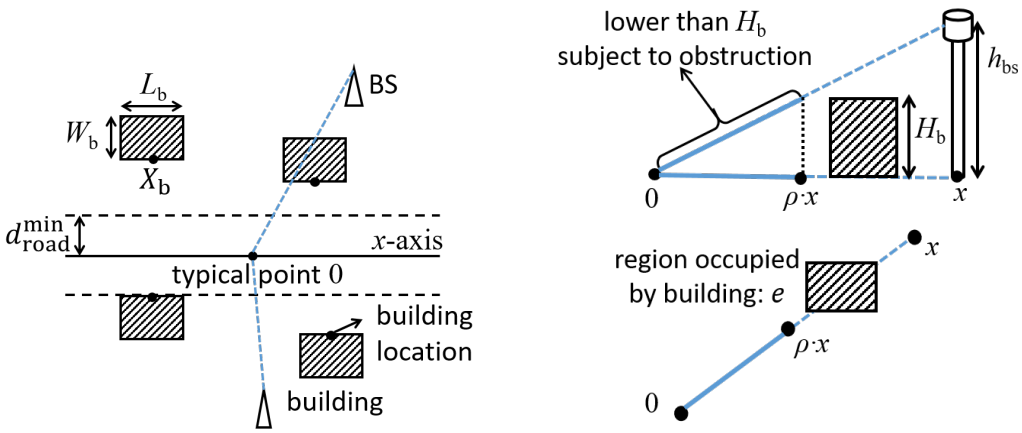

(a) Cellular based sensing model

(b) Side and top view of channel

Figure 5.2: (a) model for cellular based sensing under building obstruction (in rural area). In the example shown, we assume $d_{\text{road}}^{\text{BS,min}} = d_{\text{road}}^{\text{b,min}} = d_{\text{road}}^{\text{min}}$ (b) the side and top view of an example for channel obstruction. The path lower than h_b is subject to building obstruction.

The above obstruction model is roughly appropriate for sparse suburban/rural areas where building densities are low and buildings can be approximated as randomly distributed. In dense urban areas, the building density can be high, and we may suppose the buildings fill the city blocks separated by roads. In the latter case, the buildings can be tall thus it will be difficult for a BS to have a good LOS coverage of a road which is one block away, see Fig. 5.3. For better sensing coverage (and LOS channels for mmWave communication), cellular based sensors should be located on the sides of the buildings next to roads, which then becomes similar to our assumptions on RSU placement. The performance of sensing would then be similar to that of RSUs but perhaps placed at a larger height.

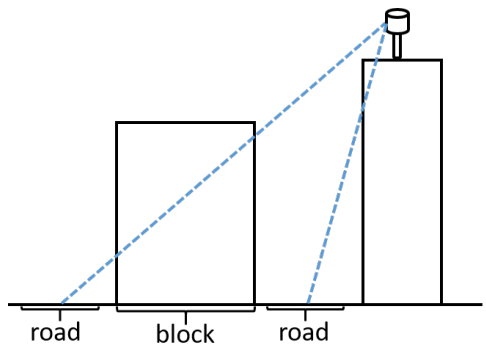

Figure 5.3: Cellular based sensing can be heavily obstructed in dense urban area.

We shall examine the *coverage of roads*, i.e., the proportion of roads covered by at least one sensor, under different sensor deployment schemes given road density λ_{road} and sensor spatial density λ_{rsu} (and building density λ_{b}).

5.1.2 RSU Based Sensing Coverage

Randomly distributed RSUs. For each road, the coverage of RSUs follows a 1D Poisson Boolean process [53]. For a fixed spatial density of RSUs λ_{rsu} and roads λ_{road}, the locations of RSUs on a road follows an HPPP with intensity

$$\mu_{\text{rsu}}^{\text{rand}} = \frac{\lambda_{\text{rsu}}}{\lambda_{\text{road}}}, \tag{5.7}$$

and each RSU covers a segment of length $2 \cdot r_{\text{rsu}}$, thus it follows that the number of RSUs covering a typical location on the road, $N_{\text{rsu}}^{\text{rand}}$, has a Poisson distribution with mean

$$\text{E}[N_{\text{rsu}}^{\text{rand}}] = \mu_{\text{rsu}}^{\text{rand}} \cdot (2 \cdot r_{\text{rsu}}). \tag{5.8}$$

The road coverage is thus given by

$$\begin{aligned} p_{\text{cover}}^{\text{rsu,rand}}(\lambda_{\text{rsu}}, r_{\text{rsu}}, \lambda_{\text{road}}) &= \Pr(N_{\text{rsu}}^{\text{rand}} > 0) \\ &= 1 - e^{-\operatorname{E}[N_{\text{rsu}}^{\text{rand}}]} \\ &= 1 - e^{-\frac{\lambda_{\text{rsu}}}{\lambda_{\text{road}}} \cdot 2 \cdot r_{\text{rsu}}}. \end{aligned} \tag{5.9}$$

Evenly spaced RSUs. The distance between two neighboring RSUs is $\frac{1}{\mu_{\text{rsu}}^{\text{even}}} = \frac{\lambda_{\text{road}}}{\lambda_{\text{rsu}}}$, thus the proportion of road covered is easily shown to be

$$p_{\text{cover}}^{\text{rsu,even}}(\lambda_{\text{rsu}}, r_{\text{rsu}}, \lambda_{\text{road}}) = \min\left\{1, 2 \cdot r_{\text{rsu}} \cdot \frac{\lambda_{\text{rsu}}}{\lambda_{\text{road}}}\right\}. \tag{5.10}$$

RSUs at intersections along with randomly distributed RSUs. In the MPLP model, the intersections on a horizontal road follow an HPPP of intensity $\lambda_{\text{road}}^{\text{v}}$, and the density of horizontal roads is $\lambda_{\text{road}}^{\text{h}}$, thus the spatial density of intersections in the MPLP model is given by

$$\lambda_{\text{inter}} = \lambda_{\text{road}}^{\text{h}} \cdot \lambda_{\text{road}}^{\text{v}}. \tag{5.11}$$

Note since $\lambda_{\text{road}} = \lambda_{\text{road}}^{\text{h}} + \lambda_{\text{road}}^{\text{v}}$, when $\lambda_{\text{road}}^{\text{h}} = \lambda_{\text{road}}^{\text{v}}$ the intersection density is given by $\lambda_{\text{inter}} = \frac{\lambda_{\text{road}}^2}{4}$. Also note that the intersection density is maximized when $\lambda_{\text{road}}^{\text{h}} = \lambda_{\text{road}}^{\text{v}}$. If $\lambda_{\text{rsu}} \leq \lambda_{\text{inter}}$, we assume each intersection has a probability $\lambda_{\text{rsu}}/\lambda_{\text{inter}}$ of having an RSU and there are no RSUs off intersections. If $\lambda_{\text{rsu}} > \lambda_{\text{inter}}$, each intersection has an RSU and in addition each road has randomly distributed RSUs with linear density $\mu_{\text{rsu}}^{\text{rand}}$, where $\mu_{\text{rsu}}^{\text{rand}}$ is such that the total spatial density of RSUs, including RSUs at intersections and randomly distributed RSUs, is equal to λ_{rsu}. The coverage is given in the following theorem. The proof is given in the appendix (Section 5.6.1).

Theorem 5.1.1. *Under the above RSU deployment at road intersections in the Manhattan Poisson line process model, the coverage of horizontal roads is given by,*

$$p_{\text{cover}}^{\text{rsu,inter,h}}(\lambda_{\text{rsu}}, r_{\text{rsu}}, \lambda_{\text{road}}^{\text{h}}, \lambda_{\text{road}}^{\text{v}}) = \begin{cases} 1 - e^{-\frac{\lambda_{\text{rsu}}}{\lambda_{\text{road}}^{\text{h}}} \cdot (2 \cdot r_{\text{rsu}})}, & \text{if } \lambda_{\text{rsu}} \leq \lambda_{\text{road}}^{\text{h}} \cdot \lambda_{\text{road}}^{\text{v}} \\ 1 - e^{-\mu_{\text{rsu}}^{\text{total}} \cdot (2 \cdot r_{\text{rsu}})}, & \text{otherwise,} \end{cases}, \tag{5.12}$$

where

$$\mu_{\text{rsu}}^{\text{total,h}} = \frac{\lambda_{\text{rsu}} + (\lambda_{\text{road}}^{\text{v}})^2}{\lambda_{\text{road}}^{\text{h}} + \lambda_{\text{road}}^{\text{v}}}, \tag{5.13}$$

is the linear density of RSUs on a typical horizontal road when $\lambda_{\text{rsu}} > \lambda_{\text{road}}^{\text{h}} \cdot \lambda_{\text{road}}^{\text{v}}$. *The coverage of vertical roads is given by*

$$p_{\text{cover}}^{\text{rsu,inter,v}}(\lambda_{\text{rsu}}, r_{\text{rsu}}, \lambda_{\text{road}}^{\text{h}}, \lambda_{\text{road}}^{\text{v}}) = p_{\text{cover}}^{\text{rsu,inter,h}}(\lambda_{\text{rsu}}, r_{\text{rsu}}, \lambda_{\text{road}}^{\text{v}}, \lambda_{\text{road}}^{\text{h}}), \tag{5.14}$$

i.e., by exchanging $\lambda_{\text{road}}^{\text{h}}$ *and* $\lambda_{\text{road}}^{\text{v}}$ *in* $p_{\text{cover}}^{\text{rsu,inter,h}}$.

Note that if $\lambda_{\text{road}}^{\text{h}} \neq \lambda_{\text{road}}^{\text{v}}$, the density of intersections on horizontal and vertical roads are not the same. Placing more RSUs on roads with fewer intersections can provide better coverage.

5.1.3 Cellular Based Sensing Coverage

Cellular coverage without obstructions. The 2D coverage of unobstructed BSs follows a simple 2D Poisson Boolean process [53], which results in a proportion of covered roads:

$$p_{\text{cover}}^{\text{BS}}(\lambda_{\text{BS}}, r_{\text{BS}}) = 1 - e^{-\lambda_{\text{BS}} \cdot \pi \cdot r_{\text{BS}}^2}. \tag{5.15}$$

Cellular coverage under obstruction. We let $A^0 = (L^0, W^0, H^0)$, where $L^0, W^0, H^0 \in \mathbb{R}^+$, denote a typical random cuboid whose dimensions have the same distribution as buildings. For a BS located at x, we denote by $E(x, A^0) \subseteq \mathbb{R}^2$ the footprint of a typical building located on the same side of the road as the BS at x. The shape of the typical building is A^0 and $E(x, A^0)$ is referenced to the location of the building, see Fig. 5.4. The average number of BSs sensing a typical location 0 is characterized in the following theorem.

Theorem 5.1.2. *Under our obstruction model, the number of BSs sensing a typical location* 0*,* $N^{\mathrm{o}}_{\mathrm{BS}}$*, has mean*

$$\mathrm{E}[N^{\mathrm{o}}_{\mathrm{BS}}] = \lambda_{\mathrm{BS}} \cdot \int_{D_{\mathrm{BS}} \cap b(0, r_{\mathrm{BS}})} e^{-\mathrm{E}[N_{\mathrm{b}}(x)]} dx, \tag{5.16}$$

where

$$\mathrm{E}[N_{\mathrm{b}}(x)] = \lambda_{\mathrm{b}} \cdot \mathrm{E}_{A^0}\left[\left|(l_{0,\rho(A^0)\cdot x} \oplus \check{E}(x, A^0)) \cap D_{\mathrm{b}}\right|\right] \tag{5.17}$$

is the expected number of buildings blocking a BS located at x*,* $l_{0,\rho(A^0)\cdot x}$ *is the line segment between* 0 *and* $\rho(A^0) \cdot x$*,* $\rho(A^0) = \min(1, \frac{H^0}{h_{\mathrm{BS}}})$*,* $\oplus$ *is the Minkowski sum [53],* $\check{E}(x, A^0) = \{y | -y \in E(x, A^0)\}$*.*

The proof follows by Campbell's theorem [53] and is given in the appendix (Section 5.6.2). If the densities of buildings and BSs are low, the sensing channels between 0 and different BSs can be approximated as independent. $N^{\mathrm{o}}_{\mathrm{BS}}$ thus follows a Poisson distribution with the same mean and the probability that the location 0 is covered by at least one BS is given by

$$p^{\mathrm{BS,o}}_{\mathrm{cover}}(\lambda_{\mathrm{BS}}, r_{\mathrm{BS}}, \lambda_{\mathrm{b}}) = 1 - e^{-\mathrm{E}[N^{\mathrm{o}}_{\mathrm{BS}}]}, \tag{5.18}$$

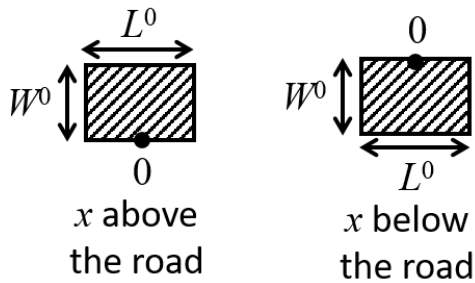

Figure 5.4: $E(x, A^0)$ denotes the footprint of a typical building, which has a shape A^0 and located on the same side of the road as the BS at x, referenced to the building's location.

where $\mathrm{E}[N^{\mathrm{o}}_{\mathrm{BS}}]$ is given in Eq. 5.16.

Model for blockage density. We can see from Eq. 5.18 that the coverage of obstructed BSs depends on building density λ_{b}, instead of road density λ_{road}. It is natural to expect the road density to be positively correlated with the building density, e.g., a correlation of over 60% was found in the generalized least squares regression model developed in [72]. In our work we will use a very simple model for building density, i.e.,

$$\lambda_{\mathrm{b}} = c \cdot \lambda_{\mathrm{road}}, \tag{5.19}$$

where c is a constant such that $\lambda_{\mathrm{b}} = \frac{1}{400}/\,\mathrm{m}^2$ (medium building density) at $\lambda_{\mathrm{road}} = 6\,\mathrm{km}\,/\,\mathrm{km}^2$. The actual relationship between λ_{b} and λ_{road} is more complicated and we use this simple model to study the scaling of cellular coverage qualitatively.

5.1.4 Comparisons

Other road models. Our analysis will focus on the MPLP road model. Other road models include (non-random) Manhattan grid model [62], and Poisson line process [73]. In these models, our analysis on RSU and cellular based sensing remain valid, except for the case where RSUs are placed at intersections. In Manhattan grid model, the topology of the roads is deterministic and the analysis of coverage is straight forward. For the Poisson line process the results are similar to the MPLP model and a detailed analysis is included in the appendix. The qualitative results and implications on infrastructure deployment are similar in these models.

Let us compare the minimum required spatial sensor density to achieve a target coverage probability, $p_{\text{cover}}^{\min}$. Let $\lambda_{\text{rsu}}^{\text{rand,min}}$, $\lambda_{\text{rsu}}^{\text{even,min}}$, $\lambda_{\text{rsu}}^{\text{inter,min}}$, $\lambda_{\text{BS}}^{\min}$, and $\lambda_{\text{BS}}^{\text{o,min}}$ be the minimum sensor density to provide at least $p_{\text{cover}}^{\min}$ coverage in the five schemes discussed above.

We study how the required sensor density scales in the road densities and coverage requirements. Fig. 5.5 illustrates how the required sensor density to achieve $p_{\text{cover}}^{\min} = 90\%$ coverage as one varies the road density, e.g., from sparse rural to dense urban areas. $r_{\text{rsu}} = r_{\text{BS}} = 200\,\text{m}$, and we let $\lambda_{\text{road}}^{\text{h}} = \lambda_{\text{road}}^{\text{v}}$. For cellular sensing obstruction model, we assume the buildings have the same dimensions, $l_{\text{b}} = l_{\text{b}} = 14\,\text{m}$, $h_{\text{b}} = 3\,\text{m}$. The BSs are placed at a height $h_{\text{BS}} = 15\,\text{m}$, and $d_{\text{road}}^{\text{BS,min}} = d_{\text{road}}^{\text{b,min}} = 10\,\text{m}$, i.e., two 3.5 m lanes and 3 m sidewalk. Note that we only present result in obstructed cellular based sensing for $\lambda_{\text{road}} \leq 6\,\text{km}/\,\text{km}^2$. At larger road densities, the buildings may

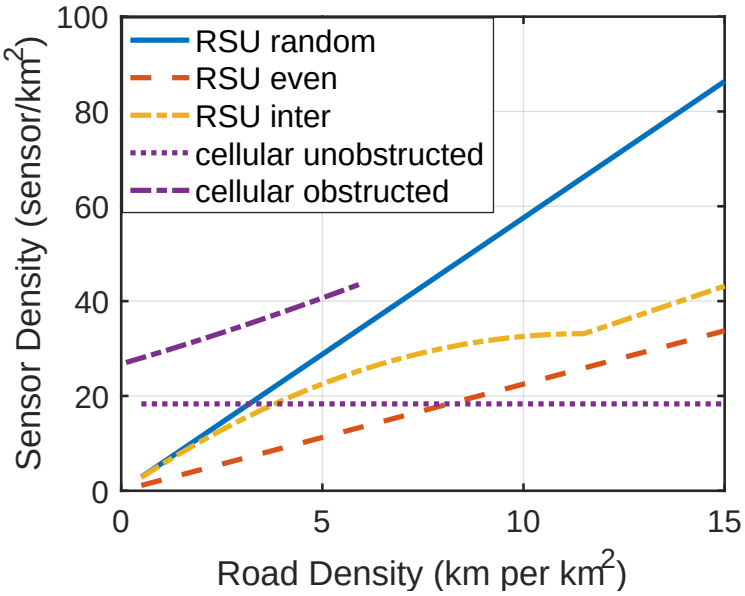

Figure 5.5: Required sensor densities to achieve 90% coverage at different road densities for different schemes. 'RSU random' RSUs randomly located along roads; 'RSU even' RSUs located along the road at even space; 'RSU inter' RSUs first deployed at intersections and remaining RSUs randomly located along roads; 'cellular' cellular based sensing without obstruction; 'cellular obstructed' cellular based sensing subject to obstruction.

be tall and close to to each other. BSs may only sense the roads surrounding the BSs, and cellular based sensors may be deployed and work as (randomly deployed) RSUs. Fig. 5.6 exhibits the required sensor density for different coverage requirement. The road density is $\lambda_{\text{road}} = 6\,\text{km}\,/\,\text{km}^2$, while other parameters are the same as those in Fig. 5.5.

Benefit of placing RSUs at intersections. Deploying RSUs at intersections can double the coverage benefit per RSU, so the required sensor density can in principle be reduced by half as compared to random deployment, i.e.,

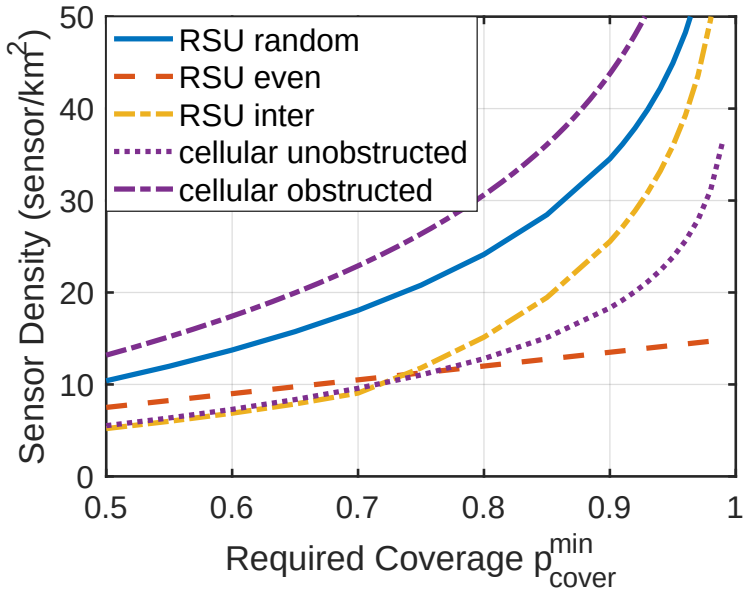

Figure 5.6: How the required spatial sensor density scales in the coverage requirement $p_{\text{cover}}^{\text{min}}$.

$\lambda_{\text{rsu}}^{\text{inter,min}} = \frac{1}{2}\lambda_{\text{rsu}}^{\text{rand,min}}$. More precisely the relationship between $\lambda_{\text{rsu}}^{\text{inter,min}}$ and $\lambda_{\text{rsu}}^{\text{rand,min}}$ (when $\lambda_{\text{road}}^{\text{h}} = \lambda_{\text{road}}^{\text{v}}$) is given by

$$\lambda_{\text{rsu}}^{\text{inter,min}} = \begin{cases} \lambda_{\text{rsu}}^{\text{rand,min}} - \frac{\lambda_{\text{road}}^2}{4} & \text{if } \lambda_{\text{road}} \leq \sqrt{2 \cdot \lambda_{\text{rsu}}^{\text{rand,min}}} \\ \frac{1}{2} \cdot \lambda_{\text{rsu}}^{\text{rand,min}} & \text{otherwise} \end{cases}. \tag{5.20}$$

See the results for 'RSU random' and 'RSU inter' in Fig. 5.5. When λ_{inter} is low, the difference between $\lambda_{\text{rsu}}^{\text{rand,min}}$ and $\lambda_{\text{rsu}}^{\text{inter,min}}$, i.e., $\frac{\lambda_{\text{road}}^2}{4}$ in Eq. 5.20, increases with road density λ_{road}. At high road densities, e.g., $\lambda_{\text{road}} \geq 11\,\text{km}\,/\,\text{km}^2$ in Fig. 5.5, deploying RSUs only at (some of) the intersections is enough to provide the required coverage and the required RSU density is reduced by half.

Random v.s. evenly located RSUs. If RSUs are distributed at even spacings, there is no overlap among the coverage of RSUs (at low RSU densities)

and $\lambda_{\text{rsu}}^{\text{even,min}} < \lambda_{\text{rsu}}^{\text{rand,min}}$. We can derive from Eq. 5.9 and Eq. 5.10 that

$$\lambda_{\text{rsu}}^{\text{rand,min}} \propto -\log(1 - p_{\text{cover}}^{\text{min}}), \tag{5.21}$$

$$\lambda_{\text{rsu}}^{\text{even,min}} \propto p_{\text{cover}}^{\text{min}}. \tag{5.22}$$

As $p_{\text{cover}}^{\text{min}} \to 1$, the minimum sensor densities for random deployment schemes, i.e., $\lambda_{\text{rsu}}^{\text{rand,min}}$, $\lambda_{\text{rsu}}^{\text{inter,min}}$, $\lambda_{\text{BS}}^{\text{min}}$ and $\lambda_{\text{BS}}^{\text{o,min}}$, go to infinity while $\lambda_{\text{rsu}}^{\text{even,min}}$ increases linearly with $p_{\text{cover}}^{\text{min}}$ and is bounded. Deploying RSUs at even spacings minimizes the required RSU density. $\lambda_{\text{rsu}}^{\text{even,min}}$ can be further reduced by placing RSUs at intersections. However when deploying RSUs at intersections, the distance between RSUs is not necessarily multiple of the sensing range, thus overlap between RSUs might be inevitable. Optimal deployment of RSUs will thus depend on the actual topology of the roads.

RSU based sensing v.s. cellular based sensing. In RSU based sensing, the required sensor density increases linearly with road density while if there are no obstructions in cellular based sensing, the required sensor density does not scale with road density. This indicates that the sensor density and associated cost in cellular based sensing could be smaller than RSU based sensing at high road densities. The required sensor density depends on sensing ranges, r_{rsu} and r_{BS}. Based on our analysis, the required sensor density in RSU sensing is inversely proportional to r_{rsu} while the required density in unobstructed cellular based sensing is proportional to $1/r_{\text{BS}}^2$. Consider randomly distributed RSU and cellular based sensing without obstructions, the minimum sensor

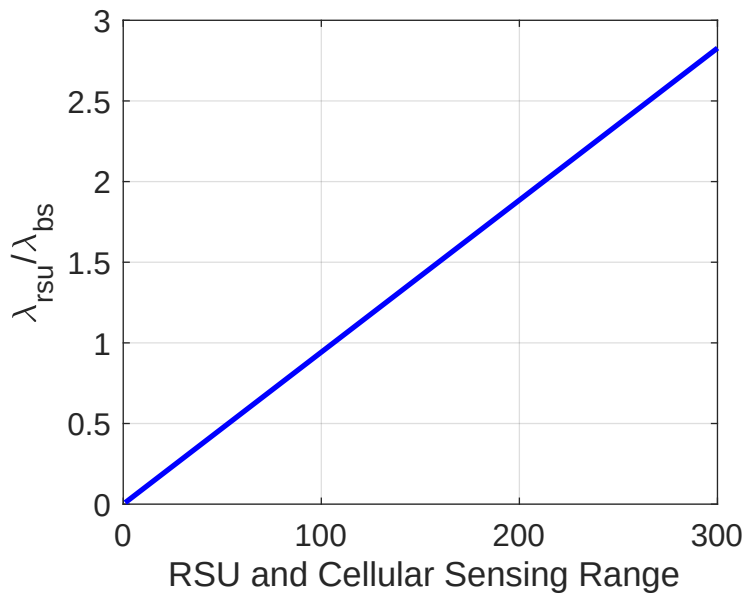

Figure 5.7: How $\lambda_{\text{rsu}}^{\text{rand,min}}/\lambda_{\text{BS}}^{\text{min}}$ scales in sensing range, $r_{\text{rsu}} = r_{\text{BS}}$.

densities to achieve the same coverage should satisfy

$$\lambda_{\text{rsu}}^{\text{rand,min}} = \frac{\pi \cdot r_{\text{BS}}^2 \cdot \lambda_{\text{road}}}{2 \cdot r_{\text{rsu}}} \cdot \lambda_{bs}^{\text{min}}. \tag{5.23}$$

It is clear that cellular based sensing is more beneficial when the sensing range is large and road density is high. Fig. 5.7 illustrates how the ratio between $\lambda_{\text{rsu}}^{\text{rand,min}}$ and $\lambda_{\text{BS}}^{\text{min}}$, i.e., $\lambda_{\text{rsu}}^{\text{rand,min}}/\lambda_{\text{BS}}^{\text{min}}$, scales in the sensing range, $r_{\text{BS}} = r_{\text{rsu}}$, at road density $\lambda_{\text{road}} = 6\,\text{km}/\text{km}^2$. The ratio increases linearly with sensing range and we have $\lambda_{\text{rsu}}^{\text{rand,min}} = \lambda_{\text{BS}}^{\text{min}}$ at $r_{\text{rsu}} = 106\,\text{m}$, i.e., the density of sensors is the same in both schemes in an urban setting when $r_{\text{rsu}} \approx 100\,\text{m}$. From Eq. 5.23 we can see the r_{rsu} threshold is proportional to $\frac{1}{\lambda_{\text{road}}}$. It is obvious that when cellular based sensing is subject to obstruction, the required sensor density increases with building density (and thus road density). Cellular based

sensing thus may not be more efficient than RSU based sensing. As we have discussed, cellular based sensing in dense urban area may only cover the roads surrounding the BSs and work similar to RSUs.

Conclusion. In this section we compared the performance of different infrastructure assisted sensing, including RSU and cellular based sensing. Deploying RSUs at even spacings (regularly) and at intersections reduces the required density of RSUs. When the road density is high and sensing range is large, it can be more beneficial to deploy sensors at BSs to cover multiple roads with one sensor. However there are more obstructions at high road densities, limiting the coverage of cellular based sensing to roads surrounding the BSs. This suggest that cellular based sensing will be at a disadvantage over RSU based sensing unless BSs are placed on the sides of buildings and/or along roads similarly to RSUs. These considerations will however be highly dependent on the available technologies and costs.

5.2 RSU Assisted Collaborative Sensing

In this section we study how the deployment and sensing capabilities of RSUs would impact the performance of vehicle collaborative sensing assisted by RSUs, i.e., vehicles share sensor data with neighboring collaborative vehicles and RSUs.

5.2.1 Sensing of Objects

Previously in this dissertation we focus on sensing the (void) locations, which is closely related to representing the environment using occupancy map or sharing raw sensor data. Sharing raw sensor data can be more reliable in case of accidents [38], but can be costly in the communication and processing of data. Modeling objects by their geometric shapes and additional information can be more efficient. Each object is modeled with a geometric shape and additional information, e.g., velocity. Such representation works well in tracking objects in dynamic environments and has much lower cost, i.e., lower cost in computation and communication, which makes it especially desirable in the early stage of automated driving. In the following sections, including the simulation of sensing with RSUs and temporal diversity of sensing, we shall study the sensing of objects using the metrics defined below.

We consider the same environmental model as the one for the sensing of locations introduced in Section 4.1. We first define the *objects of interest* of sensor i, O_i, based on the region of interest in Definition 4.1.2 as follows.

Definition 5.2.1. *(Objects of interest) Given sensor i's region of interest D_i, the* objects of interest *of sensor i, O_i, is defined as the set of objects overlapping with D_i, i.e.,*

$$O_i = \left\{ j \in \mathbb{N}^+ \middle| E_j \cap D_i \neq \emptyset \right\}. \tag{5.24}$$

We shall assume object j is sensed by sensor i if any part of object j is

sensed, i.e.,

$$E_j \cap C_i(\tilde{\Phi}) \neq \emptyset. \tag{5.25}$$

Similar to the sensing redundancy for a location in Definition 4.2.1, we define the *object sensing redundancy* of object i as follows.

Definition 5.2.2. *(Object sensing redundancy) Given an environment and sensing field $\tilde{\Phi}$, and a subset of collaborating sensors, $K \subseteq \Phi^s$, the* object sensing redundancy *of object i is defined as the number of sensors in K sensing object i, i.e.,*

$$R^{\mathrm{o}}(\tilde{\Phi}, K, i) = \sum_{j:X_j \in K} \mathbb{1}\left(E_i \cap C_j(\tilde{\Phi}) \neq \emptyset\right). \tag{5.26}$$

We also define the *object coverage* of sensor i based on the coverage of a location in Definition 4.2.3 as follows.

Definition 5.2.3. *(Object coverage and reliability) Given an environment and sensing field $\tilde{\Phi}$, a minimum redundancy requirement $\gamma \in \mathbb{N}^+$ for reliable sensing of objects, a subset of collaborating sensors, $K \subseteq \Phi^s$, and sensor i's objects of interest O_i, the* γ-object coverage set *of sensor i is the set of objects in O_i which are covered by at least γ sensors in K, denoted by*

$$C_c^{\mathrm{o}}(\tilde{\Phi}, K, O_i, \gamma) \triangleq \left\{ j \in O_i \middle| R^{\mathrm{o}}(\tilde{\Phi}, K, j) \geq \gamma \right\}. \tag{5.27}$$

The γ-object coverage *of sensor i is the cardinality of the γ-object coverage set,*

$$|C_c^{\mathrm{o}}(\tilde{\Phi}, K, O_i, \gamma)|. \tag{5.28}$$

The γ-object coverage reliability *is the* γ*-object coverage normalized by the area of region of interest,*

$$\frac{|C_c^{\mathrm{o}}(\tilde{\Phi}, K, O_i, \gamma)|}{|O_i|}. \tag{5.29}$$

In the detailed evaluation of collaborative sensing with RSUs, we would use the performance metrics on sensing of the objects.

5.2.2 RSU Assisted Collaborative Sensing Scenario

In our simulations we shall consider a 3D scenario, and the metrics are extended to 3D accordingly.

Sensing capabilities. We suppose each collaborative sensing vehicle is equipped with a sensor mounted on the central top of the vehicle. The sensing supports of sensors are discs centered at the sensor with radius r_{vehicle}. Sensors are subject to obstructions from neighboring vehicles (no self obstruction), and an object is assumed to be sensed by a sensor if any part of the object is sensed. Each sensing vehicle has a communication range r_{comm}. Fig. 5.8 illustrates collaborative sensing with infrastructure. We assume vehicles can receive sensor data from all sensors within communication range, including RSUs and other collaborative sensing vehicles.

Deployment of Infrastructure. The performance of infrastructure sensing depends on the deployment characteristics. Suppose the sensors are located at a height h_{rsu} above the ground, and the distance to the roadside is d_{road}. Suppose also the density of RSU units along the road is μ_{rsu} on one side of the

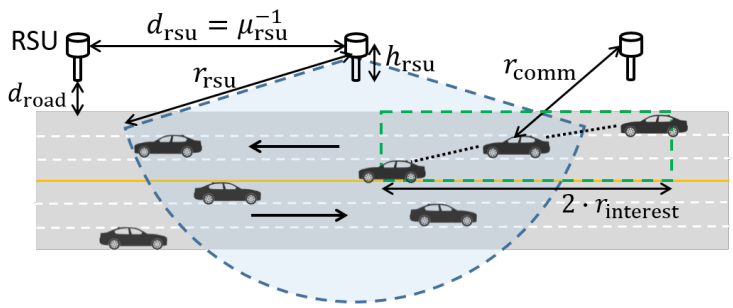

Figure 5.8: Collaborative sensing with infrastructure.

road. Denote by d_{rsu} the distance between the 1-D location of two neighboring sensors. d_{rsu} can be fixed, i.e., RSUs are regularly (or uniformly) distributed, or random, e.g., RSUs follow a Poisson process.

Collaborative sensing assumptions. In the following simulations of RSU assisted sensing, we shall assume vehicles are interested in the vehicles moving in the same direction, and communicate with vehicles moving in the same direction. Sensor data regarding vehicles in the same direction is more important, and V2V communication links are more stable. Sensing and communicating with vehicles in the same direction is likely to be used in the early stage of automated driving.

In the *base case*, $d_{\text{road}} = 2\,\text{m}$, $h_{\text{rsu}} = 3\,\text{m}$, $\mu_{\text{rsu}} = \frac{1}{400}\,\text{RSU}\,/\,\text{m}$, RSUs are distributed along the road at even spacings, i.e., $d_{\text{rsu}} = 400\,\text{m}$. $r_{\text{vehicle}} = r_{\text{rsu}} = 200\,\text{m}$, $r_{\text{comm}} = 200\,\text{m}$.

Note that under the above assumptions on sensing and communication range, there is exactly one RSU within the communication range of a vehicle. The RSUs are not sharing data with neighboring RSUs and the sensing support

of the RSU communicating with the vehicle may fail to cover the whole region of interest of the vehicle, undermining the benefits of RSUs. To get sensor data from all RSUs covering the vehicle's region of interest, the communication range needs to be sufficiently large, i.e.,

$$r_{\text{comm}} \geq r_{\text{interest}} + r_{\text{rsu}}. \tag{5.30}$$

Such communication range can be achieved by 1) extending vehicle-to-RSU communication range, which can be difficult for links in the mmWave band in dynamic and possibly obstructed environment; 2) relaying sensor data via V2V communication; and 3) RSUs sharing (and possibly merging) sensor data amongst RSUs via high rate wired or wireless links.

Simulation scenario. We consider a typical freeway scenario as described in [38], see Fig. 5.8 for example. There are three lanes in each direction, and the lane width is 4 m. Vehicles are randomly located in the lanes with the same distribution as used in Section 4.1. We simulate two types of vehicles modeled as rectangular cuboids, including sedans 4.8 m ×1.8 m ×1.5 m (length × width × height), and SUVs 5 m ×2 m ×1.8 m. Half of the vehicles are selected to be sedans while the other half are SUVs. Vehicles are moving at a velocity $s = 20\,\text{m}\,/\,\text{sec}$, the lane density of vehicles is $\mu_{\text{vehicle}} = \frac{1}{2 \cdot s} = 0.025$ vehicles/ m, e.g., the average distance between two neighboring vehicles in the same lane is 2 sec. The region of interest for a vehicle has a range of $r_{\text{interest}} = 10 \cdot s = 200\,\text{m}$ in both forward and backward directions, i.e., vehicles require a 10 sec prediction forward and backward of the environment.

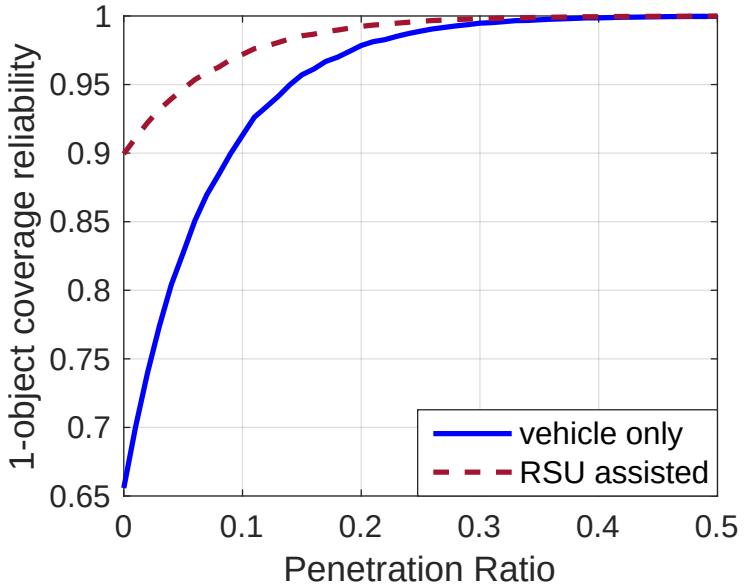

Figure 5.9: 1-object coverage reliability for the base case.

5.2.3 Numerical Results on RSU Sensing

Fig. 5.9 exhibits the 1-object coverage reliability for the base case. An RSU do have a good coverage of the road within its sensing support and the sensing support of RSUs almost cover the whole road. However a vehicle may fail to communicate with all sensors/RSUs sensing its objects of interest. In fact in the base case each vehicle can communicate with only one RSU, whose sensing support may be different from the vehicle's region of interest, thus the reliability is not 100%.

Communication range r_{comm}. Fig. 5.10 exhibits the results for different communication ranges. When $r_{\text{comm}} = 400\,\text{m}$, a vehicle can get sensor data from all RSUs sensing the objects of interest. We can see that the coverage

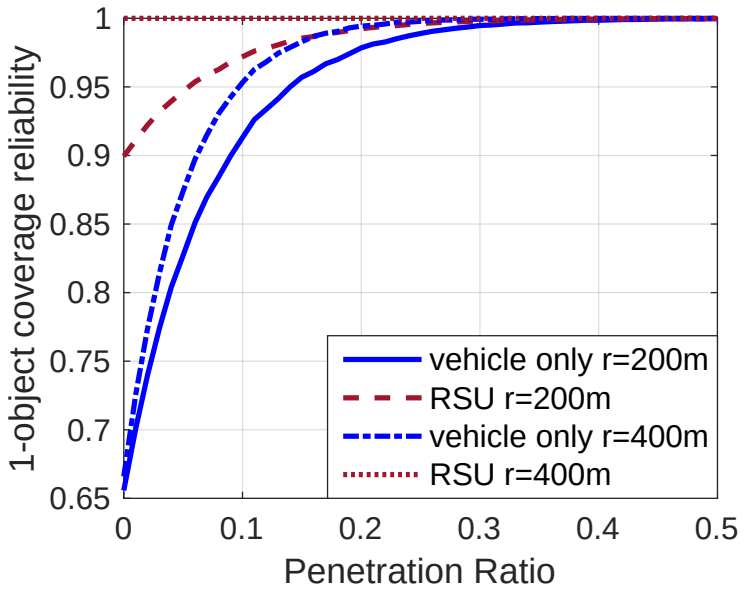

Figure 5.10: 1-object coverage reliability for different communication ranges: 200 m, 400 m. At $r_{\text{comm}} = 400\,\text{m}$, each vehicle can communicate with all RSUs that can sense its objects of interest.

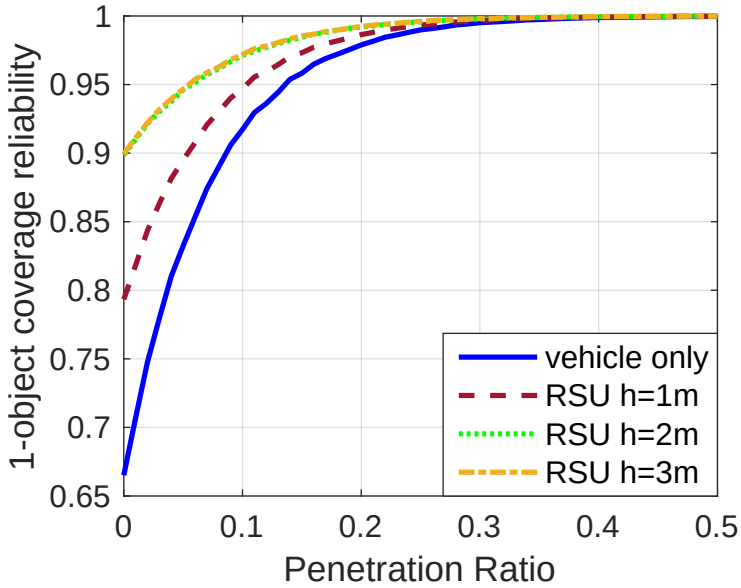

Figure 5.11: 1-object coverage reliability for different RSU heights: 1 m, 2 m, 3 m.

reliability is almost 1. This indicates that RSUs are almost not subject to obstructions from vehicles when the vehicles are moving at normal velocities (still see obstructions from large vehicles like trucks or when the vehicles are moving very slow and the distance between vehicles is small). It is more important to extend the range of communication so that each vehicle can get all sensor data regarding its region of interest. Feasible approaches are discussed in the end of Section 5.2.2.

Height of RSUs h_{rsu}. Fig. 5.11 shows the coverage reliability result for $h_{\text{rsu}} = 1\,\text{m}, 2\,\text{m}, 3\,\text{m}$. As expected, RSUs which are located higher have better coverage. Notice that once h_{rsu} is higher than the vehicles, the gain in object coverage reliability from increasing h_{rsu} is marginal. However RSUs at larger

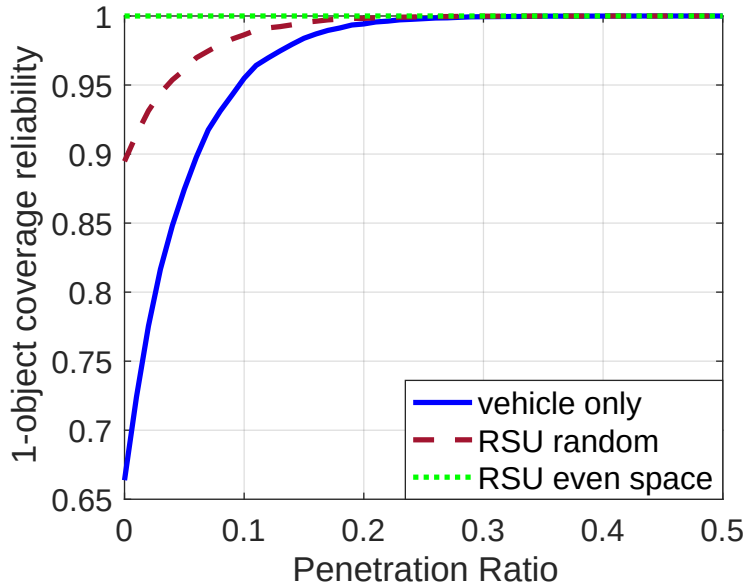

Figure 5.12: 1-object coverage reliability for different RSU deployment: 1) random: the locations of RSUs follow a Matérn process with minimum gap 50 m, and 2) even space. Communication range is $r_{\text{comm}} = 400\,\text{m}$.

heights can sense a larger proportion of objects' surfaces and roads.

Deployment regularity: evenly spaced or randomly located. In Fig. 5.12 we compare different RSU deployment regularities. We use a Matérn process [55] to model the distribution of RSUs, and set the minimum gap between vehicles to be 50 m. The communication range is set to be 400 m. When randomly distributed, RSUs may fail to cover some parts of the road, decreasing the 1-object coverage reliability. However there can be benefits of random placement: in some parts of the road may be covered by multiple RSUs, and the sensing reliability in these parts are higher.

Distance to road d_{rsu}. Fig. 5.13 shows the reliability result for different

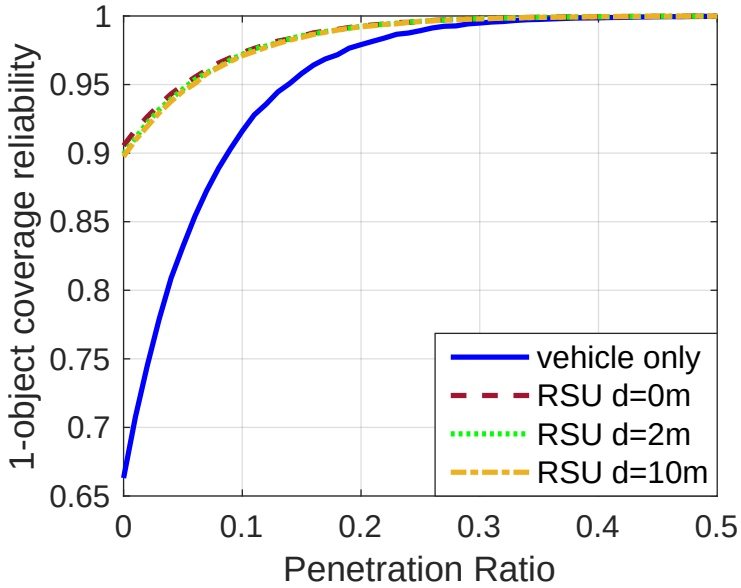

Figure 5.13: 1-object coverage reliability for RSUs deployed at different distances to road side d_{road}: 0 m, 2 m, and 10 m.

distances to road: $d_{\text{rsu}} = 0\,\text{m}, 2\,\text{m}, 10\,\text{m}$. There is no clear change in RSU coverage, indicating that d_{rsu} does not have much impact if RSUs are placed above the vehicles.

Density of RSUs μ_{rsu}. Fig. 5.14 exhibits the reliability result at different RSU densities: $\frac{1}{800}$ RSU / m, $\frac{1}{400}$ RSU / m, $\frac{1}{200}$ RSU / m. As expected the coverage increases with RSU density. At $\mu_{\text{rsu}} = \frac{1}{200}$ RSU / m the RSUs provide 2-coverage of the road, e.g., each location can be sensed by at least 2 RSUs. Vehicles can communicate with at least one RSU in both forward and backward directions, and have 100% coverage with the help from RSUs.

RSU sensing range r_{rsu}. In Fig. 5.15 we compare the results for different RSU sensing ranges, i.e., $r_{\text{rsu}} = 100\,\text{m}, 200\,\text{m}, 300\,\text{m}, 400\,\text{m}$. As expected

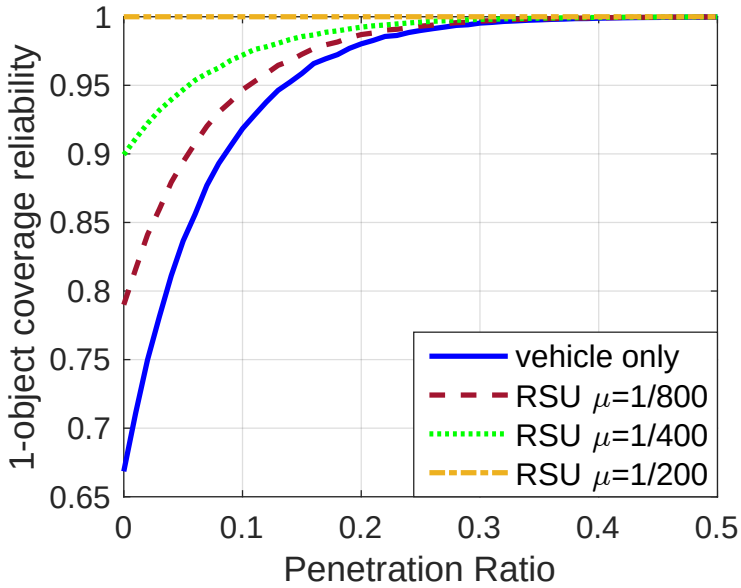

Figure 5.14: 1-object coverage reliability for different RSU densities: $\frac{1}{800}$ RSU / m, $\frac{1}{400}$ RSU / m, $\frac{1}{200}$ RSU / m.

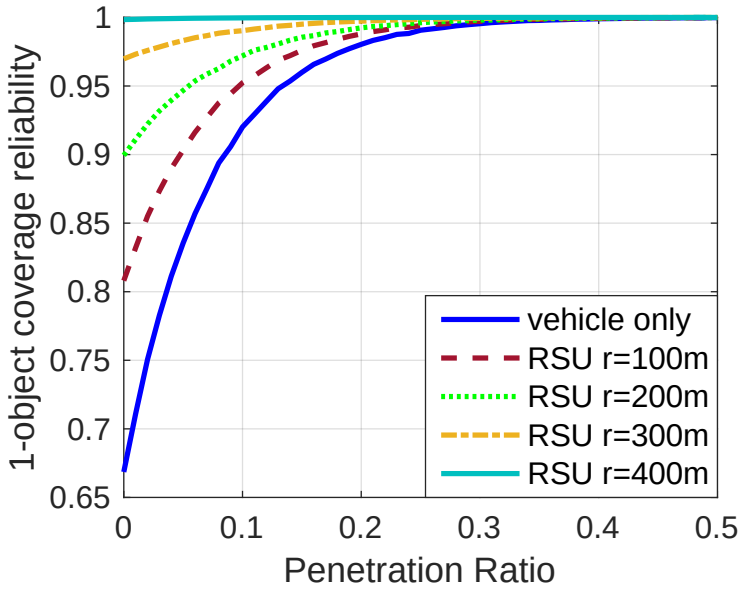

Figure 5.15: 1-object coverage reliability for different RSU sensing ranges r_{rsu}: 100 m, 200 m, 300 m, 400 m.

sensing coverage would increase with r_{rsu}.

Conclusion on the deployment of RSUs. Deploying schemes and RSU capabilities impact the performance of collaborative sensing with RSUs. Our results show that deploying sensing RSUs can greatly improve collaborative sensing performance, especially at low penetrations. RSUs are less likely to be subject to obstructions compared with sensing of vehicles. However to get the most from RSUs, we should extend the communication range between vehicles and RSUs, e.g., RSUs sharing sensor data with neighboring RSUs and send (possibly merged) data to vehicles.

5.3 Spatio-temporal Diversity in Collaborative Sensing

In the previous sections we studied how collaborative sensing improves coverage for a *snapshot* of the environment by providing spatial diversity in sensing, i.e., sensor data for locations and objects from different points of view. In addition, collaborative sensing can improve sensing performance via utilizing temporal diversity in sensing. Objects in the environment are moving thus the environment is dynamic, e.g., vehicles' regions of interest, blockage fields, and the sensor coverage sets are varying with time. Sensor data measured at different time provides possibly different information regarding the environment, thus sensors can utilize temporal diversity for sensing and tracking of objects in the environment.

5.3.1 Temporal Dynamic Environment and Sensing Model

We modify the environment and sensing model in Section 4.1 to capture temporal dynamics.

We let X_i be the location of object i at time 0, and denote by

$$\Phi^d(t) = \{X_i^d(t), i \in \mathbb{N}^+\}$$

the locations of objects at time t, where $X_i^d(t)$ is the location of object i at time t. Suppose the movements of objects are IID and independent of the locations of objects (during the time interval we are interested in). $\Phi \sim \text{HPPP}(\lambda)$ thus it follows the Displacement Theorem [57] that the locations of objects at any time t will remain an HPPP process, i.e.,

$$\Phi^d(t) \sim \text{HPPP}(\lambda), \forall t.$$

For simplicity we suppose the shape, location of sensor on the object, and the radial sensing support of the sensor, $M_i = (A_i, Y_i, S_i^0)$, do not change with time, e.g., objects do not rotate. Denote by

$$E_i^d(t) = X_i^d(t) \oplus A_i \tag{5.31}$$

the region occupied by object i at time t, and

$$S_i^d(t) = X_i^d(t) \oplus S_i^0 \tag{5.32}$$

the sensing support of sensor i at t. The environment and sensing sensing field at t is given by

$$\tilde{\Phi}^d(t) = \big\{\big(X_i^d(t), (A_i, Y_i, S_i^0)\big), i \in \mathbb{N}^+\big\},$$

and the model for the temporal dynamics of the environment and sensing capabilities is denoted by

$$\tilde{\mathbf{\Phi}}^{\boldsymbol{d}} = \big(\tilde{\Phi}^d(t), t \in \mathbb{R}\,\big).$$

We let Φ^s denote the locations of collaborating sensors at time 0.

The coverage set of sensor i at time t, $C_i^d(\tilde{\mathbf{\Phi}}^{\boldsymbol{d}}, t)$, is given by

$$C_i^d(\tilde{\mathbf{\Phi}}^{\boldsymbol{d}}, t) = \big\{x \in S_i^d(t) \big| x \in E_i^d(t) \text{ or } l_{X_i^d(t)+Y_i,x} \cap E^{-i,d}(t) \subseteq \{x\}\big\}, \quad (5.33)$$

where $E^{-i,d}(t) = \cup_{j \neq i} E_j^d(t)$ is the blockage set associated with objects other than i at t.

We let $D_i^d(t) \subseteq \mathbb{R}^2$ denote sensor i's region of interest at time t. We shall define the objects that a sensor needs to sense at time t as follows.

Definition 5.3.1. *(Objects of interest at time t) The objects of interest of sensor i at time t are the objects which overlap with sensor i's region of interest at t, denoted by $O_i^d(t)$, i.e.,*

$$O_i^d(t) = \big\{j \in \mathbb{N}^+ \big| E_j^d(t) \cap D_i^d(t) \neq \emptyset\big\}. \quad (5.34)$$

5.3.2 Sensing Redundancy and Coverage Resulting from Temporal Dynamics

We suppose an object i is sensed by object j at time t if sensor j senses any part of i, i.e.,

$$C_j^d(\tilde{\mathbf{\Phi}}^{\boldsymbol{d}}, t) \cap E_i^d(t) \neq \emptyset.$$

Sensors can track the states of objects in the environment, e.g., locations, velocity, acceleration, etc, and thus have a good estimate of the objects even when the objects are blocked for some time. For simplicity we assume an object is tracked by a sensor at t if the object has been sensed in time interval $[t-\tau, t]$, where τ is the maximum time window for reliable tracking without new sensor data.

The spatio-temporal sensing redundancy of an object can then be defined as follows.

Definition 5.3.2. *(Spatio-temporal object sensing redundancy) Given an environment and sensing model $\tilde{\mathbf{\Phi}}^{\boldsymbol{d}}$, a fixed subset of sensors collaborating, $K \subseteq \Phi^s$, and assuming an object can be sensed if it has been sensed within a time period τ, the* object sensing redundancy *of sensor i at time t is given by*

$$R^{\mathrm{o},d}(\tilde{\mathbf{\Phi}}^{\boldsymbol{d}}, K, i, t, \tau) = \sum_{j:X_j \in K} \mathbb{1}\left(\exists z \in [t-\tau, t] \ s.t. \ E_i^d(z) \cap C_j^d(\tilde{\mathbf{\Phi}}^{\boldsymbol{d}}, z) \neq \emptyset\right). \tag{5.35}$$

Given the above definition of spatio-temporal sensing redundancy we can define the (γ, τ)-object coverage reliability as follows.

Definition 5.3.3. *((γ, τ)-object coverage reliability) Given an environment and sensing field $\tilde{\mathbf{\Phi}}^{\boldsymbol{d}}$, a minimum redundancy requirement $\gamma \in \mathbb{N}^+$ for reliable sensing of an object, a subset of collaborating sensors, $K \subseteq \Phi^s$, and sensor i's objects interest O_i^d, the* γ-coverage object set *of sensor i is the set of objects of interest at time t which are covered by at least γ sensors in K, denoted by*

$$C_c^d(\tilde{\Phi}^d, K, O_i^d, \gamma, t, \tau) \triangleq \left\{ j \in O_i^d(t) \middle| R^d(\tilde{\Phi}^d, K, j, t, \tau) \geq \gamma \right\}. \tag{5.36}$$

The (γ, τ)-object coverage reliability *is proportion of the objects of interest that are in the* γ*-coverage set, i.e.,*

$$\frac{|C_c(\tilde{\Phi}, K, O_i^d, \gamma, t, \tau)|}{|O_i^d(t)|}. \tag{5.37}$$

5.3.3 Performance of Collaborative Sensing Utilizing Spatio-temporal Diversity

The relative movement of neighboring vehicles driving in the same direction would typically be small, e.g., the relative locations of vehicles in a fleet may be stable most time. Such slow relative movement facilitates the communication amongst the vehicles, but limits the temporal diversity in the sensing of vehicles moving in the same direction. The sensing coverage of collaborative sensing for vehicles moving in the same direction may fail to change quickly with time and obstructed vehicles will remain unseen. By comparison RSUs and vehicles moving in the opposite direction will see fast relative movements to a given flow of vehicles and have improved sensing coverage with temporal diversity. We have shown in Section 5.2 that RSUs can have an almost unobstructed view of the road if located well above the vehicles. In reality, RSUs may be low, e.g., lower RSUs to save cost, and vehicles are of different dimensions, thus the sensing of vehicles can be obstructed and RSUs may benefit from temporal sensing diversity. The relative velocity of vehicles moving in the opposite direction is large, i.e., $2 \cdot s$, thus there is more temporal diversity. However such high relative speed can make it difficult to establish reliable high rate links (in the mmWave band).

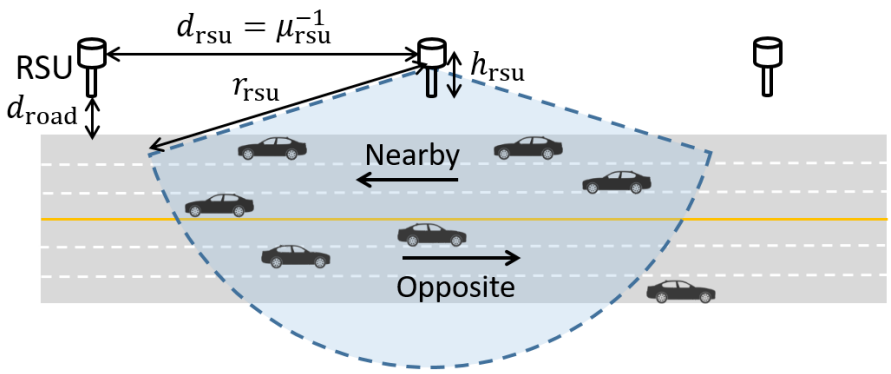

Figure 5.16: Freeway simulation scenario for RSU assisted collaborative sensing with temporal dynamics.

Let us evaluate the performance of collaborative sensing in the presence of such relative motions via simulation in a freeway scenario. We shall use the same assumptions on the deployment of RSUs as introduced in Section 5.2. We shall refer to the direction of the lanes close to RSUs as the 'nearby' direction, and the other direction as the 'opposite' direction, see Fig. 5.16.

We consider different collaborative sensing schemes, i.e., 1) base case: collaborate with only vehicles moving in the same direction. The communication channel is stable, yet the set of collaborating sensors is limited. 2) RSU: in addition vehicles communicate with sensing capable RSUs. 3) opposite: vehicles communicate with vehicles moving in the same direction and opposite direction.

Fig. 5.17 illustrates the $(1, \tau)$-object coverage reliability of collaborative sensing in different collaboration schemes and different τ. RSUs are uniformly deployed along the road, providing a 1-coverage of the road, e.g., $r_{\text{rsu}} = 200\,\text{m}$,

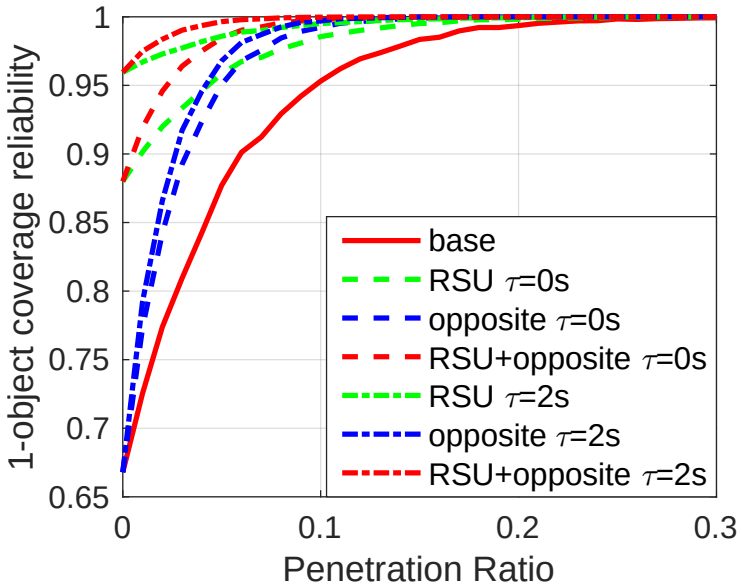

(a) Nearby direction

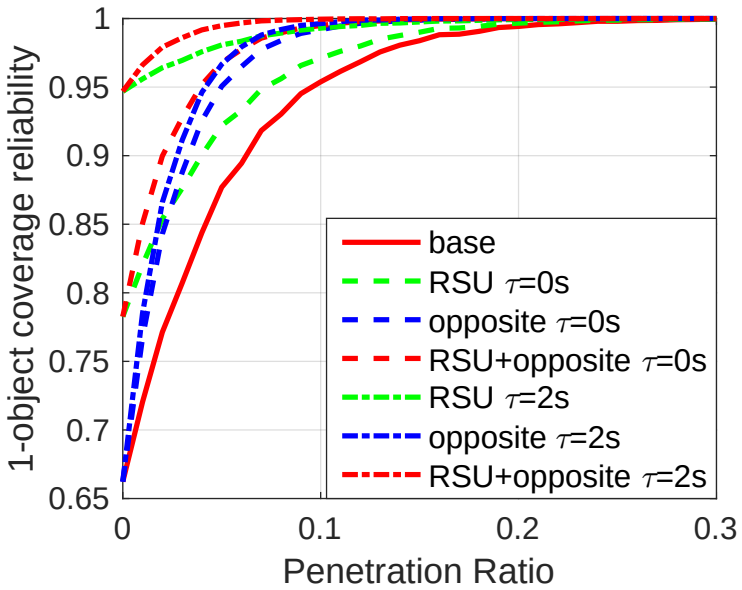

(b) Opposite direction

Figure 5.17: The $(1, \tau)$-object coverage reliability of collaborative sensing with vehicles driving in the same direction and RSUs for vehicles moving in (a) the original direction, and (b) the opposite direction.

$d_{\text{rsu}} = 400\,\text{m}$. We assume $r_{\text{interest}} = 200\,\text{m}$, $d_{\text{road}} = 2\,\text{m}$. The communication range is $r_{\text{comm}} = 500\,\text{m}$, which is enough for a vehicle to communicate with all sensors having relevant sensor data. We set $h_{\text{rsu}} = 1\,\text{m}$, which is lower than the heights of vehicles. Such assumption on h_{rsu} is mainly used to make the sensors subject to obstructions to study the impact of temporal diversity. The base case is that vehicles collaborate with other vehicles moving in the same direction.

First let us consider collaborative sensing without temporal diversity, i.e., $\tau = 0\,\text{sec}$. From simulation results we can see sensing coverage reliability increases with spatial diversity, i.e., collaboration with RSUs and/or vehicles in the opposite direction improves the sensing coverage reliability. More specifically, collaborating with RSUs provides larger gain at low penetrations while collaborating with vehicles in the opposite direction works better at high penetrations. As expected, collaborating with both RSUs and vehicles in the opposite direction provides most temporal diversity and thus most gain.

When temporal diversity in sensing is utilized, i.e., RSUs and vehicles in the opposite direction track objects using previous measurements, coverage reliability can be further improved. In fact the coverage reliability increases with τ. Note that collaborating with RSUs utilizing the temporal diversity alone can already provide a relative high coverage, e.g., over 95%. This indicates that relative mobile RSUs can have a good coverage of the environment by tracking objects even when RSUs are not located higher than all objects and are subject to objects. Comparison of coverage for vehicles moving in

different directions show that RSUs benefit more from temporal diversity in sensing vehicles moving in the further away lanes. The reason is that the obstructions in the nearby lanes have larger relative movements, thus RSUs will see larger temporal diversity in obstruction field.

5.3.4 Generalized Sensing with Mobile Sensors

In this section we provide a preliminary generalized model for sensing with mobile sensors. In particular we consider a setting where sensors are moving and sense the environment collaboratively. We try to characterize the coverage for a fixed object and the temporal dynamics of coverage for such an object.

We ignore the impact of obstructions, e.g., sensors are drones moving above the ground and not obstructed. Assume sensors are randomly located on an 2-D infinite plane, each moving in a random direction, $\Theta \sim \text{unif}[0, 2\pi]$. The velocity of sensor i at time t, $V_i(t) \in \mathbb{R}^+$, is IID, bounded and stationary. The acceleration of sensors is also bounded. We denote by $V \in \mathbb{R}^+$ a random variable having the same distribution of the sensor velocity. At time 0, the sensors are initially randomly located on the plane following an HPPP with intensity λ_{sensor},

$$\Phi^s = \{X_i, i \in \mathbb{N}^+\}.$$

The sensing support of sensor i, $S_i \in \mathbb{R}^2$, is a disc centered on the sensor with radius R_i, i.e., $S_i = b(X_i, R_i)$. Objects are randomly located on the plane, and we consider a typical object located at 0 with a fixed convex shape $a \subset \mathbb{R}^2$.

For a location, a is a single point. We assume that an object occupying is sensed if the region occupied by the object overlap with the sensing support of any sensor, i.e., the typical object is sensed if

$$\exists i \in \mathbb{N}^+ \text{ s.t. } S_i \cap a \neq \emptyset.$$

Based on our assumptions we have the following results on the distribution of sensors and the coverage of a typical object (or location).

Lemma 5.3.4. *(Displacement theorem) If at time* 0 *sensors follow an HPPP with intensity* λ_{sensor}*, sensors move independently in random directions uniformly distributed in* $[0, 2\pi]$ *and the velocities of sensors are IID, at any time* t *the locations of sensors follow an HPPP with intensity* λ_{sensor}*.*

Denote by $R \in \mathbb{R}^+$ a random variable with the same distribution as the radius of sensing support, $a \subseteq \mathbb{R}^2$ an convex shape representing the shape of the reference object. Recall that we let $\nu_2(a)$ denote the area of a, $\nu_1(\partial(a))$ the length of the perimeter of a. The number of sensors viewing the typical object with shape a is given by the following result.

Theorem 5.3.5. *(Number of sensors viewing an object) At any time* t*, the number of sensors seeing a typical object with a convex shape* a*,* $N_{\text{sensor}}(t)$*, follows a Poisson distribution with mean*

$$\mathrm{E}[N_{\text{sensor}}(t)] = \lambda_{\text{sensor}} \cdot \big(\pi\, \mathrm{E}[R^2] + \nu_2(a) + \mathrm{E}[R] \cdot \nu_1(\partial(a))\big). \tag{5.38}$$

The probability that the location is sensed by at least one sensor is then given by

$$p_{\text{sensed}} = 1 - e^{-\mathrm{E}[N_{\text{sensor}}(t)]}. \tag{5.39}$$

The above result is the direct application of generalized Steiner Formula [57] as used in Section 3.1.

Based on our previous analysis of temporal dynamics of blockage state in mobile wearable network, we characterize the spatio-temporal dynamics of the sensing of a typical object as follows.

Theorem 5.3.6. *(Temporal arrival of sensors covering a typical object) Based on our assumptions on sensor mobility, a given object of shape a experiences a Poisson arrival of new sensors which provide coverage that has rate*

$$\lambda^{Q}_{\text{sensor}} = \lambda_{\text{sensor}} \cdot \mathrm{E}[V] \cdot \big(2 \cdot \mathrm{E}[R] + \nu_1(\partial(a))/\pi\big), \tag{5.40}$$

where $\mathrm{E}[V]$ *is the average velocity of sensors.*

Theorem 5.3.7. *(Temporal dynamics of sensing of a typical object) The sensing state of a typical object follows an alternating renewal process. The duration an object of shape a is not viewed by any sensors,* $T_{\text{notsensed}}$*, has an exponential distribution with mean*

$$\begin{aligned} \mathrm{E}[T_{\text{notsensed}}] &= \frac{1}{\lambda^{Q}_{\text{sensor}}} \\ &= \frac{1}{\lambda_{\text{sensor}} \cdot \mathrm{E}[V] \cdot \big(2 \cdot \mathrm{E}[R] + \partial(a)/\pi\big)}. \end{aligned} \tag{5.41}$$

The duration the object is viewed by some sensor, T_{sensed}*, has mean*

$$\mathrm{E}[T_{\text{sensed}}] = \frac{p_{\text{sensed}}}{1 - p_{\text{sensed}}} \mathrm{E}[T_{\text{notsensed}}]. \tag{5.42}$$

The proof of the theorem follows our proof for Theorem 3.2.1. For the sensing of a location, we have $\nu_2(a) = 0$ and $\nu_1(\partial(a)) = 0$ and the results directly apply.

Based on Thm. 5.3.7 the probability (the proportion of time) that a location/object is not sensed for at least $t_{\text{notsensed}}$ is given by,

$$p_{\text{notsensed}} \cdot e^{-\lambda^{Q}_{\text{sensor}} \cdot t_{\text{notsensed}}}. \tag{5.43}$$

5.4 Robustness in Collaborative Sensing

In this part we briefly discuss the robustness characteristics of collaborative sensing.

5.4.1 Metric for Sensing Robustness

The (γ, τ)-object coverage reliability introduced in Def. 5.3.3 could be used as a metric for robustness in collaborative sensing. Diversity in the points of view (spatial diversity) helps improve the reliability of computational perception of the environment, e.g., a bicycle can be distinguished from pedestrians when seen from different points of view. The redundancy in sensor data also improves robustness to sensor / link failures. As for temporal diversity, measurements taken at different times can be used to better track and predict changes in the environment.

5.4.2 Impact of Failures

Sensing and communication are the two key components underlying collaborative sensing. The impact of different types of failures can be summarized as follows:

Failures in sensing and communication. If both the sensing and communication capability of a vehicle fail, the vehicle can no longer perceive the environment and perform automated driving. Such vehicles would need to be driven by humans or pull over to the side of the road. Such vehicles also would no longer participate in collaborative sensing. For other collaborative sensing vehicles, such failures are equivalent to reducing the penetration ratio. How the collaborative sensing performance and communication cost scales in the penetration ratio has already been studied in Section 4.2 and Section 4.4.

Failures in sensing. If the sensors on a vehicle fail but it can still communicate, the vehicle can sense the environment based on sensor data from other vehicles participating in collaborative sensing. The vehicle may still perform automated driving, but the sensing of the environment surrounding the vehicle can be poor, especially at low penetrations. In this setting collaborative sensing should probably facilitate human drivers instead of performing fully automated driving. To other vehicles, the penetration of sensors is lower, so is the sensing coverage and redundancy. However, the vehicle can still help relay data, thus the communication cost on V2I network does not increase (actually the communication cost may decrease as the total amount of generated sensor data reduces).

Failures in communication capabilities. If the communication capabilities of a vehicle fails, the vehicle can still sense the environment and perform automated driving based on its own sensors. However the coverage of a single vehicle is obstructed and the vehicle can not coordinate with other vehicles. The vehicle should take more conservative actions, including driving slower, increasing the gaps between vehicles, and being more cautious in path planning / changing lanes, etc. To other vehicles, failures in communication is the same as reducing penetration ratio.

5.5 Conclusion

In this chapter we show that carefully deployed sensing capable infrastructure has good coverage of roads, and can effectively help vehicles in sensing beyond obstructions. However, this would require deployment of sensing and communication capable RSUs regularly along the roads and at intersections, as enabling sensing at existing cellular infrastructure may suffer from obstructions. Furthermore, to share sensing data with all relevant vehicles, long range and high rate V2I/V2V (relay) links are required. One may consider enabling infrastructure to share and/or relay sensor data generated by vehicles and infrastructure with neighboring infrastructure via (mmWave) backhaul.

In addition our analysis and findings also apply for V2I communication relying on the availability of LOS channels, e.g., millimeter wave based communication. In the future more data traffic would be generated on the road, including safety related and infotainment data. Service providers may

focus more on serving the needs of increasing mobile traffic demands, e.g., by deploying infrastructure which are carefully placed (i.e. unobstructed coverage of roads) and have good backhaul support.

5.6 Appendix: Proofs and Additional Results

5.6.1 Proof of Theorem 5.1.1

Proof. Consider a typical point 0 on a typical horizontal line, x-axis. The intersections on a horizontal road follow an HPPP of intensity $\mu^{\mathrm{h}}_{\mathrm{inter}} = \lambda^{\mathrm{v}}_{\mathrm{road}}$, thus the spatial density of intersections is

$$\lambda_{\mathrm{inter}} = \lambda^{\mathrm{h}}_{\mathrm{road}} \cdot \lambda^{\mathrm{v}}_{\mathrm{road}}. \tag{5.44}$$

Case 1: $\lambda_{\mathrm{rsu}} \leq \lambda_{\mathrm{inter}}$. Each intersection has an independent probability of $\lambda_{\mathrm{rsu}}/\lambda_{\mathrm{inter}}$ to have a RSU. The RSUs along a typical road thus follows an HPPP with intensity

$$\frac{\lambda_{\mathrm{rsu}}}{\lambda_{\mathrm{inter}}} \cdot \mu^{\mathrm{h}}_{\mathrm{inter}} = \frac{\lambda_{\mathrm{rsu}}}{\lambda^{\mathrm{h}}_{\mathrm{road}}}. \tag{5.45}$$

The coverage probability is thus given by

$$p^{\mathrm{inter,h}}_{\mathrm{cover}}(\lambda_{\mathrm{rsu}}, r_{\mathrm{rsu}}, \lambda^{\mathrm{h}}_{\mathrm{road}}, \lambda^{\mathrm{v}}_{\mathrm{road}}) = 1 - e^{-\frac{\lambda_{\mathrm{rsu}}}{\lambda^{\mathrm{h}}_{\mathrm{road}}} \cdot 2 \cdot r_{\mathrm{rsu}}}. \tag{5.46}$$

Case 2: $\lambda_{\mathrm{rsu}} > \lambda_{\mathrm{inter}}$. Denote by $\mu^{\mathrm{rand}}_{\mathrm{rsu}}$ the linear intensity of the randomly distributed RSUs along the road in addition to the RSUs at intersections. The total spatial density of RSUs is λ_{rsu}, thus the spatial density of

randomly deployed RSUs should satisfy that

$$\lambda_{\text{rsu}} = \lambda_{\text{road}} \cdot \mu_{\text{rsu}}^{\text{rand}} + \lambda_{\text{inter}}, \tag{5.47}$$

$$\begin{aligned} \mu_{\text{rsu}}^{\text{rand}} &= \frac{\lambda_{\text{rsu}} - \lambda_{\text{inter}}}{\lambda_{\text{road}}} \\ &= \frac{\lambda_{\text{rsu}} - \lambda_{\text{road}}^{\text{h}} \cdot \lambda_{\text{road}}^{\text{v}}}{\lambda_{\text{road}}}. \end{aligned} \tag{5.48}$$

On a typical horizontal road, the RSUs at intersections and randomly deployed RSUs are independent, thus the RSUs on the road form an HPPP with intensity

$$\begin{aligned} \mu_{\text{rsu}}^{\text{total,h}} &= \mu_{\text{inter}}^{\text{h}} + \mu_{\text{rsu}}^{\text{rand}} \\ &= \lambda_{\text{road}}^{\text{v}} + \frac{\lambda_{\text{rsu}} - \lambda_{\text{road}}^{\text{h}} \cdot \lambda_{\text{road}}^{\text{v}}}{\lambda_{\text{road}}} \\ &= \frac{\lambda_{\text{rsu}} + (\lambda_{\text{road}}^{\text{v}})^2}{\lambda_{\text{road}}^{\text{h}} + \lambda_{\text{road}}^{\text{v}}}, \end{aligned} \tag{5.49}$$

i.e., the RSU intensity of randomly located RSUs plus the benefit from RSUs located at intersections. The coverage probability given $\lambda_{\text{rsu}} > \lambda_{\text{inter}}$ is thus given by

$$p_{\text{cover}}^{\text{inter,h}}(\lambda_{\text{rsu}}, r_{\text{rsu}}, \lambda_{\text{road}}^{\text{h}}, \lambda_{\text{road}}^{\text{v}}) = 1 - e^{-\mu_{\text{rsu}}^{\text{total,h}} \cdot 2 \cdot r_{\text{rsu}}}. \tag{5.50}$$

Combine the two cases and we finish the proof. □

5.6.2 Proof of Theorem 5.1.2

Proof. Under our model of buildings, the region occupied by buildings follow a Boolean process [57]. A building centered at y with shape a^0 blocks the BS at x if

$$(y \oplus E(x, a^0)) \cap l_{0,\rho(a^0)\cdot x} \neq \emptyset, \tag{5.51}$$

i.e., the location of building satisfies that,

$$y \in \big(l_{0,\rho(a^0)\cdot x} \oplus \check{E}(x, a^0)\big). \tag{5.52}$$

The buildings are independent, and $y \in D_{\mathrm{b}}$, thus we can get the expected number of obstructing buildings by taking expectation over A^0, i.e.,

$$\mathrm{E}[N_{\mathrm{b}}(x)] = \lambda_{\mathrm{b}} \cdot \mathrm{E}_{A^0}\big[\big|(l_{0,\rho\cdot x} \oplus \check{E}(x, A^0)) \cap D_{\mathrm{b}}\big|\big] \tag{5.53}$$

By the Boolean process, $N_{\mathrm{b}}(x)$ follows an exponential distribution, thus the probability that a BS located at x is not obstructed is given by

$$\mathrm{P}(N_{\mathrm{b}}(x) = 0) = e^{-\mathrm{E}[N_{\mathrm{b}}(x)]}. \tag{5.54}$$

By Campbell's theorem [57], the number of BSs sensing 0, N_{BS}, has mean

$$\mathrm{E}[N_{\mathrm{BS}}] = \lambda_{\mathrm{BS}} \cdot \int_{D_{\mathrm{BS}} \cap b(x, r_{\mathrm{BS}})} e^{-\mathrm{E}[N_{\mathrm{b}}(x)]} dx. \tag{5.55}$$

□

5.6.3 RSU Sensing Coverage in Poisson Line Process Model

We consider the coverage of infrastructure based sensing in Poisson line process road model.

Each road is modeled as a undirected straight line in the space, parametrized by (p, θ), where $p \in \mathbb{R}$ is the perpendicular distance to the origin 0, $\theta \in [0, \pi)$ is the angle between the line and the x_1 axis, see [57].

$$\Phi_L = \{(P_i, \Theta_i), i \in \mathbb{N}^+\}.$$

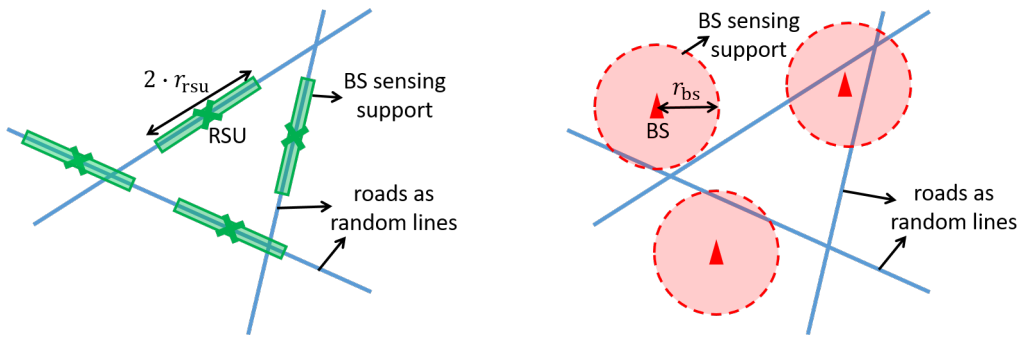

(a) RSU based sensing (b) Cellular based sensing

Figure 5.18: (a) Model for RSU based sensing. (b) Model for cellular (BS) based sensing.

with intensity λ_{road}. The state space of lines is $\mathbb{R} \times [0, \pi]$, and the state of the lines, (P_i, Θ_i), follow an HPPP with intensity λ_{road} in $\mathbb{R} \times [0, \pi)$. This process is known to be translation invariant and to have an average length of line segments per unit area λ_{road} [57].

In randomly distributed and evenly spaced deployment schemes, the coverages are the same as the results in the MPLP model, see Eq. 5.9 and Eq. 5.10. For RSUs at intersections along with randomly distributed RSUs, let us first study the distribution of road intersections. Denote by λ_{inter} the spatial density of road intersections, which is given in the following theorem.

Theorem 5.6.1. *In a Poisson line model of density λ_{road}, the intersections on a line follows an HPPP of intensity*

$$\mu_{\text{inter}} = \frac{2}{\pi} \cdot \lambda_{\text{road}}. \tag{5.56}$$

The spatial density of line intersections is

$$\lambda_{\text{inter}} = \frac{\lambda_{\text{road}}^2}{\pi}. \tag{5.57}$$

Proof. Consider a typical line selected from the line process, $e \in \Phi_L$. By Slivnyak-Mecke theorem [57], the Palm distribution of the line process as seen by e, $\Phi_L \backslash \{e\}$, has the same distribution of Φ_L. Denote by Ψ the intersections between e and $\Phi_L \backslash \{e\}$. Φ_L is isotropic, i.e., $\Theta_i \sim \text{unif}[0, 2\pi]$, and translation invariant, thus Ψ is a Poisson point process on e [57] with intensity

$$\mu_{\text{inter}} = \frac{2}{\pi} \cdot \lambda_{\text{road}}. \tag{5.58}$$

Each RSU deployed at intersections is shared by two roads, thus λ_{inter} is given by

$$\begin{aligned} \lambda_{\text{inter}} &= \frac{\lambda_{\text{road}} \cdot \mu_{\text{inter}}}{2} \\ &= \frac{\lambda_{\text{road}}^2}{\pi}. \end{aligned} \tag{5.59}$$

□

Compared to the intersection density in MPLP in Eq. 5.11, the intersection density in the Poisson line model is larger at the same road density λ_{road}. The coverage of the roads is given by the following theorem.

Theorem 5.6.2. *In the Poisson line road system, the coverage probability of RSUs when RSUs are first deployed at intersections and then along the roads randomly is given by,*

$$p_{\text{cover}}^{\text{rsu,inter}}(\lambda_{\text{rsu}}, r_{\text{rsu}}, \lambda_{\text{road}}) = \begin{cases} 1 - e^{-\frac{2 \cdot \lambda_{\text{rsu}}}{\lambda_{\text{road}}} \cdot (2 \cdot r_{\text{rsu}})}, & \text{if } \pi \cdot \lambda_{\text{rsu}} \leq \lambda_{\text{road}}^2 \\ 1 - e^{-\mu_{\text{rsu}}^{\text{total}} \cdot (2 \cdot r_{\text{rsu}})}, & \text{otherwise} \end{cases}, \tag{5.60}$$

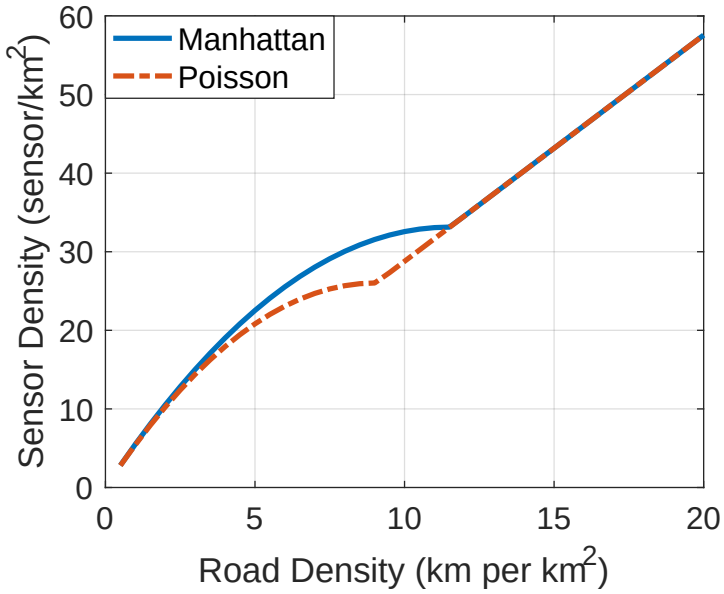

Figure 5.19: Required sensor density to achieve 90% coverage at different road densities under MPLP model and Poisson line process model.

where

$$\mu_{\text{rsu}}^{\text{total}} = \frac{1}{\pi} \cdot \lambda_{\text{road}} + \frac{\lambda_{\text{rsu}}}{\lambda_{\text{road}}} \tag{5.61}$$

is the linear density of RSUs on a typical road when $\lambda_{\text{inter}} > \lambda_{\text{rsu}}$.

The proof of the above result is similar to the proof of Theorem 5.1.1 in the appendix (Section 5.6.1). The scaling of coverage in λ_{rsu}, r_{rsu}, and λ_{road}, is similar to those in MPLP model, and the conclusions and implications on the performance and deployment of RSUs would be identical. The only difference would be that the density of road intersections is higher than that in MPLP. The required RSU density to reach coverage requirement, $\lambda_{\text{rsu}}^{\text{inter,min}}$, could be smaller as there are more intersections to deploy RSUs, see Fig. 5.19.

Chapter 6

Conclusion and Future Work

Recent advances in communication and sensing technologies are enabling new applications, e.g., mmWave based wearable devices and collaborative sensing for automated driving. These new application scenarios bring new challenges to communication network design. Communication in mmWave bands is promising in that it can in principle provide high rates and low latency, yet is sensitive to blockages and mobility, especially for wearable networks in dense and dynamic environments. In automated driving applications, sensing and information sharing (in mmWave bands) are also subject to obstruction and dynamics in the environment. In this dissertation we explored the impact of blockage (obstruction) and mobility on collaborative sensing and mmWave based communication, and the implications on the design of communication networks.

mmWave based communication. At a high level the results in this dissertation suggest that for dense mmWave wearable networks, blockage from neighboring users' bodies limits the strong interferers to a few stable nearby neighbors, which should make it possible to design scalable MAC protocols to manage interference. However, communication amongst wearable devices on a

single user could still be challenging. Such communication channels are subject to blockage by the user, e.g., limbs and torso, and to maintain connectivity may need to rely on reflections off (mobile) nearby objects. Addressing the need for reliable (low latency) connectivity when such self blockages occur, might be a challenge for such systems.

Collaborative sensing. In this dissertation we quantified the performance benefits and communication costs associated with collaborative sensing, and their dependence on the penetration of collaborative vehicles. Our study focused on characterizing what can be "seen" via collaborative sensing, e.g., sensing coverage and redundancy/diversity. Quantifying how such information will improve computational perception of the environment, e.g., translating sensing coverage and redundancy perception quality or application performance remains yet to be addressed. This is critical towards deciding collaboration schemes and thus communication requirements of future vehicular automated driving systems. We envision that collaborative sensing based on generic sensing models, i.e., vehicles using standardized models of the environment and sharing processed sensor data based on such models, will save computation and communication costs and is likely to be critical in the development of such systems.

Bibliography

[1] A. Pyattaev, K. Johnsson, S. Andreev, and Y. Koucheryavy, "Communication challenges in high-density deployments of wearable wireless devices," *IEEE Wireless Communications*, vol. 22, no. 1, pp. 12–18, 2015.

[2] "IEEE standard for information technology telecommunications and information exchange between systems local and metropolitan area networks specific requirements. part 11: Wireless LAN medium access control (MAC) and physical layer (PHY) specifications amendment 3: Enhancements for very high throughput in 60 GHz band," *IEEE Standard 802.11ad*, 2012.

[3] "IEEE standard for information technology telecommunications and information exchange between systems local and metropolitan area networks specific requirements. part 15.3: Wireless medium access control (MAC) and physical layer (PHY) specifications for high rate wireless personal area networks (WPANs) amendment 2: Millimeter-wave-based alternative physical layer extension," *IEEE Standard 802.15.3c*, 2009.

[4] ECMA International, "High rate 60 GHz PHY, MAC and PALs," *ECMA Standard 387*, 2010.

[5] T. S. Rappaport, G. R. MacCartney, M. K. Samimi, and S. Sun, "Wide-

band millimeter-wave propagation measurements and channel models for future wireless communication system design," *IEEE Trans. Commun.*, vol. 63, no. 9, pp. 3029–3056, 2015.

[6] S. Sun, G. R. MacCartney, and T. S. Rappaport, "Millimeter-wave distance-dependent large-scale propagation measurements and path loss models for outdoor and indoor 5G systems," in *Antennas and Propagation (EuCAP), 2016 10th European Conference on.* IEEE, 2016, pp. 1–5.

[7] S. Sun, T. S. Rappaport, T. A. Thomas, A. Ghosh, H. C. Nguyen, I. Z. Kovács, I. Rodriguez, O. Koymen, and A. Partyka, "Investigation of prediction accuracy, sensitivity, and parameter stability of large-scale propagation path loss models for 5G wireless communications," *IEEE Trans. Veh. Technol.*, vol. 65, no. 5, pp. 2843–2860, 2016.

[8] S. Nie, M. K. Samimi, T. Wu, S. Deng, G. R. MacCartney Jr, and T. S. Rappaport, "73 GHz millimeter-wave indoor and foliage propagation channel measurements and results," *NYU WIRELESS Technical Report, TR-2014–003*, 2014.

[9] G. R. Maccartney, T. S. Rappaport, S. Sun, and S. Deng, "Indoor office wideband millimeter-wave propagation measurements and channel models at 28 and 73 GHz for ultra-dense 5G wireless networks," *IEEE Access*, vol. 3, pp. 2388–2424, 2015.

[10] S. Geng, J. Kivinen, X. Zhao, and P. Vainikainen, "Millimeter-wave

propagation channel characterization for short-range wireless communications," *IEEE Trans. Veh. Technol.*, vol. 58, no. 1, pp. 3–13, 2009.

[11] S. Sun, T. S. Rappaport, T. A. Thomas, and A. Ghosh, "A preliminary 3D mm wave indoor office channel model," in *Computing, Networking and Communications (ICNC), 2015 International Conference on.* IEEE, 2015, pp. 26–31.

[12] M. K. Samimi and T. S. Rappaport, "3-D millimeter-wave statistical channel model for 5G wireless system design," *IEEE Trans. Microw. Theory Tech.*, vol. 64, no. 7, pp. 2207–2225, 2016.

[13] C. Gustafson and F. Tufvesson, "Characterization of 60 GHz shadowing by human bodies and simple phantoms," in *Antennas and Propagation (EUCAP), 2012 6th European Conference on.* IEEE, 2012, pp. 473–477.

[14] S. Collonge, G. Zaharia, and G. E. Zein, "Influence of the human activity on wide-band characteristics of the 60 GHz indoor radio channel," *IEEE Trans. Wireless Commun.*, vol. 3, no. 6, pp. 2396–2406, 2004.

[15] S. Singh, F. Ziliotto, U. Madhow, E. Belding, and M. Rodwell, "Blockage and directivity in 60 GHz wireless personal area networks: From cross-layer model to multihop MAC design," *IEEE J. Sel. Areas Commun.*, vol. 27, no. 8, 2009.

[16] I. Kashiwagi, T. Taga, and T. Imai, "Time-varying path-shadowing model for indoor populated environments," *IEEE Trans. Veh. Technol.*, vol. 59,

no. 1, pp. 16–28, 2010.

[17] T. Bai and R. W. Heath, "Coverage and rate analysis for millimeter-wave cellular networks," *IEEE Trans. Wireless Commun.*, vol. 14, no. 2, pp. 1100–1114, 2015.

[18] A. Thornburg, T. Bai, and R. W. Heath, "Performance analysis of outdoor mmWave ad hoc networks," *IEEE Trans. Signal Process.*, vol. 64, no. 15, pp. 4065–4079, 2016.

[19] K. Venugopal, M. C. Valenti, and R. W. Heath, "Device-to-device millimeter wave communications: Interference, coverage, rate, and finite topologies," *IEEE Trans. Wireless Commun.*, vol. 15, no. 9, pp. 6175–6188, 2016.

[20] G. George and A. Lozano, "Performance of enclosed mmWave wearable networks," in *IEEE Int'l Workshop on Compuational Advances in Multi-Sensor Adaptive Processing (CAMSAP 15)*, 2015.

[21] O. Galinina, A. Turlikov, A. Pyattaev, K. Johnsson, S. Andreev, and Y. Koucheryavy, "A capacity bound for mmWave-based channel access in ultra-dense wearable deployments," in *Ultra Modern Telecommunications and Control Systems and Workshops (ICUMT), 2015 7th International Congress on.* IEEE, 2015, pp. 298–304.

[22] O. Galinina, A. Pyattaev, K. Johnsson, A. Turlikov, S. Andreev, and Y. Koucheryavy, "Assessing system-level energy efficiency of mmWave-

based wearable networks," *IEEE J. Sel. Areas Commun.*, vol. 34, no. 4, pp. 923–937, 2016.

[23] E. Shihab, L. Cai, and J. Pan, "A distributed asynchronous directional-to-directional MAC protocol for wireless ad hoc networks," *IEEE Trans. Veh. Technol.*, vol. 58, no. 9, pp. 5124–5134, 2009.

[24] S. Singh, R. Mudumbai, and U. Madhow, "Distributed coordination with deaf neighbors: efficient medium access for 60 GHz mesh networks," in *INFOCOM, 2010 Proceedings IEEE*. IEEE, 2010, pp. 1–9.

[25] W. Feng, Y. Li, D. Jin, and L. Zeng, "Inter-network spatial sharing with interference mitigation based on IEEE 802.11 ad WLAN system," in *Globecom Workshops (GC Wkshps), 2014*. IEEE, 2014, pp. 752–758.

[26] Z. He, S. Mao, and T. T. S. Rappaport, "On link scheduling under blockage and interference in 60-GHz ad hoc networks," *IEEE Access*, vol. 3, pp. 1437–1449, 2015.

[27] X. An, C.-S. Sum, R. V. Prasad, J. Wang, Z. Lan, J. Wang, R. Hekmat, H. Harada, and I. Niemegeers, "Beam switching support to resolve link-blockage problem in 60 GHz WPANs," in *Personal, Indoor and Mobile Radio Communications, 2009 IEEE 20th International Symposium on*. IEEE, 2009, pp. 390–394.

[28] S. Sur, X. Zhang, P. Ramanathan, and R. Chandra, "Beamspy: enabling robust 60 GHz links under blockage," in *13th USENIX Symposium on*

Networked Systems Design and Implementation (NSDI 16). USENIX Association, 2016, pp. 193–206.

[29] A. Rauch, F. Klanner, and K. Dietmayer, "Analysis of V2X communication parameters for the development of a fusion architecture for cooperative perception systems," in *Intelligent Vehicles Symposium (IV), 2011 IEEE.* IEEE, 2011, pp. 685–690.

[30] H. Li and F. Nashashibi, "Multi-vehicle cooperative perception and augmented reality for driver assistance: A possibility to seethrough front vehicle," in *Intelligent Transportation Systems (ITSC), 2011 14th International IEEE Conference on.* IEEE, 2011, pp. 242–247.

[31] A. Rauch, F. Klanner, R. Rasshofer, and K. Dietmayer, "Car2x-based perception in a high-level fusion architecture for cooperative perception systems," in *Intelligent Vehicles Symposium (IV), 2012 IEEE.* IEEE, 2012, pp. 270–275.

[32] S.-W. Kim, Z. J. Chong, B. Qin, X. Shen, Z. Cheng, W. Liu, and M. H. Ang, "Cooperative perception for autonomous vehicle control on the road: Motivation and experimental results," in *Intelligent Robots and Systems (IROS), 2013 IEEE/RSJ International Conference on.* IEEE, 2013, pp. 5059–5066.

[33] X. Zhao, K. Mu, F. Hui, and C. Prehofer, "A cooperative vehicle-infrastructure based urban driving environment perception method using a D-S theory-

based credibility map," *Optik-International Journal for Light and Electron Optics*, vol. 138, pp. 407–415, 2017.

[34] J. B. Kenney, "Dedicated short-range communications (DSRC) standards in the united states," *Proc. IEEE*, vol. 99, no. 7, pp. 1162–1182, 2011.

[35] M. Torrent-Moreno, J. Mittag, P. Santi, and H. Hartenstein, "Vehicle-to-vehicle communication: fair transmit power control for safety-critical information," *IEEE Trans. Veh. Technol.*, vol. 58, no. 7, pp. 3684–3703, 2009.

[36] H. Seo, K.-D. Lee, S. Yasukawa, Y. Peng, and P. Sartori, "LTE evolution for vehicle-to-everything services," *IEEE Commun. Mag.*, vol. 54, no. 6, pp. 22–28, 2016.

[37] "3GPP TS 22.186 v15.1.0 study on enhancement of 3GPP support for V2X scenarios; stage 1 (release15)," June 2016.

[38] "3GPP TR 22.886 v15.1.0 study on enhancement of 3GPP support for 5G V2X services (release15)," March 2017.

[39] V. Va, T. Shimizu, G. Bansal, R. W. Heath Jr *et al.*, "Millimeter wave vehicular communications: A survey," *Foundations and Trends® in Networking*, vol. 10, no. 1, pp. 1–113, 2016.

[40] J. Choi, V. Va, N. Gonzalez-Prelcic, R. Daniels, C. R. Bhat, and R. W. Heath, "Millimeter-wave vehicular communication to support massive au-

tomotive sensing," *IEEE Commun. Mag.*, vol. 54, no. 12, pp. 160–167, 2016.

[41] C. Lundquist, T. B. Schön, and U. Orguner, "Estimation of the free space in front of a moving vehicle," 2009.

[42] S. Thrun *et al.*, "Robotic mapping: A survey," *Exploring artificial intelligence in the new millennium*, vol. 1, pp. 1–35, 2002.

[43] A. Petrovskaya and S. Thrun, "Model based vehicle detection and tracking for autonomous urban driving," *Autonomous Robots*, vol. 26, no. 2-3, pp. 123–139, 2009.

[44] G. Zhang, Y. Xu, X. Wang, X. Tian, J. Liu, X. Gan, H. Yu, and L. Qian, "Multicast capacity for VANETs with directional antenna and delay constraint," *IEEE J. Sel. Areas Commun.*, vol. 30, no. 4, pp. 818–833, 2012.

[45] S. Kwon, Y. Kim, and N. B. Shroff, "Analysis of connectivity and capacity in 1-D vehicle-to-vehicle networks," *IEEE Trans. Wireless Commun.*, vol. 15, no. 12, pp. 8182–8194, 2016.

[46] X. He, H. Zhang, W. Shi, T. Luo, and N. C. Beaulieu, "Transmission capacity analysis for linear VANET under physical model," *China Communications*, vol. 14, no. 3, pp. 97–107, 2017.

[47] A. T. Giang, A. Busson, A. Lambert, and D. Gruyer, "Spatial capacity of IEEE 802.11 p-based VANET: Models, simulations, and experimen-

tations," *IEEE Trans. Veh. Technol.*, vol. 65, no. 8, pp. 6454–6467, 2016.

[48] G. Ozbilgin, U. Ozguner, O. Altintas, H. Kremo, and J. Maroli, "Evaluating the requirements of communicating vehicles in collaborative automated driving," in *Intelligent Vehicles Symposium (IV), 2016 IEEE*. IEEE, 2016, pp. 1066–1071.

[49] J. O'rourke, *Art gallery theorems and algorithms*. Oxford University Press Oxford, 1987, vol. 57.

[50] L. Hobert, A. Festag, I. Llatser, L. Altomare, F. Visintainer, and A. Kovacs, "Enhancements of V2X communication in support of cooperative autonomous driving," *IEEE Commun. Mag.*, vol. 53, no. 12, pp. 64–70, 2015.

[51] M. Wang, W. Daamen, S. P. Hoogendoorn, and B. Van Arem, "Connected variable speed limits control and car-following control with vehicle-infrastructure communication to resolve stop-and-go waves," *Journal of Intelligent Transportation Systems*, vol. 20, no. 6, pp. 559–572, 2016.

[52] K. Sato, T. Manabe, T. Ihara, H. Saito, S. Ito, T. Tanaka, K. Sugai, N. Ohmi, Y. Murakami, M. Shibayama *et al.*, "Measurements of reflection and transmission characteristics of interior structures of office building in the 60-GHz band," *IEEE Trans. Antennas Propag.*, vol. 45, no. 12, pp. 1783–1792, 1997.

[53] F. Baccelli and B. Błaszczyszyn, "Stochastic geometry and wireless networks: Volume I Theory," *Foundations and Trends® in Networking*, vol. 3, no. 3–4, pp. 249–449, 2009.

[54] J. F. C. Kingman, *Poisson processes*. Wiley Online Library, 1993.

[55] B. Matérn, *Spatial variation*. Springer Science & Business Media, 2013, vol. 36.

[56] B. J. Frey and D. Dueck, "Clustering by passing messages between data points," *Science*, vol. 315, no. 5814, pp. 972–976, 2007.

[57] S. N. Chiu, D. Stoyan, W. S. Kendall, and J. Mecke, *Stochastic geometry and its applications*. John Wiley & Sons, 2013.

[58] P. Madadi, F. Baccelli, and G. de Veciana, "On temporal variations in mobile user SNR with applications to perceived QoS," in *Modeling and Optimization in Mobile, Ad Hoc, and Wireless Networks (WiOpt), 2016 14th International Symposium on*. IEEE, 2016, pp. 1–8.

[59] P. Hall, "Heavy traffic approximations for busy period in an M/G/ queue," *Stochastic Processes and their Applications*, vol. 19, no. 2, pp. 259–269, 1985.

[60] H. G. Seif and X. Hu, "Autonomous driving in the iCity–HD maps as a key challenge of the automotive industry," *Engineering*, vol. 2, no. 2, pp. 159–162, 2016.

[61] "Automated driving levels of driving automation are defined in new SAE international standard J3016," October 2014.

[62] "3GPP TR 36.885 v14.0.0 study on LTE-based V2X services (release 14)," June 2016.

[63] S. Thrun, W. Burgard, and D. Fox, *Probabilistic robotics*. MIT press, 2005.

[64] P. Gupta and P. R. Kumar, "The capacity of wireless networks," *IEEE Trans. Inf. Theory*, vol. 46, no. 2, pp. 388–404, 2000.

[65] F. Baccelli, M. Klein, M. Lebourges, and S. Zuyev, "Stochastic geometry and architecture of communication networks," *Telecommunication Systems*, vol. 7, no. 1, pp. 209–227, 1997.

[66] F. Baccelli and X. Zhang, "A correlated shadowing model for urban wireless networks," in *Computer Communications (INFOCOM), 2015 IEEE Conference on*. IEEE, 2015, pp. 801–809.

[67] Y. Wang, K. Venugopal, A. F. Molisch, and R. W. Heath, "Analysis of urban millimeter wave microcellular networks," in *Vehicular Technology Conference (VTC-Fall), 2016 IEEE 84th*. IEEE, 2016, pp. 1–5.

[68] W. Chang, H. Zheng, J. Wu, C. C Tan, and H. Ling, "Environmental-assisted vehicular data in smart cities," *Smart Cities: Foundations, Principles, and Applications*, pp. 819–844, 2017.

[69] A. Jalooli, M. Song, and X. Xu, "Delay efficient disconnected RSU placement algorithm for VANET safety applications," in *Wireless Communications and Networking Conference (WCNC), 2017 IEEE*. IEEE, 2017, pp. 1–6.

[70] Y. Jo and J. Jeong, "RPA: Road-side units placement algorithm for multihop data delivery in vehicular networks," in *Advanced Information Networking and Applications Workshops (WAINA), 2016 30th International Conference on*. IEEE, 2016, pp. 262–266.

[71] J. G. Andrews, F. Baccelli, and R. K. Ganti, "A tractable approach to coverage and rate in cellular networks," *IEEE Transactions on Communications*, vol. 59, no. 11, pp. 3122–3134, 2011.

[72] T. J. Hawbaker, V. C. Radeloff, R. B. Hammer, and M. K. Clayton, "Road density and landscape pattern in relation to housing density, and ownership, land cover, and soils," *Landscape Ecology*, vol. 20, no. 5, pp. 609–625, 2005.

[73] D. J. Aldous and W. S. Kendall, "Short-length routes in low-cost networks via Poisson line patterns," *Advances in Applied Probability*, vol. 40, no. 1, pp. 1–21, 2008.

Vita

Yicong Wang received his B.S. in information science and technology from Tsinghua University in 2012, and M.S.E. in electrical and computer engineering from the University of Texas at Austin in 2014. Since 2012, he has been working under the supervision of Prof. Gustavo de Veciana in the Wireless Networking and Communications Group (WNCG) in the Department of Electrical and Computer Engineering at the University of Texas at Austin. He interned at Intel Labs, Santa Clara, in summer 2016.

Permanent address: 1 University Station C0803
Austin, Texas 78712-0240

This dissertation was typeset with LaTeX[†] by the author.

[†]LaTeX is a document preparation system developed by Leslie Lamport as a special version of Donald Knuth's TeX Program.